博士論文

Markerless Tracking of Brain Surface by Non-rigid Registration Combining Shape and Texture Information

(形状とテクスチャの情報を用いた非剛体レジストレーションによる脳表のマーカーレストラッキング)

蒋 崛

Content

List of Tables

List of Figures

1 Introduction

1.1 Brain Surgery

In these decades, brain tumor has drawn much attention for it is estimated that 35% of all the tumors are attributable to brain tumor [1]. Patients who have brain tumor, usually suffer from more frequent and severe headache, unexplained nausea or vomiting, vision or speech problem, seizures and so on. These symptoms have greatly obstructed the patients' life with inconveniences. Furthermore, according to the latest investigations, brain tumor disease has keep increasing in recent years[2]. Thus, conquering the brain cancer becoming more and more important. Since brain tumor is usually located inside the head of patient, brain surgery is one of the approaches to cure the tumor.

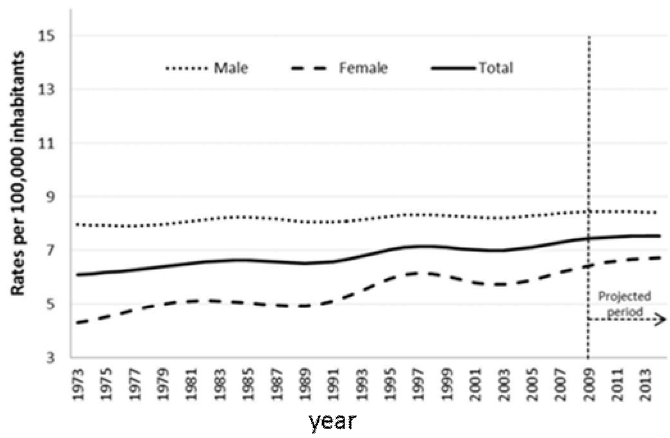

Figure 1-1 Brain cancer incidence trend[2]

During brain surgery, there are some critical eloquent areas, on brain surface, which can control human ability such as speech, language, vision, sensation, and movement function, as shown in Figure 1-2. In this circumstance, the price to pay for resection of brain tumor may be an increase in morbidity or sequela, especially in case of brain tumors in eloquent areas due to the high eloquence of the surrounding brain tissue. For example, it is reported that the majority of patients will suffer a relapse or local progression of the disease some time after surgery. Therefore, these areas are significant important and need to be protected during surgery and knowing the accurate brain tumor information, as well as brain function area, vessels is needed. Fortunately, nowadays we can get the 3D brain volumetric information using imaging technology, such as MRI, CT and Ultra sound, which can offer the accurate information of them. However, the problem is how to map these structures onto patient brain surface, which is difficult since brain will deform with a 30-mm magnitude on average during surgery. Such amount of deformation which would trivialize the current brain navigation system and cannot be ignored. To overcome these problems, some methods have been proposed, which will be described in the following sections.

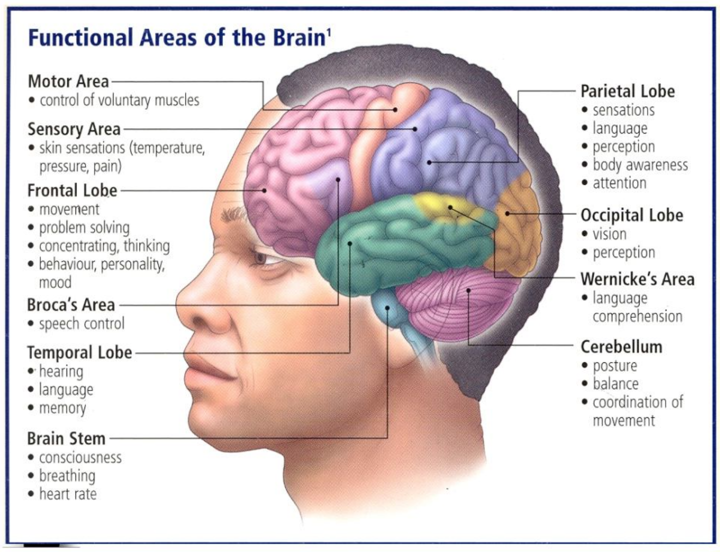

Figure 1-2 The brain eloquent areas. Left temporal and frontal lobes is speech and language area; bilateral occipital lobes is vision area; bilateral parietal lobes is sensation area; bilateral motor cortex is movement area[3]

1.2 Electrical Stimulation to identify the functions of brain surface

The first technology to map the brain function area before and during surgery is the electrical stimulation. This technology usually allows the surgeons to localize the brain surface function areas with awake (language areas) or non-relaxed (motor areas) patients by directly stimulating the brain surface. Moreover, this technology allows the realization of the function map to identify whether the exposed cerebral cortex is significant or not. The electrical stimulation procedure works as follow: the neurosurgeons place an electrode at a small region of cortical area of the brain; then a stimulator from the computer applies some stimuli, which can result in neurological change as patient numbness or movement or inhibit neurological function as speech arrest. When the stimulation of a local region generates any of the above symptoms not accompanied by a crisis or post-discharge, it is realized and confirmed that the stimulated brain area is an important region for brain function. The stimulation procedure is finished by marking the brain surface with sterile labels to avoid damaging the eloquent areas. Figure 1-3 shows the electrical stimulation on brain surgery for the brain function mapping of language function area. The two language function areas are identified and labeled by paper markers in brain surgery. However, this kind of electrical stimulation method is an invasive method and the electrical current might cause epilepsy by accident during surgery. To avoid this invasive approach, image-guided neurosurgery (IGNS) systems have been developed over the years to assist surgeons during brain surgery while avoiding invasively stimulating the eloquent areas. The details about IGNS will be described in the next section.

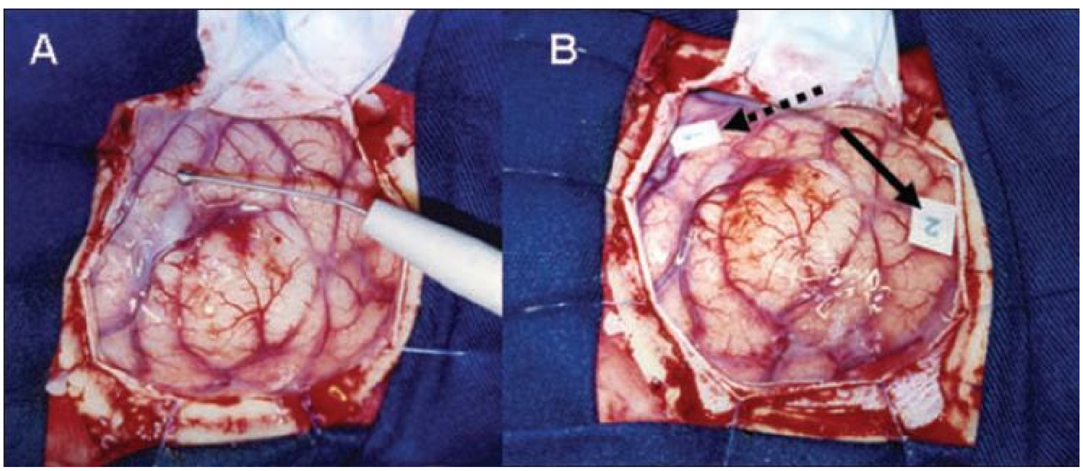

Figure 1-3 Electrical stimulation to identify the brain functions[4]

1.3 Image-Guided Neurosurgery (IGNS)

Over the past century, Image-Guided Neurosurgery (IGNS) systems have developed a standard operating room protocol for invasively assisting the surgeons. Image-Guided Neurosurgery (IGNS) systems are usually adapted to locate the surgery target (tumor and eloquent area) and assist the surgeon to know the exact position of the patient brain, surgical tools as well as brain surface during surgery. Commonly, in IGNS system, the preoperative image (e.g. preoperative MR) is acquired prior to the surgery procedure to assist the navigation of the surgery. To establish the guidance, the preoperative image is rigidly rotated and translated to align with the patient in the operative room (OR). The transformation between the preoperative image and the OR system is usually based on the locations of several features both in the preoperative image and the OR coordinate system. The features commonly used in the surgery are scalp-attached fiducials, as shown in Figure 1-4 (a). Those fiducials will appear hyper-intense on preoperative imaging so that they would be readily visible on the preoperative imaging. IGNS usually assist surgeons in two aspects. Firstly, they make the planning of surgery easier and match the correspondence between the preoperative multimodality 3D images and the patient systems. Accordingly, the surgeons could define and relate the boundaries of the anatomical and eloquent structures as well as to define the surgical targets and trajectories. Secondly, the IGNS systems can relate the preoperative images, the patient's head and the positions of the surgeons' instruments with each other in the operative room. Thus, the probe (or another instrument) and the set of the preoperative image are related and then the surgeon could navigate with the probe simultaneously in the patients' head (patient space coordinate system) and preoperative image (preoperative image coordinate system). Therefore, the IGNS can track both the surgical instruments and the patient's brain surface.

Based on the research of the IGNS systems, the overall IGNS accuracy is estimated to be 2 mm[5] when assuming that the preoperative image keeps the same shape of the patient brain during surgery. However, this assumption could not be held during surgery since the skull opening, brain retraction, cerebrospinal fluid (CSF) suction or outflow, lesion resection, perfusion and pharmacological manipulation during surgery indeed alter the 3D morphology of brain structures, and could lead to localization and tracking errors which might be one order of magnitude larger than common IGNS accuracy. This kind of phenomena of brain structure change during surgery is called brain shift. The traditional IGNS does not compensate brain shift and brain shift is then becoming one of the major problems of IGNS. The detail of the magnitude and direction of brain shift will be described in the next section.

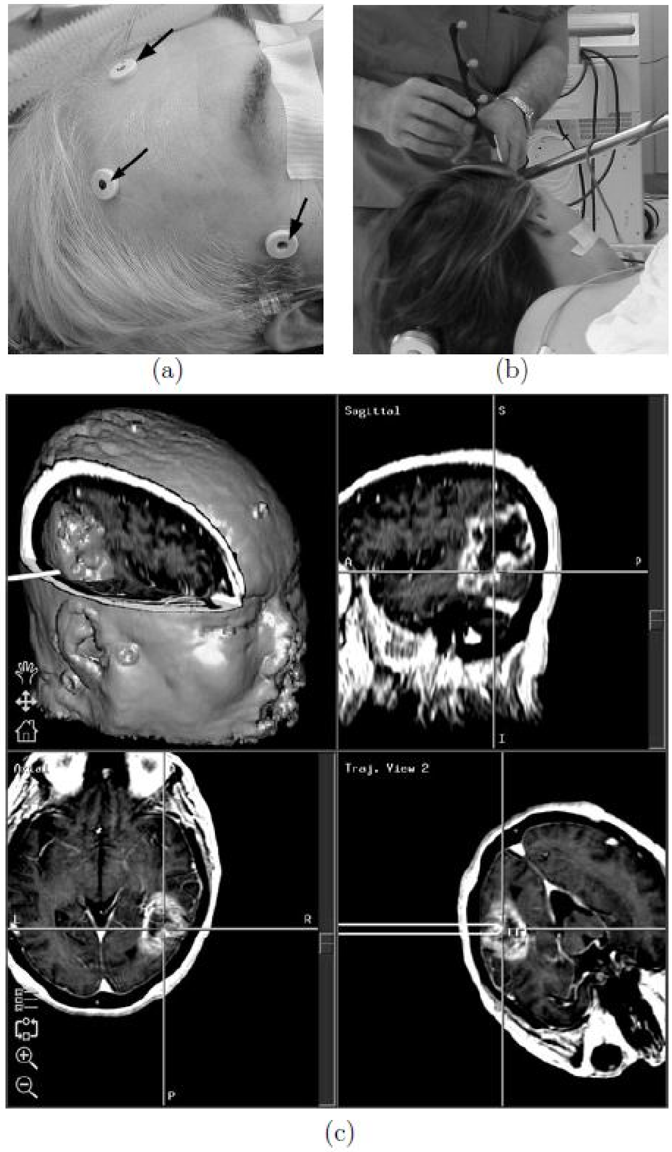

Figure 1-4 Pictorial description of image-guided surgery: (a) Fiducials (arrows) are attached to a patient's scalp to correlate the patient's surface anatomy with the preoperatively obtained image data set; (b)These fiducials are localized in the OR prior to surgery. (c) After patient registration, three-dimensional reconstruction, sagittal, axial, and trajectory views demonstrate a left parietooccipital tumor. This display aids surgical planning[6].

1.4 Brain Shift: magnitude and direction

As assumption aforementioned for IGNS is that the brain is *rigid* and *brain shift* during surgery compromises the accuracy of current IGNS systems. An example of brain shift on IGNS is shown in Figure 1-5, in which the brain shift caused by a retractor blade.

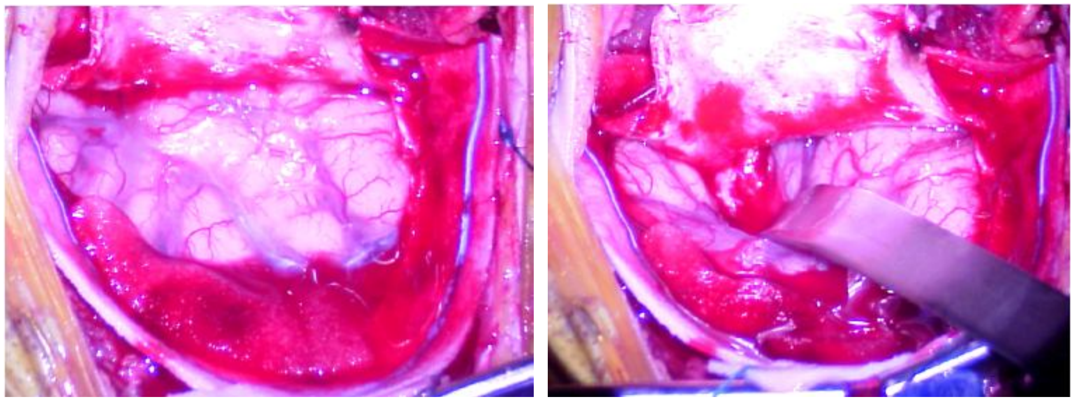

Figure 1-5 The cortical surface of the same patient viewed through the operating microscope immediately after the opening of the dura (left) and during the tissue retraction (right). Note the significant tissue deformation induced by the retractor blade[6].

A lot of research reports have revealed the investigation of the magnitude and direction of brain shift during surgery.

Nauta *el al.* first quantitatively reported brain shift during surgery[7]. In their work, two stereotactic localization systems were used to quantify brain shift in a patient undergoing resection of "an extremely small" tumor. As a result, the difference in localization because of brain shift was reported to be approximately 5 millimeters. Later, a preliminary research done by Hill *et al.* reported brain surface shift in 5 patients, with serial measurements in 2 of the 5 in 1997. In their work, OPTOTRACK began to be used for localization of surface points intraoperatively with a mean number of surface points of 25.57 ± 27.96. Their result indicated the brain shift on the order of a centimeter and brain shift increased over the course of the surgery with serial surface localizations. In 1998, they further extended the patient population size to 21 patients and recorded time-course measurements for each patient[8]. Their new result indicated a mean brain surface shift of 3 millimeters with a max of 8 millimeters before removing of the dura. Also, they reported that the brain surface of each of the patient sank on an average 10 millimeters. Then they pointed out that the brain shift during surgery was significant surprising and it was necessary to enhance the current image-guided neurosurgery (IGNS) systems.

Besides, some intraoperative image sensors have been used to measure the brain shift. The first intraoperative ultrasound (iUS) image measurements system for brain shift was reported by Bucholz *et al*[9]. To measure the brain shift, a calibrated ultrasound and optically tracked probe was used. Some features in serial ultrasound image, such as cross-section point of vessel, were measured to quantify the shift. Bucholz *et al*. applied this iUS measurement technique for brain shift to 23 patients undergoing different surgeries. They reported that the average shift observed was around 7.3 ± 5.8 millimeters. Similar to Hill's result, Bucholz also reported that the brain shift increased over the duration of surgery. Finally, their brain shift analysis provided an evidence to support the development of an iUS method to compensate for brain shift.

Besides using iUS, Maurer *el al.* were one of the first to use intraoperative magnetic resonance imaging (iMR) to demonstrate the effects of brain shift during surgery[10]. In their work, five patients undergoing tumor resection therapy were recorded. Little quantitative result was reported in their paper. Later, Hartkens *et al*. further extended Maurer's work to 24 patients within a paper published in 2003[11]. In Hartkens's work, a 3D deformation volumetric registration algorithm was implemented. Because of the 3D non-rigid registration, the corresponding feature point between the preoperative patient data and the intraoperative MR imaging was obtained. This corresponding mapping can allow Hartkens to calculate 3D shift of the brain, as well as volumetric change during the whole surgery. Also, their result presented an approach to correct brain shift during surgery using iMR, which will be discussed later in this chapter.

Meanwhile, Hartkens[11] *et al.* pointed out that the brain shift direction was related to gravity. Three cases of the patients are shown in Figure 1-6. In Figure 1-6, the white arrow represents the gravity direction. The distribution of the displacement vectors of one surgery case is shown in Figure 1-7. The displacement vectors are visualized as points in the 3-D coordinate system whereby the axes represent the components of the vectors. Displacement vectors with a magnitude of less than 1 mm are not shown in this diagram. The large vector in the diagram represents the first axis of the Principle Component Analysis (PCA). The variance in direction of this vector is a measure for the magnitude of the displacement field. The other two axes of the PCA are visualized in relationship to the variance of the first axis. Because the variance in their direction is very low in comparison to the first axis, they can hardly be seen in this visualization. The main brain shift direction can be seen along the Z direction (Z is the gravity direction).

Further, Dorward *et al*. indicated that the brain shift not only happened in surface points but also in deep tissue points with measurement of 48 patients[12]. In their experiment, five points were selected for each patient during surgery: on the dura at the center of the craniotomy, at the deep tumor margin after resection, on the surface of the skull at the center of the craniotomy and on the surface of the cortex adjacent to the tumor before and after resection. Their reports indicated that the mean surface shifting for all patients at opening and closing were 4.6 and 6.7 millimeters, respectively; also they pointed out that the deep tissue shift for all the patients were 5.1 millimeters on average. Dorward *et al.*' results revealed the complex deformations of the brain shift phenomenon.

The results of all the aforementioned papers demonstrate the complexity of brain shift and the major factors and effects of brain shift during surgery. Although the individual measurement result varies from patient to patient in each experiment, the general trend indicates that the brain surface shift is *on the order of centimeters and deep tissue shift is on the order of 5 millimeters*. Also, the direction of brain shift is generally parallel to the gravitational direction and the brain shift is time dependent. This amount of error could cause error thus the compensation of brain shift is one of the biggest issues to improve the accuracy of IGNS.

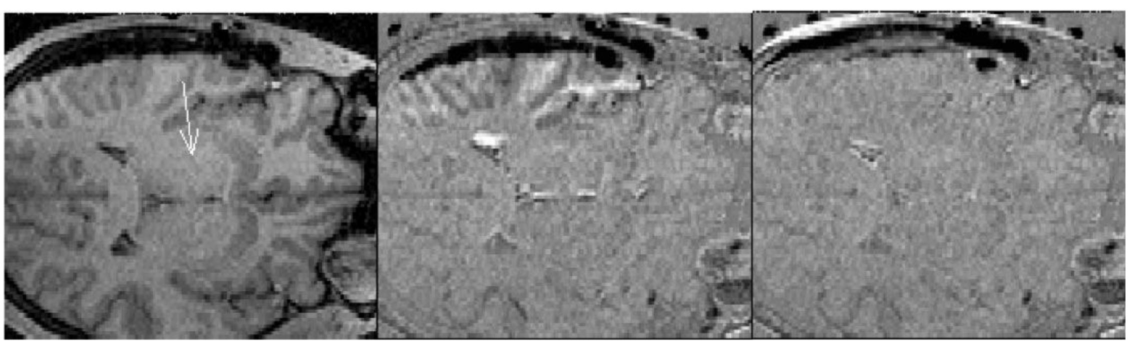

(a)

(b)

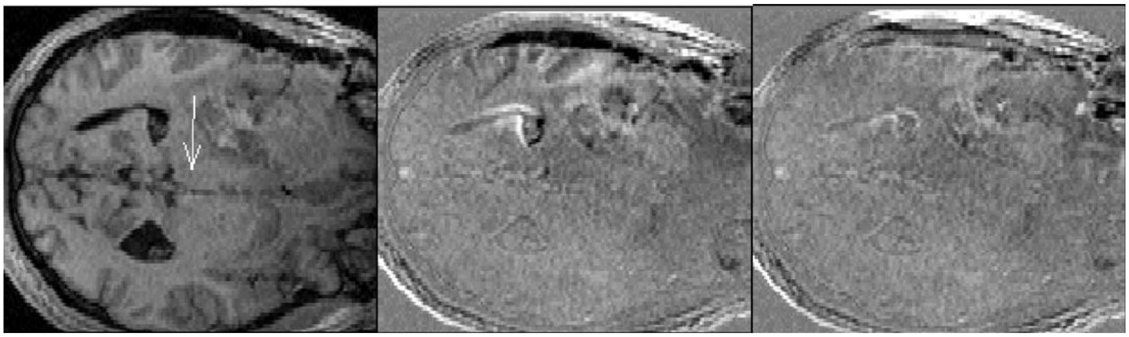

(c)

Figure 1-6 Brain shift direction. (a) (b) and (c) are 3 cases of brain surgery. The white arrow showed the brain shift direction. Also, the gravity direction points to the down direction[11].

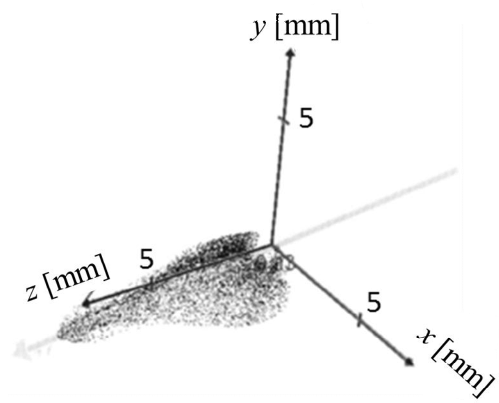

Figure 1-7 PCA analysis of the brain shift magnitude. X, Y, Z are the three coordinates. The black point is the brain shift point coordinate[11].

1.5 Compensation of Brain Shift for IGNS

From the previous description, it is noticed that the brain shift phenomena have been extensively researched and it compromises the accuracy of current IGNS systems. As a result, some efforts have been focused on the improvement of current IGNS systems by compensating the brain shift. In this section, we will briefly introduce some previous techniques to improve the accuracy of IGNS during surgery by compensating brain shift.

1) Marker based on brain shift compensation method

The main purpose of IGNS is to accurately locate the patient brain and surgeon's instruments during surgery through registration. Such kind of locating process is to help the surgeon to know where the brain tumor and eloquent area are. In the early stage of this research, marker based method is implemented as a direct but manual way to demarcate such key area during surgery. Until now, there are two kinds of markers used in IGNS system for assisting surgeon according to the position and function they used for: micropatty marker and catheter marker.

In 1991, Hassenbusch *et al.* demonstrated a marker based method to account for brain shift during resection[13]. The method outlined used surgical micropatties (Surgical Patties. 1/4× 1/4 inch. Codman & Shurtleff. Inc. Randolph. Massachusetts) with string tails tethered to them. A series of patties, shown in Figure 1-8, were placed under stereotactical guidance around the tumor margin. The micropatty can demarcate the brain key area during surgery. The tails of the marker work for 2 purposes: 1st locating the corticotomy 2nd following the tail to the tumor and then to the micropatty at the deep tumor edge. The advantage is that the tails of the patty markers lead directly to the tumor bulk and then to the edges. Accordingly, cumbersome additional equipment is not needed to resect deep-seated tumors. Moreover, the author mentioned that the marker system is very cost-effective.

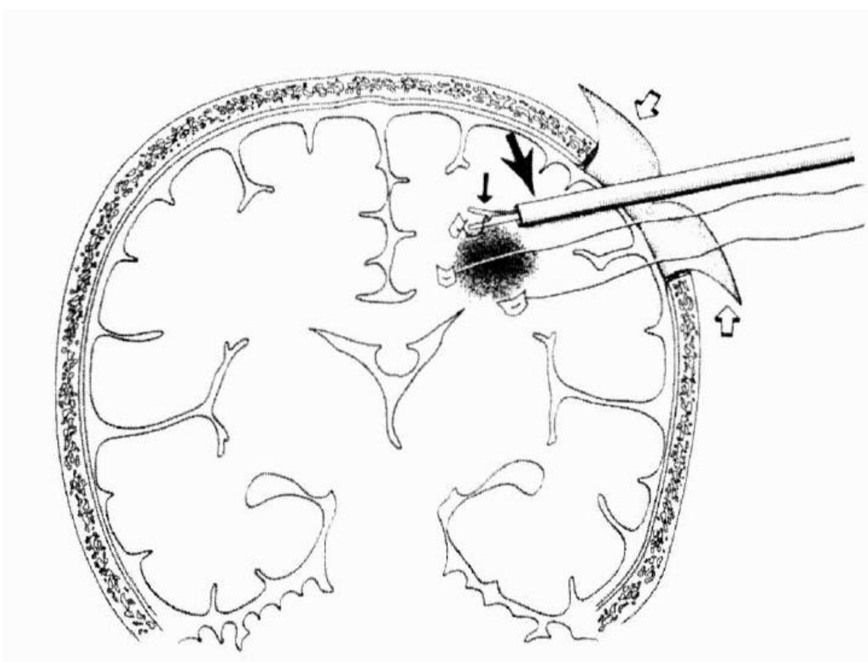

Figure 1-8 Diagrammatic description of the stereotactic placement of a "micropatty" with attached "tail" extending out through the brain and the site of the durotomy add the craniotomy[13].

Later, another kind of marker was used for brain surgery[14]. The second marker is silicon tube. By inserting the silicon tube around the tumor or the eloquent area, the surgeon can realize which part of the exposure surface is important, as suggested in Figure 1-9 and one clinical situation in Figure 1-10 . This kind of marker system works as: 1st the entry and target points were decided; 2nd an adequate number of silicon tubes are inserted under the guidance of the navigation system; 3rd the tumor mass is resected under the guidance of the silicon tube. Using this kind of marker, the tumor mass can be extirpated without seeing a tumor margin.

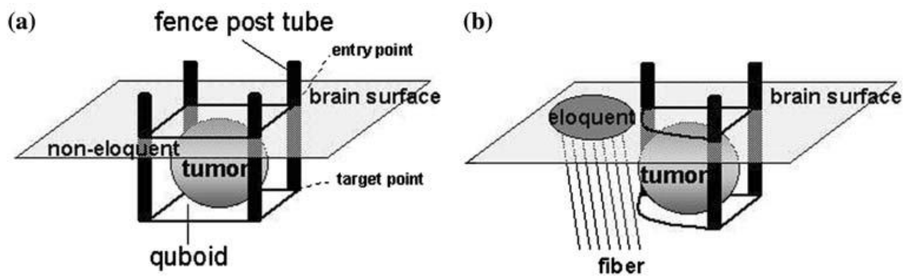

Figure 1-9 Scheme of the silicon marker[14].

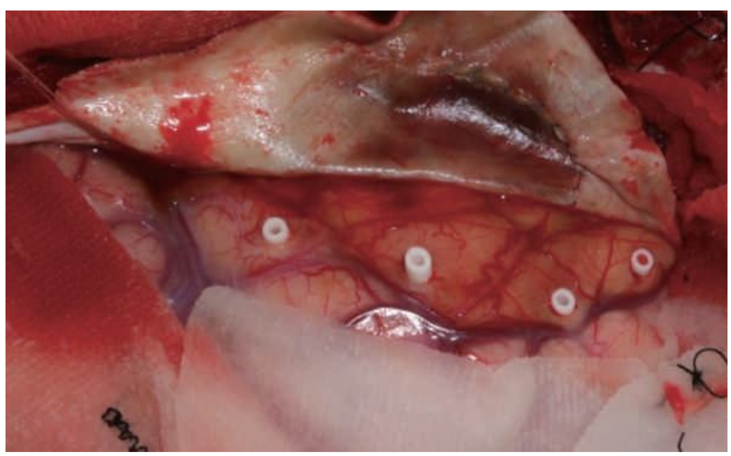

Figure 1-10 Clinical situation used the marker[15]. The white silicon tubes were inserted into the patient's brain

However, these marker-based technologies suffer from some problems: 1st: the marker system highly depends on the accuracy of placing the marker on/into the patient; 2nd: the marker based system is an invasive approach, which should be avoided during surgery; 3rd: in the micro-patty marker system, the tail might disturb the attention of surgeon. Because of such inconveniences and problems in marker-based method, the marker-less tracking for brain surface is extremely developed in nowadays.

2) Intraoperative imaging for compensating brain shift in IGNS

One of the effective marker-less approaches is intraoperative imaging technique. Usually, surgeons intuitively estimate the intraoperative brain surface deformation during surgery and compensate for brain shift intuitively, which is actually a factor of inaccuracy and biases. Some surgery centers further acquired reduced-quality intraoperative images at several critical times during surgery, in an attempt to track brain deformations during surgery. Those reduced-quality intraoperative images are then added to IGNS systems by adapting a rigid registration between them and preoperative images. This rigid registration aligns the preoperative images with the intraoperative images in the same coordinate, however, it still failed to compensate the brain shift since only rigid registration is performed. Surgeons still need to intuitively deform the preoperative images, although it is easier with the intraoperative images since they have an image of the brain deformed. As a result, non-rigid registration between the intraoperative images and preoperative images is required. This non-rigid registration would align the preoperative images according to the deformation of the intraoperative images and the preoperative images would then be successively updated.

One issue for implementation of intraoperative images is what type of intraoperative image should be used. Nowadays, various intraoperative image sensors have been investigated to capture intraoperative deformations correctly, such as intraoperative MR (iMR), intraoperative CT (iCT) and intraoperative US (iUS).

Intraoperative MR images is an imaging technology used to track brain shift [16-40] during surgery. For instance, in reference [21], the preoperative and intraoperative MR are aligned by maximizing the Mutual Information (MI). One example of iMR is shown in Figure 1-11. iMR can either be acquired by using interventional scanner in OR[21] or moving patients between OR and the adjacent scanning room[41]. However, intraoperative MRS is expensive and it also needs expensive surgical instruments. The scanners have poor spatial resolution and the generated image often suffers from geometric distortions. Because of these reasons, intraoperative MRs have not been widely used in brain surgery applications. Another approach is moving the patient out of the OR for scanning which might further complicate the procedure and it is also not very commonly adopted. Moreover, the resolution of intraoperative MR images is often lower than that of the standard diagnostic scanners.

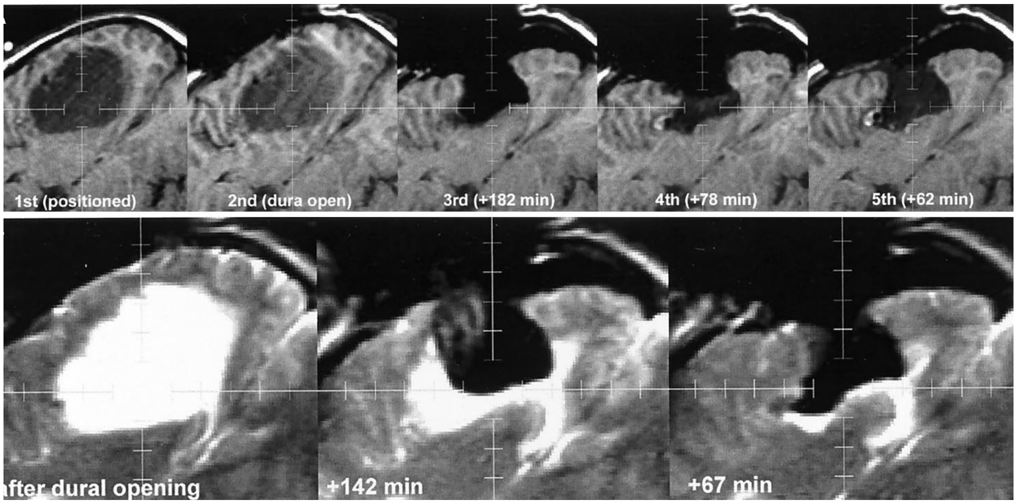

Figure 1-11 iMR image used in brain surgery[21]

Another IGNS uses intraoperative CT (iCT) images[42-47]. The first iCT was made by the University of Pittsburgh for minimally invasive brain surgery[48]. Recently, a new mobile CT scanner with wheels was developed at Harvard[49]. In 2007, a new system named BrainSuite iCT, integrating Siemens's Miyabi CT with BrainLab's computer-aided surgery equipment was developed for the first time. However, it is still costly to adopt them for common use. For that reason, a new portable low dose xCAT ENT has been introduced. The dimensions of the scanner are smaller than traditional CT scanner. Moreover, the CT images with slice thickness as low as 0.4 mm can be produced. This scanner is good for providing guidance for the surgeon with better resolution but the soft tissue contrast is not as good as diagnostic scanners. One example of the iCT image is shown in Figure 1-12.

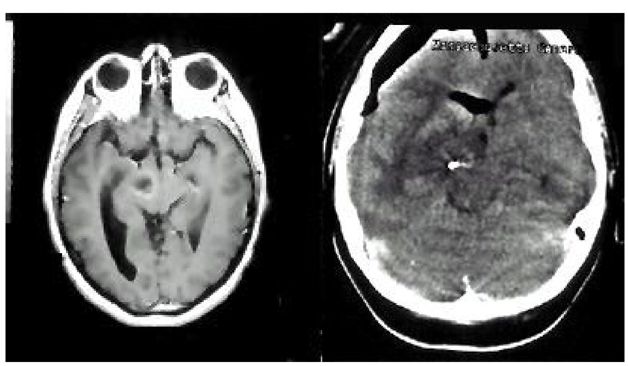

Figure 1-12 The iCT image in brain surgery[50]

Compared to iMR and iCT, the iUS has gathered a lot of attentions for the reason that it is cost-effective and safe[51-65]. In 1989, Leroux *el al.* measured the difference in tumor volumes predicted by pCT and iUS[66]. They pointed that using ultrasound can enhance the selection of resection margins during surgery. In 1997, Bucholz *et al.*[9] proposed to use iUS to correct brain shift and demonstrate the ability of iUS to capture, register and measure brain shift by using 2D US images. They further predict the ability of iUS in 3D space. A research group from Canada demonstrated the ability to acquire 3D iUS image to register the intraoperative data to preoperative images by incorporating image warping technology[67-69]. The current iUS, however, suffers from low signal-to-noise (SNR) which limits its effectiveness during surgery.

Overall, the intraoperative image technologies described in this section failed to provide quantitative brain shift compensation by themselves. Rather, the brain shift compensation springs from the surgeon's expertise and is performed in a qualitative manner. Accordingly, model-updated image guided neurosurgery (MUIGNS) is proposed to compensate brain shift in a quantitative manner.

3) IGNS developed to track brain shift using model-updated image

The idea of MUIGNS is that the pre-operative data could use intraoperative data to deform algorithmically in order to provide accurate feedback of the position and shape of the brain during surgery. At the beginning, Roberts *et al.* used a computational model that could predict the motion of brain under loading conditions in the OR. There has been quite a lot of research related to computational model since Roberts's research [70-87]. Also, some other mathematical methods could be used for the matching of intraoperative data and preoperative data, such as atlas based modeling of the brain shift[88] or interpolation of shift [89]. For the computational models, one of the most accurate models of brain shift has been proposed by a group at Dartmouth. The model adapts Biot's theory of consolidation and likens the brain to be a sponge. Nowadays, computer technology could make the model calculation real-time.

For the implementation of MUIGNS, one critical issue is the accurate acquisition of intraoperative data. The intraoperative data is renamed as *sparse-data* in this area since the data has limited information or extent. Each of the intraoperative imaging method described above could be used for the sparse-data acquisition. However, as aforementioned, iMR images are expensive and could interfere with the neurosurgical workflow, leading to barriers to its widespread acceptance; iUS is less expensive but provides relatively poor image quality. Recently, efficient methods to acquire the brain surface using non-contact range-sensing for the brain surface is widely researched.

One of the technologies for measuring the brain surface data during surgery is stereovision [6, 34, 90-94]. This method provides the brain surface with information in a non-contact fashion by using a pair of calibrated cameras. Another textured brain surface measurement method, the laser range scanner (LRS), has been used in brain surgery to capture the brain surface with texture image [95-110]. The brain surface, measured by stereovision or LRS, is used by the MUIGNS system for model deformation driven by registration between intraoperative captured images or registration between the preoperative image and intraoperative image. Our research in this dissertation is mainly focusing on the intraoperative brain image registration for tracking the brain surface deformation for MUIGNS to update the brain model to guide brain surgery. The previous methods on intraoperative brain-surface registration will be described in next section.

1.6 Previous Methods on intraoperative brain-surface registration and their problems

The previous intraoperative brain registration methods could be classified into 2D image registration methods and 3D registration methods according to the registration image dimension.

1) 2D image registration methods

The researchers in Vanderbilt University proposed a method to register brain image before and after tumor resection. In their method, they take the advantage of vessel texture and the vessels are considered to be the texture point and segmented using Frangi filter[111]. Then the corresponding points between the vessels from two brain images are estimated by Robust Point Matching (RPM) algorithm. After obtaining the corresponding points, the whole image is deformed by the Thin-Plate-Spline (TPS) interpolation method[101]. The mathematical description is shown below:

$$\frac{\min}{f} E(f) = \frac{\min}{f} \sum_{a=1}^{K} \| y_a - f(v_a) \|^2 + \lambda \iint [\frac{\partial^2 f}{\partial^2 x} + 2(\frac{\partial^2 f}{\partial x \partial y}) + \frac{\partial^2 f}{\partial^2 y}] \mathrm{d}x\mathrm{d}y \tag{1-1}$$

In that function, y_a is the control point and f if the transformation that needs to be calculated and $f(v_a)$ is the estimated corresponding point. The first part of the function tries to find the corresponding point while the second part of the function tries to constraint the shape so that it deforms smoothly. Afterward, they further extended this method into a vessel based video tracking method for 2D-brain image tracking[100]. They introduced a vessel-ness and intensity combined feature point extraction in the brain image tracking. The feature can be seen in the following equation:

$$\mathbf{F}=\begin{bmatrix} R_{-r} & R_{-r+1} & \dots & R_r \\ G_{-r} & G_{-r+1} & \dots & G_r \\ B_{-r} & B_{-r+1} & \dots & B_r \\ 3V_{-r} & 3V_{-r+1} & \dots & 3V_r \end{bmatrix} \tag{1-2}$$

Where *R, G, B* is the pixel intensity value on RGB channel; V is the vessel corresponding value of the pixel evaluated by Frangi filer; *r* is the length of a line perpendicular to each center line of the detected vessel. Their clinical evaluation results showed that they can track brain surface image well even when there are some occlusions. An example of their vessel based brain surface tracking is shown in Figure 1-13.

In summary, the TPS based 2D brain registration is composed of the following steps:

1) Texture/Feature point extraction from the 2D image.

2) Texture/Feature corresponding point estimation.

3) The whole image deformation by TPS by considering the texture/feature point as the control point.

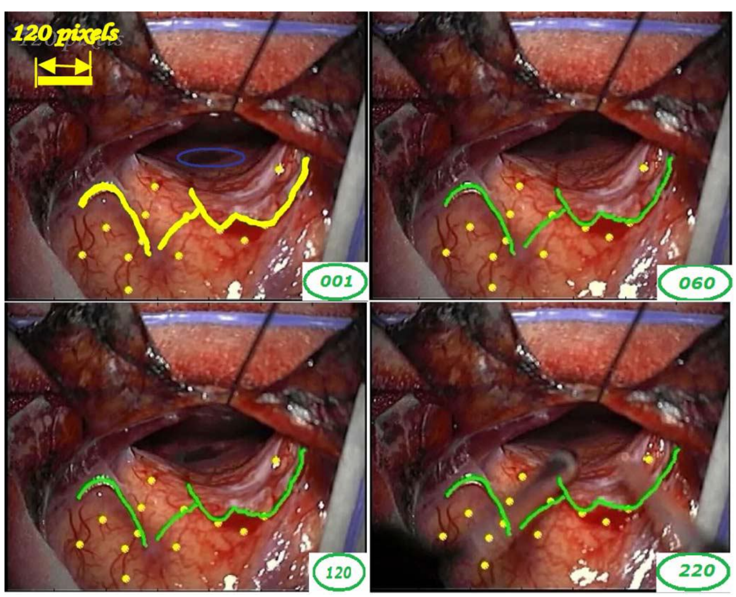

Figure 1-13 An example of Ding's vessel based brain image tracking. The series images showed the vessel tracking result, in which the yellow line is the initial vessel and the green line is the tracking result[100].

Furthermore, Ji *et al.*, another research group in Dartmouth College, proposed to adapt the optical flow based registration for brain surface registration[93]. Similar to TPS based method, his method also contains corresponding and deformation constraints. The mathematical description is shown below:

$$E(u,v) = E_{\text{data}} + \alpha E_{\text{smooth}}$$
$$E_{\text{data}} = \int \psi(|I(\mathbf{p}+\mathbf{w}) - I(\mathbf{p})|^2)d\mathbf{p} \qquad (1\text{-}3)$$
$$E_{\text{smooth}} = \int \phi(|\nabla u|^2 + |\nabla v|^2)d\mathbf{p}$$

Where $\mathbf{p} = (x, y, t)$ and the underlying flow field, $\mathbf{w}(\mathbf{p})$ is given by $\mathbf{w}(\mathbf{p}) = (u(\mathbf{p}), v(\mathbf{p}), 1)$, where $u(\mathbf{p})$ and $v(\mathbf{p})$ are the horizontal and vertical components of the flow field, respectively. E_{data} means the cost for the constancy assumption while E_{smooth} constraint the shape to deform smoothly. In the smooth energy, $|\nabla u|^2 = u_x^2 + u_y^2$ with $u_x = \frac{\partial}{\partial x}u, u_y = \frac{\partial}{\partial y}u$ and ∇ is the gradient operator. Because the flow field in a natural scene is typically smooth and by applying the smooth constraint, the brain can deform smoothly. Their method was evaluated by 18 clinical surgical cases and their result shows that their proposed method achieved an accuracy around 1mm on average compared to the OPTOTRAK measured results. One example of Ji's method is shown in Figure 1-14.

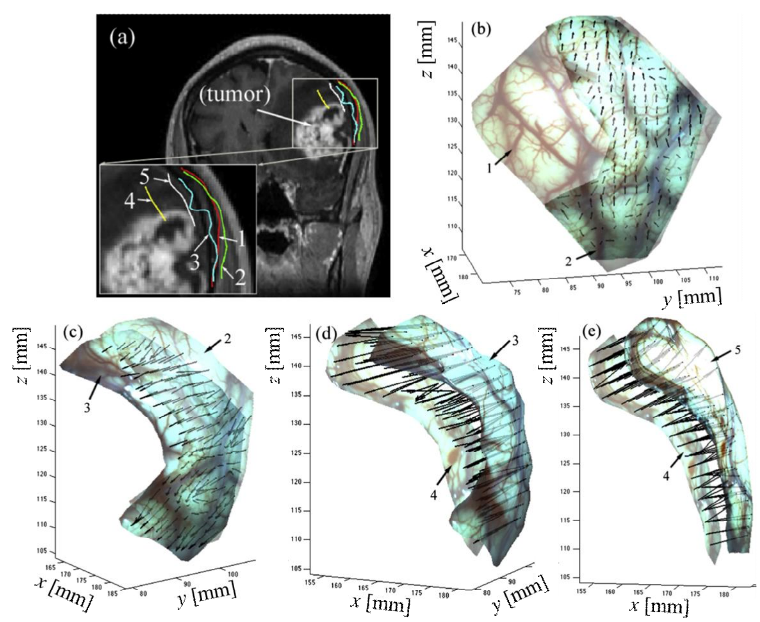

Figure 1-14 Cross-sections of cortical surfaces reconstructed from iSV at five-time points during surgery on the same coronal pMR image showing the progression of the exposed cortical surface during tumor resection for patient 11 in (a). The resulting 3D displacement[93]

Ji *et al.*'s method, however, highly depends on the intensity of the brain image since they assumed that the intensity of brain image remains constant during surgery. However, this challenging assumption could not hold solidly in the clinical situation[112]. To solve this problem, Faria *et al.* further extended Ji's method using normalized cross correlation (NCC) to track brain surface 2D image through stereovision system[113]. NCC was used to find the corresponding between the stereovision image pair and successive images for tracking. They proposed an iSV based on brain surface reconstruction and tracking method, which is robust to intensity variations. However, this method is based on the assumption that the motion of the feature between frames is limited, and it fails when significant deformations occur.

A 2D image should be mapped to a 3D space to compensate for brain surface deformation, and interpolation is usually required when resolutions of the 2D image and 3D point are different. In addition, 2D image distortion might contribute to displacement errors in the physical space. Therefore, registration between intraoperative 3D brain surface images is a direct method of tracking brain surface. Some researchers have proposed to use 3D shape instead of the 2D image for the registration, which will be described in the following section.

2) 3D surface registration methods

To track brain surface, Sun *et al.* assume that the brain did not contain large deformation in the surgery and the Iterative Closest Point (ICP) rigid registration method is used to register the brain surfaces[6, 94].

$$\min_{\mathbf{R},\mathbf{t}} E(\mathbf{R},\mathbf{t}) = \min_{\mathbf{R},\mathbf{t}}[\sum_{i=0}^{N} \| \mathbf{p}_i^{\mathrm{cor}} - (\mathbf{R}\mathbf{q}_i + \mathbf{t}) \|^2] \tag{1-4}$$

In the function, $\mathbf{q}_i$ is the source point and $\mathbf{p}_i^{\mathrm{cor}}$ is the considered closest point, $\mathbf{R}$ and $\mathbf{t}$ are the rotation matrix and translation matrix. In Sun's method, only the surface is used for the registration, and the two surfaces are aligned in order to achieve a minimal surface alignment error. However, surface information alone might fail in surface registration when the surface has large deformation. Then the non-rigid surface registration method is needed.

Furthermore, vessels, as the most readily visible structures on the brain surface, have also been used for brain surface registration [96, 100-102, 104, 114-116]. For example, Marreiros *et al.* proposed a non-rigid deformation pipeline for compensating superficial brain shift using superficial blood vessels as landmarks. They used the coherent point drift (CPD) to determine the correlation between intraoperative vessels and preoperative vessels from magnetic resonance angiography and then used TPS to generate volume deformation, the equation is described as equation 1-5, where v_a is the point (x,y,z); y_a is the estimated corresponding and the second part is the constraints. Moreover, Cao *et al.* also proposed a non-rigid registration method using 3D vessel information registration by RPM to find the corresponding points. Similar to Marreiros's method, TPS was implemented to generate a global deformation calculated by 3D vessels corresponding between two shapes. The influence of surrounding materials could be decreased by integrating vessel structures[104]. An example of Cao's method is shown in Figure 1-15. Through evaluation of the RE and TRE, their results showed that the RE is 0.4 mm while the TRE is around 4 mm.

$$\frac{\min}{f} E(f) = \frac{\min}{f} \sum_{a=1}^{K} \| y_a - f(v_a) \|^2 + \lambda \iint [\frac{\partial^2 f}{\partial^2 x} + \frac{\partial^2 f}{\partial^2 y} + \frac{\partial^2 f}{\partial^2 z} + 2(\frac{\partial^2 f}{\partial x \partial y}) + 2(\frac{\partial^2 f}{\partial x \partial z}) + 2(\frac{\partial^2 f}{\partial y \partial z})] \mathrm{d}x\mathrm{d}y\mathrm{d}z \quad (1\text{-}5)$$

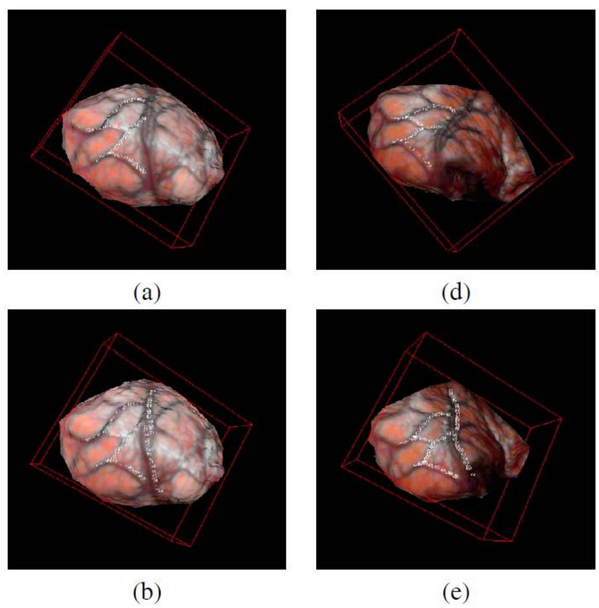

Figure 1-15 Registration result of Cao's result by using the vessel. (White line is the vessel used for registration)[96]

The LRS and stereo-system can offer textured brain surface which Perrine Paul *et al.* Took advantage of [117]. They proposed a surface combined with intensity method. In their method, a corner detection based on marker can be used to register the 3D surface. An energy function containing surface Euclidean distance, intensity Euclidean distance and land marker Euclidean distance were proposed to register the brain surface, as shown in equation 1-6.

$$F(\mathbf{P}_i, \mathbf{P}_j) = \beta\alpha A(\mathbf{P}_i, \mathbf{P}_j) + (1-\alpha)B(\mathbf{P}_i, \mathbf{P}_j) + (1-\beta)C(\mathbf{P}_i, \mathbf{P}_j) \quad (1\text{-}6)$$

Where, A is related to the image intensities; B is related to the Euclidean distance between surfaces; C is related to the Euclidean distance between landmarks. Their method was compared with ICP based registration method by one clinical surgical cases. **P** is the 3D point position. The result showed that the method can achieve an accuracy of 2.2 ± 0.2 mm while the result of ICP method is 5.8 ± 0.9 mm. An example of land-marker detected for registration is shown in Figure 1-16.

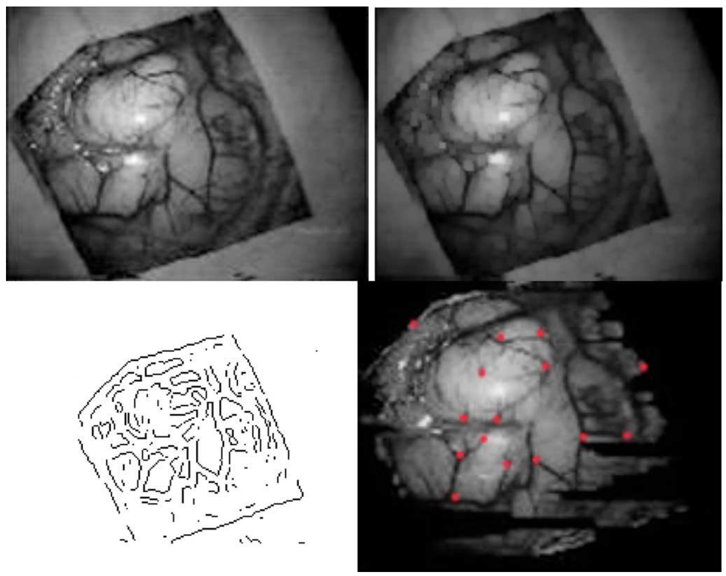

Figure 1-16 Lander marker detection based on brain surface tracking[117]. The red dot is the detected corner points for registration during deformation tracking.

3) Problems in previous methods

As mentioned above, some previous methods have been proposed to track brain surface in experiment setting up or clinical situation. According to the image dimension used, the previous methods can be divided into 2 categories: 2D/2D registration method and 3D/3D registration method. However, they suffered from some problems, which will be described below.

a) Problems in previous 2D registration methods

In Ding's TPS-registration method, they use the vessel to obtain the corresponding of the control points and the whole image is deformed by TPS interpolation [100-102]. TPS is a linear space interpolation method and when the vessels are few the registration will lead to a bad result. Also, when the image pixel point is far away from the vessel but has large deformation, their method also might fail in such registration case. In the energy function, as seen in equation 1-1, there are only 1 parameter λ, which is used to constraint the deformation and it is easy to shrink the image. Further, Ding extended the method to intensity and vessel feature based video stream brain image tracking. In this method, the continuous video stream is needed to identify and track a set of vessels which means additional image processing is demanded when sudden appearance/disappearance of blood or surgical tools occurs in the field-of-view. Also, because of adapting TPS, the previous disadvantage of TPS has not been overcome.

Optical Flow based on registration method, proposed by Ji *et al.*, is established on the assumption that the intensity of the image remains constant in the surgery[93]. However, the OF algorithm can fail or result in displacement artifacts when the gray value constancy assumption no longer holds. For example, displacement artifacts occurred when no physical correspondence existed for pixels near the craniotomy in the synthetic undeformed image when it was radially stretched outward within the craniotomy[112]. This disadvantage can be avoided by using the normalized cross correlation (NCC)[113] based on feature point tracking method proposed by Faria *et al.* However, the NCC based on method assumed that the motion of the feature between frames is limited, and it fails when significant deformations occur.

b) Problems in previous 3D registration method

In the 3D registration methods, Sun's registration method assumes that the brain did not deform largely in the surgery. Accordingly, they apply a rigid ICP method to register the two surfaces. However, if the brain has large deformation, the ICP method would fail in such kind of situation because large deformation usually happens in brain surgery [94]. Also, the ICP method only considers the shape information, which will easily cause the sliding error along the surface, as suggested in Figure 1-17. In Figure 1-17, (a) is an example of source with curve texture on it; (b) is the target surface with same texture on it; (c) is one of the registration results. And the curve line serves as the texture during registration. As suggested in (c), even the surface can achieve good alignment while the texture remains sliding error on the surface. Accordingly, 3D surface registration combining texture is necessary to overcome the problem of shape-using only registration method.

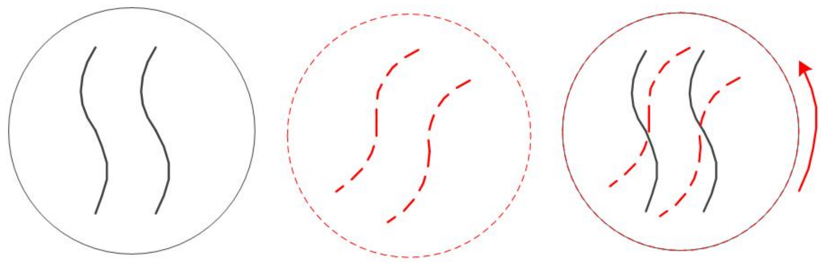

(a) Source (b) Target (c) Registration

Figure 1-17 An example of registration sliding error using only the surface. (a) is source surface and (b) is target surface. (c) shows one of the surface alignment with a sliding error caused.

Cao's TPS based 3D shape non-rigid registration method also inherits the disadvantage of Ding's 2D image registration method[104], as described in equation 1-5. As mentioned above, the 3D vessel was considered as the texture and the control point in the registration. By applying Robust Point Matching method (RPM), the corresponding pair of the intraoperative vessels can be estimated. Then the estimated corresponding of vessels drives the brain surface deform using TPS, the same interpolation method used by Ding *et al*. Their results showed that the brain registration will get more registration error when few vessels are presented.

In Paul's 3D brain surface registration method, they combined a corner detection feature, surface Euclidean distance and intensity Euclidean distance for the registration of the shape[117], as described in equation 1-6. In their energy function, they only give the energy cost for the corresponding cost and did not offer the surface deformation constraint. Then their method is easy to make abrupt shape change and shape shrinking. On the other hand, they use the corner feature which needs a continuous video stream. If there is any interruption of the video, the feature tracking will fail.

In summary, the previous methods suffer from sliding error[6], large error occurred far away from texture[90, 96, 101], the assumptions on some special conditions (intensity keep constant[90] or feature remain similar in frames[113]). A 3D non-rigid registration method which combines shape and texture, robust to texture-feature numbers change and extend of deformation, was proposed in this dissertation. We proposed a novel approach using both surface shape and texture. Registration method using only the shape can compensate the brain deformation in the direction vertical to the brain surface. It, however, could cause surface sliding error along the surface. On the other hand, using texture information for registration can compensate the brain deformation/motion along the brain surface direction. Thus, by combining the texture and shape, the proposed method can register the deformed brain surfaces while reducing the surface registration sliding error.

1.7 Objective

In order to track brain surface during deformation and reduce sliding error along brain surface, this research proposed a new non-rigid registration method by integrating shape and texture information. The shape and texture information were simultaneously obtained by an implemented phase-shift measurement system. By integrating shape and texture information, the proposed non-rigid registration method achieved higher tracking accuracy compared to previous methods. The contributions of this dissertation include the following aspects:

1) A marker-less approach to tracking brain surface

As described before, the traditional marker-based tracking system is an invasive approach, cumbersome and time-consuming work. Moreover, the marker based tracking system highly depends on the accuracy of the placing markers. Thus, we offered an imaged based marker-less approach to tracking brain surface deformation. The advantages of the proposed mark-less approach is that it's a non-invasive and effective approach to tracking brain surface. More, the assisted equipment of accurately placing markers on the brain surface is not needed.

2) A phase-shift based brain surface measurement system for textured 3D brain surface measurement

A phase-shift 3D surface measurement system [118, 119] was implemented to measure the brain surface and capture the texture simultaneously in this dissertation. The implemented phase-shift 3D surface measurement system is composed of a high speed camera and a projector. The projector can project phase-shift patterns onto the brain surface and the high speed camera can capture the brain surface texture information. Different to the previous brain surface measurement systems (stereovision [90, 91] and LRS [96, 100, 101, 105, 107, 109]), phase-shift method usually generates a dense 3D surface and one to one pair corresponding between the texture point and 3D point. Phase-shift [118, 119] uses the wrapped phase information to find the corresponding point between camera image pixel and projector image pixel. Then the textured brain surface could be obtained after triangulation. Meanwhile, the intensity variation on the brain surface is strong and the implemented phase-shift 3D measurement is robust to texture change which is vital in our brain surface measurement.

3) Marker-less tracking brain surface by non-rigid registration combining shape and texture.

In this dissertation, we proposed a novel approach to tracking brain surface by non-rigid registration combing surface shape and texture. Registration method using only the shape can compensate the brain deformation in the direction vertical to the brain surface. It, however, could cause surface sliding error along the surface. On the other hand, using texture information for registration can compensate the brain deformation along brain surface direction. Thus, by combining the texture and shape, the proposed method can register the deformed brain surfaces in both perpendicular to the brain surface and along brain surface direction, while reducing the surface registration sliding error.

1.8 Thesis Organization

The following parts of the thesis are comprised of four parts: system introduction, non-rigid registration method, experiment and result, conclusions and acknowledgment.

In chapter 2, our system configuration, the phase-shift measurement, the projector projection and system calibration are introduced.

In chapter 3, the non-rigid registration method including texture segmentation, corresponding estimation, deformation constraint, optimization and interpolation were described.

In chapter 4, the 3D shape measurement and non-rigid registration method were designed and described in this chapter to evaluate the accuracy of our method and system.

A discussion will be given in chapter 5 and a conclusion will be given in chapter 6. Finally, an acknowledgment will be given in Chapter 7.

2 Method

In this chapter, the system configuration, 3D surface measurement method, projector projection method and system calibration are introduced.

2.1 System Configuration

In our system, we implemented the phase-shift 3D shape measurement system to measure brain surface with texture. Our 3D surface measurement system is comprised of a projector and a camera. The implemented phase-shift measurement system can acquire textured brain surface by projecting phase-shift pattern and analyzing the modulated 2D image pattern, as shown in Figure 2-1.

Figure 2-1 (a) shows the projector-camera system configuration. The camera (IDP Express R2000, Photron Inc.) and projector (SHOWWX, MICROVISION Inc.) used in our measurement system are shown in Figure 2-1 (b) and (c). The camera is used to capture the real-time images while the projector is used for the phase-shift pattern projection and the brain mapping information projection.

The specific parameters of projector and camera are listed in Table 1.

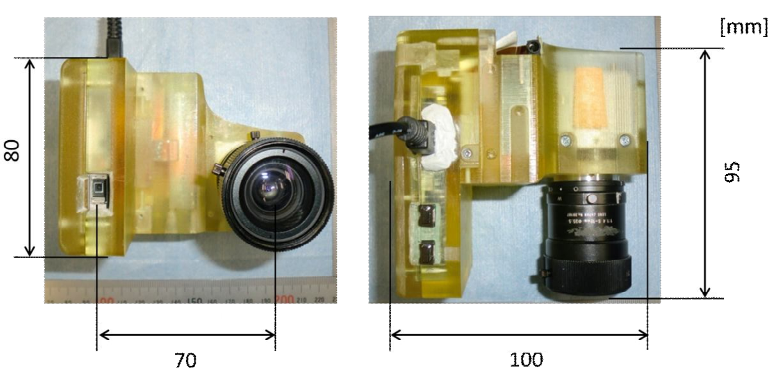

(a) System configuration

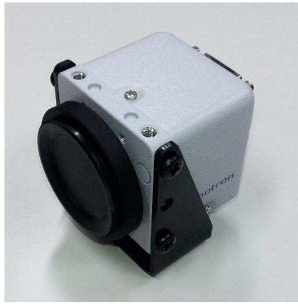

(b) Camera

(c) Projector

Figure 2-1 3D measurement system, comprised of a camera and a projector.

The working flow of the whole system is shown in Figure 2-2. In Figure 2-2, in the step 1, an initial 3D surface with texture is measured; in step 2, a deformed textured brain surface is measured; the two surfaces are registered by the proposed non-rigid registration method in step 3.

Table 1 System configuration

Camera	IDP Express R2000, Photron Inc.
Camera resolution [pixels]	512 × 512
Laser projector	SHOWWX, MICROVISION Inc.
Laser projector resolution [pixels]	848 × 480

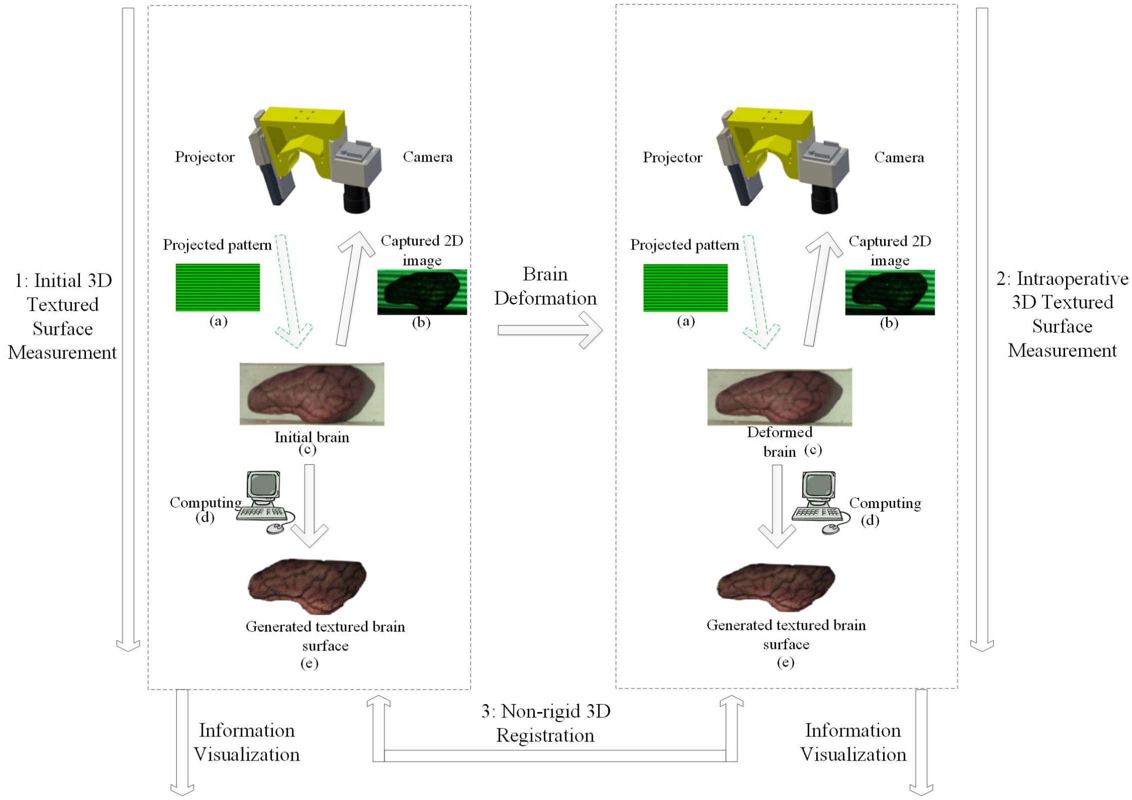

Figure 2-2 3D measurement system work flow: (a) is the projected pattern from the projector; (b) is the captured 2D image by the camera; (c) is the object; (d) is the procedure of 3D surface computing; (e) is the calculated textured brain surface

The detail of the working environment of our system is shown in Figure 2-3 with a brain phantom as the scanning object. Our system is mounted on an adjustable arm (point setter, Mitaka Kohki Co., Ltd.), where the position and the angle can be set by the pneumatically driving joint.

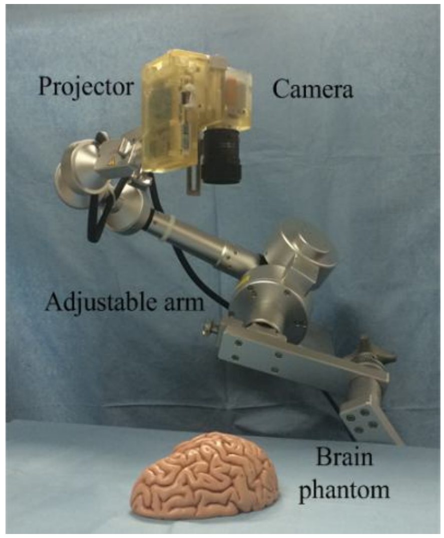

Figure 2-3 Detail of the working environment of our system. The system is comprised of a camera and a projector.

2.2 **Brain surface measurement**

As mentioned above, our system implemented phase-shift 3D shape measurement to measure brain surface. In the previous research, the Laser Range Scanner (LRS) and stereo-system have been used to measure brain surface and they can offer the textured brain surface.

2.2.1 Previous brain-surface measurement methods

In the previous research, measuring the intraoperative textured brain surface includes two kinds of system: Laser range scanner (LRS) and stereo-system. And these two kinds of technologies will be described in this section.

a. Laser range scanner (LRS)

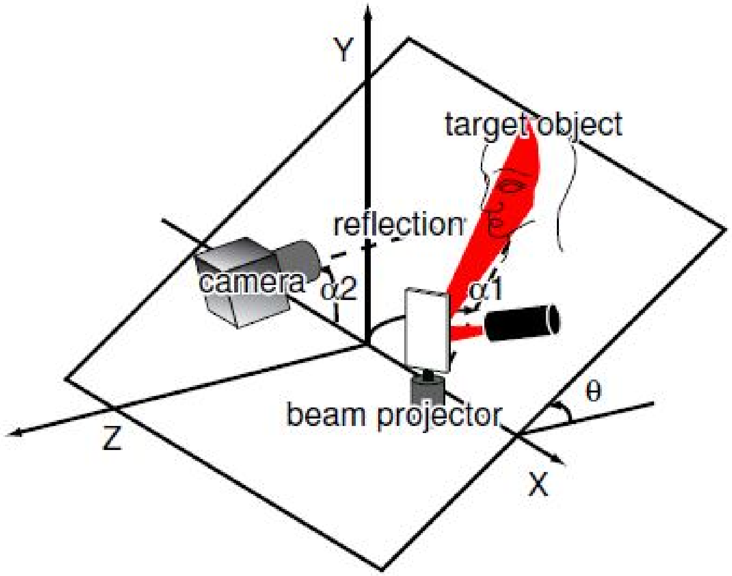

Figure 2-4 The configuration of laser range scanner[120]. The projector projects the red beam onto the target object and the camera records the reflection of the beam on the target.

The Laser Range Scanner (LRS) involved a laser-beam projector and a camera, as shown in Figure 2-4. A sheet beam is projected on the target, and then the camera gets the incident beam positions. Then the range data of the target Z can be given by:

$$Z = \frac{d \tan\alpha_1 \tan\alpha_2}{\tan\alpha_1 + \tan\alpha_2} \cos\theta \tag{2-1}$$

Where d, α_1, θ is the distance between the camera and the beam projector, the beam projection angle, the angle between the x-z plane and point on the target. And α_2 is derived from a beam position on the image sensor.

In LRS, the captured 2D texture image and the measured 3D surface is relatively separated. In order to obtain the correspondence between the 3D point and the 2D texture, a projection transformation is derived using the direct linear transformation algorithm (DLT). The DLT uses at least eight geometric fiducials $\overline{X_i} = (x_i, y_i, z_i)$ and their corresponding texture coordinates $\overline{u_i} = (u_i, v_i)$ to calculate 11 projection parameters, which can be used to map $\overline{X}$ to $\overline{u}$ as follows:

$$
\begin{aligned}
u_i - \Delta u_i &= \frac{l_1 x_i + l_2 y_i + l_3 z_i + l_4}{l_9 x_i + l_{10} y_i + l_{11} z_i + 1} \\
v_i - \Delta v_i &= \frac{l_5 x_i + l_6 y_i + l_7 z_i + l_8}{l_9 x_i + l_{10} y_i + l_{11} z_i + 1}
\end{aligned}
\tag{2-2}
$$

Figure 2-5 shows a commercial LRS which is composed of camera and laser scanning, which has been used in surgeries applications by Ding *et al.* and Cao *et al.* Figure 2-6 (a) shows the FOV of a brain surface scanning and Figure 2-6 (b) shows the generated 3D point cloud.

Figure 2-5 LRS used in Ding *et al.*'s research[110]

(a) Brain surface scanning (b) Generated brain surface

Figure 2-6 LRS application in brain surgery[110]

b. Stereo-system

Another 3D measurement system is an inactive method that has been used to measure 3D brain shape with texture by using dual cameras. After the camera calibration to estimate the intrinsic parameters, extrinsic parameters and point correspondences, the 3D shape could be obtained by triangulation. One of the 3D stereo shape measurement systems is shown in Figure 2-7. One of its 3D measurement results is shown in Figure 2-8.

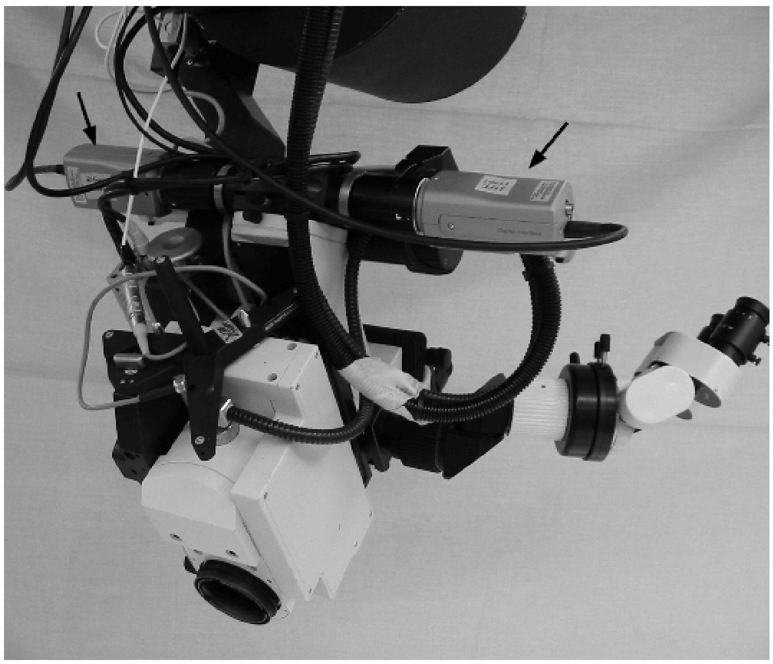

Figure 2-7 Stereo-3D brain surface measurement [6]

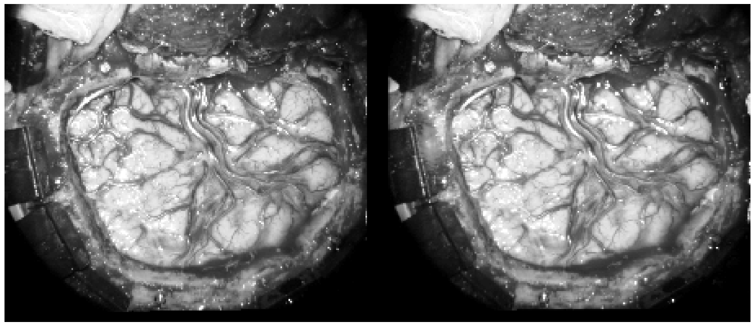

(a) Captured 2D image for 3D reconstruction

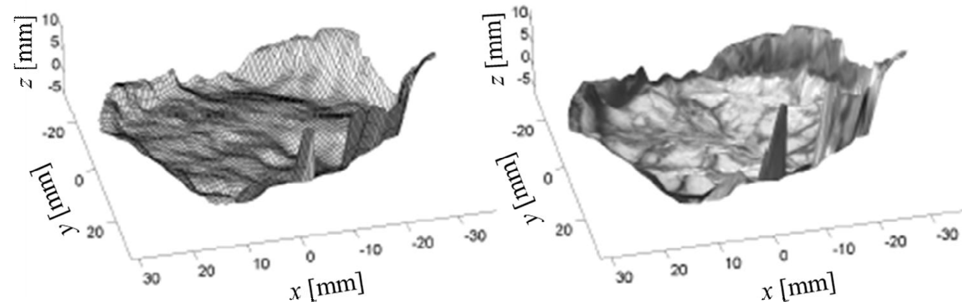

(b) Generated 3D surface

Figure 2-8 3D measurement result of stereo-camera system[6].

c. Phase-Shift 3D Measurement

In our system, we implemented a phase-shift 3D shape measurement. The resolution of points acquired by LRS is less than that of image textures, limiting tracking accuracy. Moreover, projection transformation, calculated using 11 estimated parameters, or interpolation is needed to obtain the corresponding between 3D point and 2D texture (described by equation 2-2). 3D brain surface generated by stereo-system uses only a subset of image pixels for matching, resulting in a spatially coarse surface. In contrast, the implemented phase-shift method usually generates a dense 3D textured surface by obtaining every corresponding pixel pair between camera images and projector images without interpolation and projection matrix. This method is robust to the texture intensity change which is important for brain surface measurement because the texture on brain surface contains large intensity variations. Meanwhile, phase-shift is a 3D measurement method that has been applied in different areas. Especially, it has been used into Surgery Navigation Systems[118, 119].

Figure 2-9 shows the configuration of a phase-shift system. This is a typical triangulation-based system. A computer generated sinusoidal fringe pattern is projected by a projector onto an object surface, a camera, from another viewing angle, captures the scattered fringe images by the object. The computer can compute and recover the 3D shape. Since this is a triangulation-based system, the correspondences between the projector projected image and the camera captured image must be identified.

In the phase-shift method, the correspondence between camera image pixel and projector image pixel is established in phase domain that means a pixel on the camera correspond to the point projected by the projector only if both points have the same phase value. Because the structured pattern contains vertical stripes, each phase value corresponds to a vertical line on the projected image. Once the correspondence is identified, the depth information can be recovered based on triangulation.

A set of sinusoidal patterns is projected onto the object surface. The intensities for each pixel (x,y) of the projected patterns are described as:

$$I(x,y) = I^{'}(x,y) + I^{''}(x,y)\cos(\phi(x,y) + \frac{2\pi(i-1)}{N}) \quad (2\text{-}3)$$

In the function, $I(x,y)$ is the intensity of the projected patterns and $I^{'}(x,y)$ is the offset component (background); $I^{''}(x,y)$ is the modulation signal amplitude; is the phase $\phi(x, y)$, N is the projected pattern number. Figure 2-10 (a) shows the graph profiles of the combination of the three sinuous wave patterns.

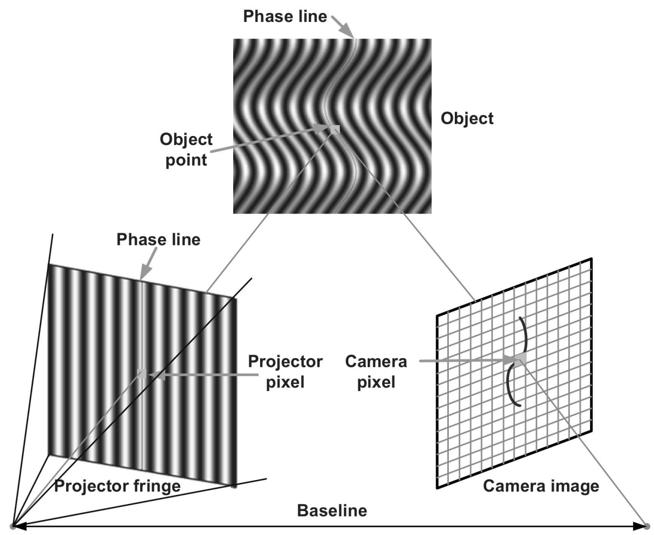

Figure 2-9 The phase-shift measurement system[121]

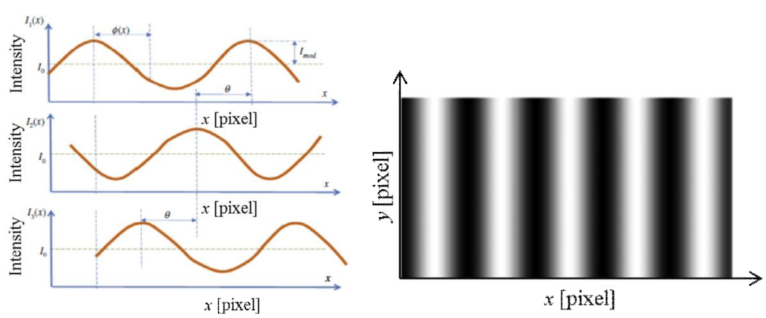

(a) Profile of the sinuous patterns (b) Example of one projected pattern

Figure 2-10 Phase-shift with three projection patterns and an example of a fringe image

Then the $\phi(x, y)$ in the function can be calculated by the function shown below:

$$\phi^{'}(x, y) = \arctan\left\{\frac{\sum_{i=1}^{N} I_i(x, y)\sin[2\pi(i-1)/N]}{\sum_{i=1}^{N} I_i(x, y)\cos[2\pi(i-1)/N]}\right\} \tag{2-4}$$

Where $I_i(x,y)$ is the intensity of the i_{th} image at pixel (x,y); N is the total projected image number.

The phase directly gives a depth-map of the projected surface, which can be converted into a distance measure from a calibration object with known geometry.

However, in the phase-shift method, the phase calculated is just the relative phase in the region $[-\pi, \pi]$ and then a phase-unwrap is required to achieve unique correspondence between phases and heights due to a 2π angular period of radians. The unwrapping procedure is illustrated in Figure 2-11 for the undistorted projected pattern (left) and the distorted pattern captured in the camera (right). The periods along the dimension of the angular phase are added to a multiple of 2π archiving a unique depth information.

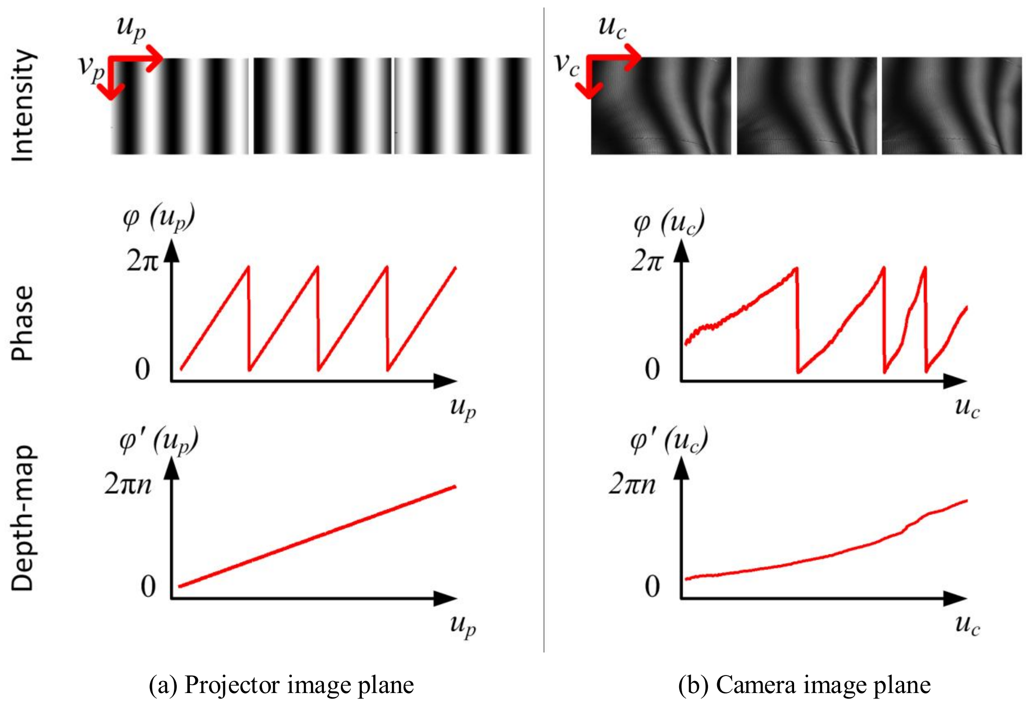

Figure 2-11 Phase unwrapping procedure

The basic idea to unwrap the phase is shown as the following function:

$$
\begin{aligned}
&\varphi_u(x_i) = \varphi_w(x_i) + m_i 2\pi \\
&m_i = \mathrm{INT}\{[\varphi_w(x_i) - \varphi_w(x_i - 1)]/2\pi + 0.5\} + m_{i-1} \\
&m_0 = 0
\end{aligned}
\tag{2-5}
$$

This kind of phase unwrapping is based on the previous pixel result. That means if one-pixel phase unwrapping result is incorrect, the error of all the pixels after this pixel will be accumulated. An example can be seen in Figure 2-12.

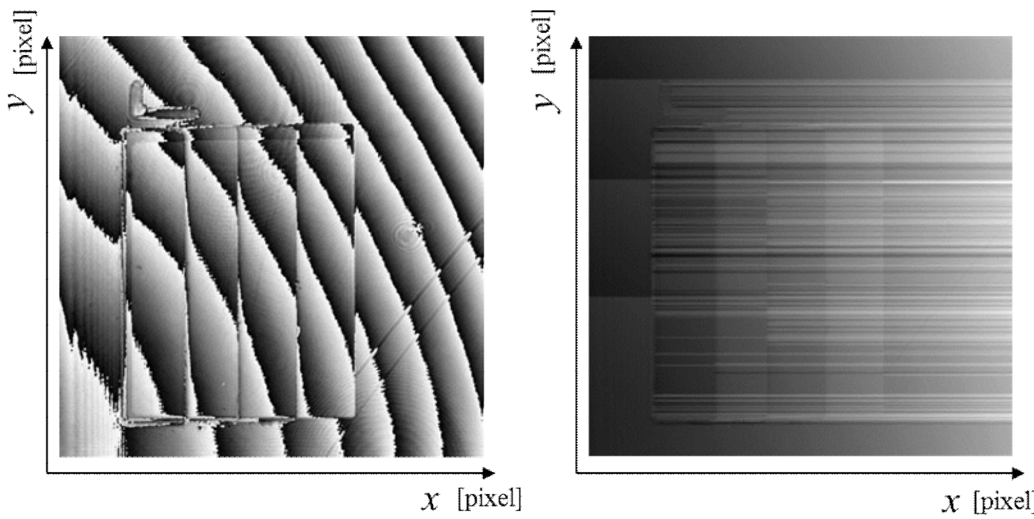

(a) Wrapped image (b) Unwrapped image

Figure 2-12 Phase unwrapping

In Figure 2-12 (a) is the wrapped phase after the calculation and (b) is the unwrapped phase. The horizontal line was an error due to an error occurred at one pixel. So some researchers proposed other methods addressing this problem, such as flood-fill[122] based, quality map quality-guided phase unwrapping algorithm, and reliability evaluation based algorithm[123].

In those methods, the quality map guided methods provide a guide to the phase unwrapping procedure. The state of art quality map calculation methods are shown below:

1) Pseudo-correlation map

The pseudo-correlation map[124] is designed to measure the correlation of the wrapped phase images. The value of the quality map for pixel (x,y) is calculated according to

$$q_{x,y} = \frac{\sqrt{(\sum \cos\psi_{i,j})^2 + \sqrt{(\sum \sin\psi_{i,j})^2}}}{k^2} \tag{2-6}$$

Where $\psi_{i,j}$ is the wrapped phase value and the sums are evaluated in the $k \times k$ neighborhood centered at each pixel(x,y). The pseudo-correlation map is based on the correlation of the wrapped phase image. It is sensitive to the noise phase data since the noise regions of wrapped phase image are normally the low correlation regions. However, the pseudo-correlation map may mark the reliable regions with steep slopes as low-quality regions.

2) Phase derivatives variance map

The phase derivative variance map[124] measures the statistical variance of the phase derivatives. The value of this map for pixel (*m,n*) is expressed as

$$q_{m,n} = \frac{\sqrt{(\sum(\Delta_{i,j}^{x} - \overline{\Delta_{m,n}^{x}}))^2} + \sqrt{(\sum(\Delta_{i,j}^{y} - \overline{\Delta_{m,n}^{y}}))^2}}{k^2} \tag{2-7}$$

Where the terms $\Delta_{i,j}^{x}$ and $\Delta_{i,j}^{y}$ are the partial derivatives of the phase, the terms $\overline{\Delta_{m,n}^{x}}$ and $\overline{\Delta_{m,n}^{y}}$ are the averages of these partial derivatives in the $k \times k$ windows, and the sums evaluated in the $k \times k$ neighborhood centered at the pixel (m, n) The phase derivatives variance map can be estimated as the local sample variance of the phase derivatives. The map indicates the badness of the phase data. In other words, the more unreliable the phase data is, the higher the phase derivatives variance is.

3) Maximum phase gradient map

The maximum phase gradient map[124] is defined as the largest phase gradient value in the $k \times k$ neighborhood of each pixel. The value of the quality map for pixel (m, n) is calculated according to

$$z_{m,n} = \max\{\max\{|\Delta_{i,j}^{x}|\}, \max\{|\Delta_{i,j}^{y}|\}\} \tag{2-8}$$

Where the terms $\Delta_{i,j}^{x}$ and $\Delta_{i,j}^{y}$ are the partial derivatives of the phase and the max are evaluated in $k \times k$ neighborhoods of the given pixel.

In our system, we implemented a phase unwrapping methods by reliability[125] which use the second differences. The use of the absolute value of the gradients in the reliability function has a number of disadvantages. If a high carrier value is present, the carrier becomes the major modulation component. However, a low carrier value would increase or decrease the values of the gradients depending on the pixel of the images, and produce an inappropriate measurement for reliability.

The calculation of second differences for pixels in an image can be find in Figure 2-13. To calculate the second differences, the pixels(i,j-1),(i,j+1)(i-1,j) and (i+1,j) is needed and is called orthogonal neighboring pixels. Where (i-1,j-1),(i+1,j-1),(i-1,j+1) and (i+1,j+1) pixels are called diagonal neighboring pixels.

$(i\text{-}1, j\text{-}1)$	$(i, j\text{-}1)$	$(i\text{+}1, j\text{-}1)$
$(i\text{-}1, j)$	(i, j)	$(i\text{+}1, j)$
$(i\text{-}1, j\text{+}1)$	$(i, j\text{+}1)$	$(i\text{+}1, j\text{+}1)$

Figure 2-13 Calculation of the second differences in an image

The second difference D of (i,j) pixel can be calculated by the equation:

$$
\begin{aligned}
&R = 1/D \\
&D(i,j) = [H^2(i,j) + V^2(i,j) + D_1^2(i,j) + D_2^2(i,j)]^{1/2} \\
&H(i,j) = \gamma[\varphi(i-1,j) - \varphi(i,j)] - \gamma[\varphi(i,j) - \varphi(i+1,j)] \\
&V(i,j) = \gamma[\varphi(i,j-1) - \varphi(i,j)] - \gamma[\varphi(i,j) - \varphi(i,j-1)] \\
&D_1(i,j) = \gamma[\varphi(i-1,j-1) - \varphi(i,j)] - \gamma[\varphi(i,j) - \varphi(i+1,j+1)] \\
&D_2(i,j) = \gamma[\varphi(i-1,j+1) - \varphi(i,j)] - \gamma[\varphi(i,j) - \varphi(i+1,j-1)]
\end{aligned} \tag{2-9}
$$

This phase unwrapping method can achieve a very good phase unwrapping result because it unwrapps the phase from the highest reliable value to the lower reliability value. But if the object is separated, the phase unwrapping algorithm will not work. However, this will not happen in the surgery brain measurement. The phase unwrapping result will be shown in the following section. The device nonlinearity or gamma distortion makes the ideal sinusoidal waveforms non-sinusoidal. In the aspect of the frequency domain, a single frequency for the ideal sinusoidal waveform becomes an infinite width of spectrum. The summation of infinite harmonic coefficients is absolutely convergent because the distorted waveform is a power signal.

After phase unwrapping, we can obtain a relative continuous phase distribution in vertical and horizontal direction. For the dot image, we know the dot point phase value and we set the value on vertical direction to be ϕ_{d_ver} and in the horizontal direction to be ϕ_{d_lat}. We can also find the dot point phase value on the phase distribution in the phase unwrapping image. We set the value on the phase unwrapping image vertical direction to be $\phi_{d\_ver}^{'}$ and in the horizontal direction to be $\phi_{d\_lat}^{'}$. Then the shift number in vertical and horizontal direction to be

$$S_{\mathrm{ver}} = \mathrm{int}(\frac{\phi_{\mathrm{d\_ver}} - \phi'_{\mathrm{d\_ver}}}{2\pi}) \tag{2-10}$$

$$S_{\mathrm{lat}} = \mathrm{int}(\frac{\phi_{\mathrm{d\_lat}} - \phi'_{\mathrm{d\_lat}}}{2\pi}) \tag{2-11}$$

Then for all the phase values in the vertical and horizontal direction, the new phase value is calculated by

$$\phi_{\mathrm{ver}}(x,y) = \phi_{\mathrm{ver}}(x,y) + 2\pi \times S_{\mathrm{ver}} \tag{2-12}$$

$$\phi_{\mathrm{lat}}(x,y) = \phi_{\mathrm{lat}}(x,y) + 2\pi \times S_{\mathrm{lat}} \tag{2-13}$$

Then the relative phase to the absolute phase-shift could be solved by the dot image projection.

After obtaining the absolute phase value on the projection image both in vertical and horizontal direction, the correspondence between the camera and projector image can be obtained by the function as shown below:

$$\begin{aligned} y' &= \frac{\phi(x,y)L_y}{2\pi} \\ x' &= \frac{\phi(x,y)L_x}{2\pi} \end{aligned} \tag{2-14}$$

In the function, (x,y) is the coordinate of captured camera pixel in the 2D image while (x', y') is the calculated correspondence coordinate in projection image. After this, the triangulation information can be used to obtain the 3D position of the object.

2.3 Information Visualization

Our system consists of a projector and a camera for 3D shape measurement. In the system, the projector has two roles. One is to project phase-shifted patterns and the other is to project images onto the brain surface. Because from the captured image, we can get the corresponding pixel of camera from projector and then we can generate a projection image for projection by the following equation:

$$\phi = \arctan\left(\frac{\sum_{i=1}^{N} I_c^i \sin(\frac{2\pi i}{N})}{\sum_{i=1}^{N} I_c^i \cos(\frac{2\pi i}{N})}\right) \tag{2-15}$$

In the equation, N is the total shifted pattern number and index i is the i_{th} image number. The vertical pixel corresponding and horizontal pixel corresponding will be described in the following sections.

2.3.1 Vertical pixel corresponding calculation

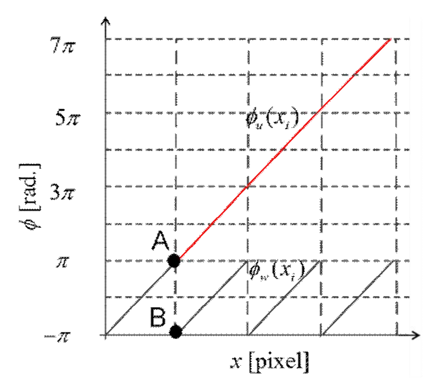

Figure 2-14 Unwrapped phase in x-axis

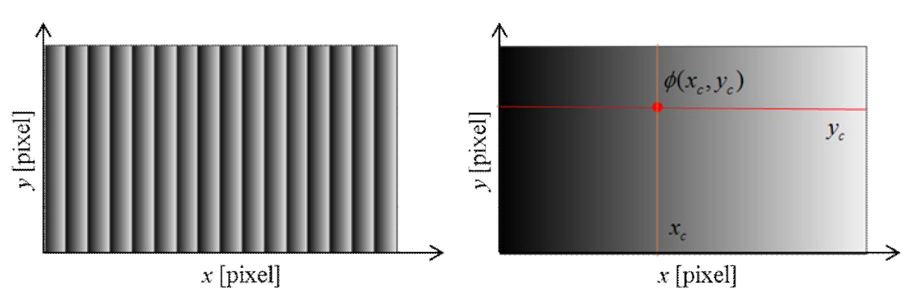

(a) Wrapped phase (b) Unwrapped phase

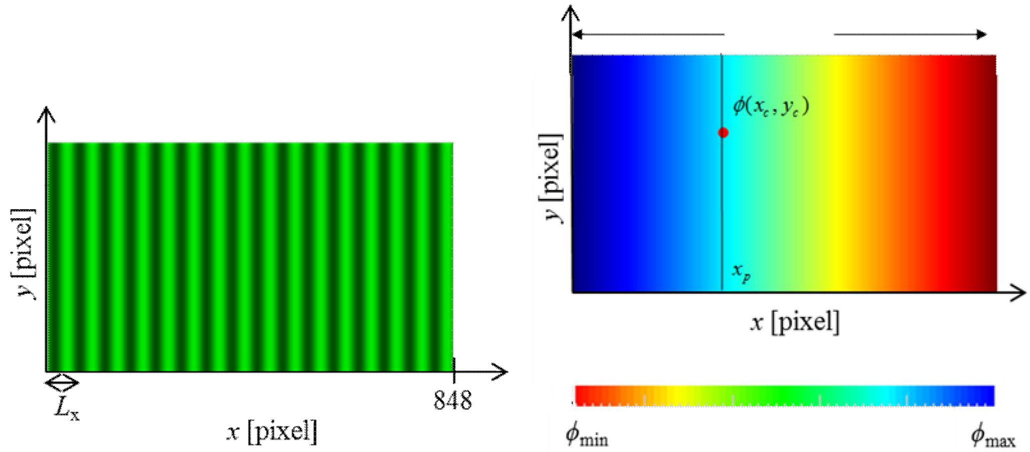

(c) Vertical original projection phase (d) Vertical original continuous phase

Figure 2-15 Vertical phase calculation

Figure 2-14 showed the phase unwrapped distribution in the x-axis direction by simulation. In Figure 2-15, (a) is the calculated wrapped phase, and (b) is the unwrapped phase after phase unwrapping. (c) is the original vertical projection image with 848 total pixel number in the x-direction and Lx is the wave length. (d) is the phase distribution in the x direction. By using the following equation, we can get the vertical x pixel corresponding of camera and projector.

$$\begin{aligned} &\phi_u(x_i) = \phi_w(x_i) + \mathrm{m}_i 2\pi \\ &\mathrm{m}_i = \lfloor |\phi_w(x_i) - \phi_w(x_{i-1})| / 2\pi + 0.5 \rfloor + \mathrm{m}_{i-1} \\ &\mathrm{m}_0 = 0 \end{aligned} \quad (2\text{-}16)$$

$$x_p = L_x \frac{\phi(x_c, y_c)}{2\pi}$$

2.4.2 Horizontal corresponding pixel calculation

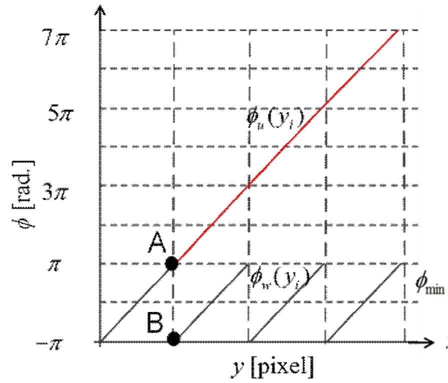

Figure 2-16 Unwrapped phase in y direction

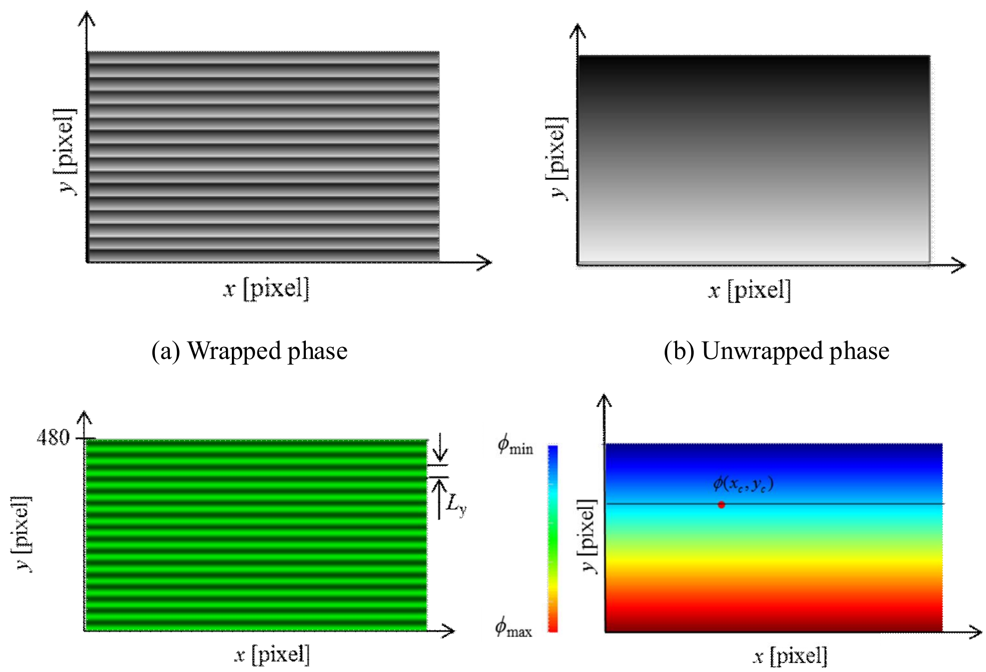

(a) Wrapped phase (b) Unwrapped phase

(c) Horizontal original projection phase (d) Horizontal original continuous phase

Figure 2-17 Vertical phase calculation

$$\begin{aligned} &\phi_v(x_i) = \phi_w(y_i) + \mathrm{m}_i 2\pi \\ &\mathrm{m}_i = \lfloor |\phi_w(y_i) - \phi_w(y_{i-1})| / 2\pi + 0.5 \rfloor + \mathrm{m}_{i-1} \\ &\mathrm{m}_0 = 0 \end{aligned} \tag{2-17}$$

$$y_p = L_y \frac{\phi(x_c, y_c)}{2\pi}$$

Figure 2-16 showed the phase unwrapped distribution in the *y*-axis direction by simulations. In Figure 2-17, (a) is the calculated wrapped phase and (b) is the unwrapped phase after phase unwrapping. (c) is the original horizontal projection image with 480 total pixel number in the y direction and *Ly* is the wave length. (d) is the phase distribution in *y* direction. By using the following equation, we can get the vertical *y* pixel corresponding of camera and projector.

2.3.3 Example of projection image

In this section, some projection examples will be demonstrated.

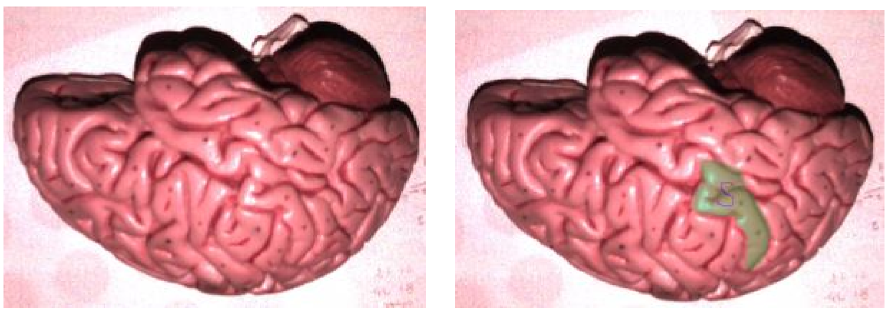

(a) Original 2D image (b) 2D image with labeled color

Figure 2-18 2D brain phantom image

As shown in Figure 2-18, (a) is the original brain image and (b) is the brain function labeled image. In Figure 2-18 (b), the transparent green color is labeled to represent the area for language function. The “S” means “speaking”.

After labeling on the original image with brain function mapping color, our system can project this function mapping onto the brain surface by scanning the brain surface and finding the correspondence between the camera image and projection image. In Figure 2-19, it is the calculated projection image with labelling color for projection. In Figure 2-20, the projected image captured by camera onto the brain phantom is shown. It can be seen that the transparent green color represents the language function area and when surgeon performs the surgery, this labeled area should be avoided in the brain surgery. The surgeon can directly see the brain labeled color brain mapping information without any other monitor. And also because the labeled color is transparent, it will not disturb the vision of surgeon and the procedure of the surgery. This is just an example of the language function brain mapping. In fact, more functions such as motion, sensor function can be projected onto the brain surface with different transparent color labeling.

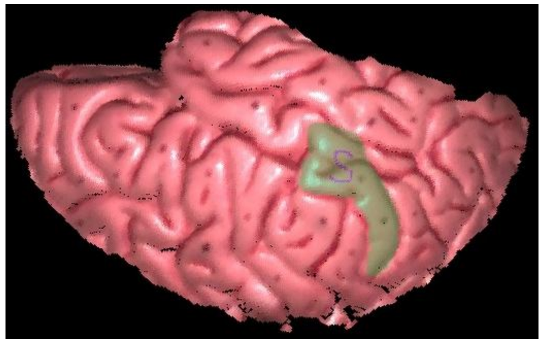

Figure 2-19 Calculated projection image

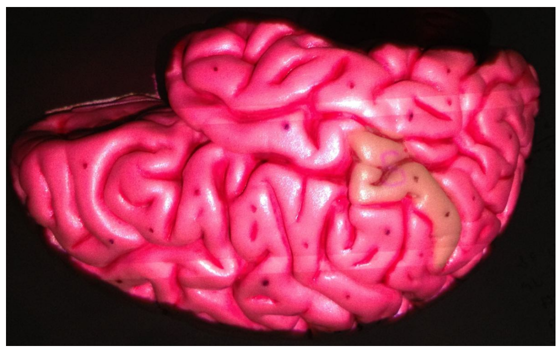

Figure 2-20 Camera captured projected image

A projection application on the porcine brain surface is shown in Figure 2-21 with some projection target points.

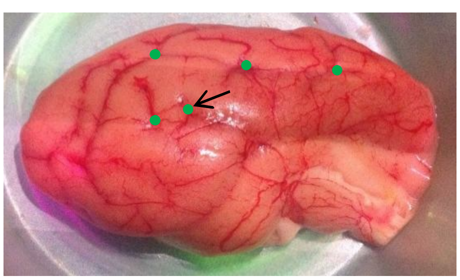

(a) Target point of pig brain

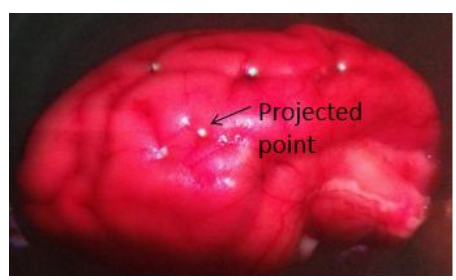

(b) Projection result

Figure 2-21 Projection on porcine brain

2.4 System calibration

Camera calibration, which is crucial in realizing high accuracy of 3D shape measurement, was addressed and will be introduced in this section. The camera is modeled as pinhole model for the camera calibration; the projector is also considered as a camera by using phase-shift projection technology; and then the camera-projector calibration system was calibrated by using normal stereo-system calibration. As the projector has gamma effect, gamma correction is implemented to reduce the gamma effect.

a) Camera calibration

The camera is modeled as pin model in the calibration system and before determining the 2D image coordinates of a specified point by the 3D point position in a world coordinate system, some transformations and projections need to be performed, as shown in Figure 2-22:

1. A rigid transformation from world coordinates (X, Y, Z) to camera coordinates (X_c, Y_c, Z_c)
2. Perspective projection from camera coordinates (X_c, Y_c, Z_c) to undistorted sensor coordinates (x,y)
3. Adjustment of undistorted sensor coordinates (x,y) to distorted sensor coordinates (x_d, y_d)
4. Unit conversion (mm to the pixel) of distorted sensor coordinates (x_d, y_d) to image coordinates (x_f, y_f).

The detail of each of coordinate systems is described below:

The transformation from world coordinates to camera coordinates in homogeneous coordinates is

$$\begin{pmatrix} X_c \\ Y_c \\ Z_c \\ 1 \end{pmatrix} = \begin{pmatrix} R & T \\ 0 & 1 \end{pmatrix} \begin{pmatrix} X \\ Y \\ Z \\ 1 \end{pmatrix} \tag{2-18}$$

Where R is the rotation matrix and T is the translation matrix.

Undistorted sensor coordinates (x,y) can be computed from camera coordinates (X_c, Y_c, Z_c) by the following equations:

$$\begin{aligned} x &= f\frac{X_c}{Z_c} \\ y &= f\frac{Y_c}{Z_c} \end{aligned} \tag{2-19}$$

Where f is the camera focal length. Then we can see that by using the pinhole camera model, a world coordinates could be projected back to the image plane coordinates by

$$\begin{pmatrix} x_s \\ y_s \\ s \end{pmatrix} = P \begin{pmatrix} X \\ Y \\ Z \end{pmatrix} \qquad (2\text{-}20)$$

Where P is a parameter that can be described by R T and f.

After that, the conversion of distorted sensor coordinates to image coordinates can be described by the following equation:

$$x_f = S_x \frac{N_{fx}}{N_{cx} d_x} x_d + C_x \qquad (2\text{-}21)$$
$$y_f = \frac{1}{d_y} x_d + C_y$$

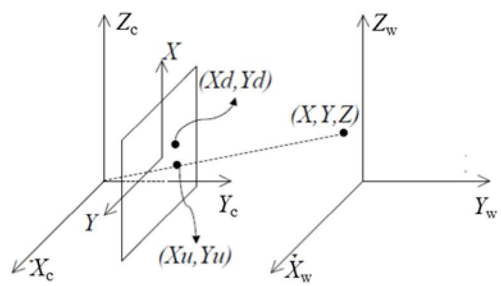

Figure 2-22 Camera model: perspective projection and lens distortion

For the camera distortion, the mathematical description of the commonly used distortion model is described by the equation:

$$\begin{aligned} x_d &= x - x_d(\kappa_1 r^2 + \kappa_2 r^4 + \ldots + \kappa_n r^{2n}) \\ y_d &= x - y_d(\kappa_1 r^2 + \kappa_2 r^4 + \ldots + \kappa_n r^{2n}) \\ r &= \sqrt{x_d^2 + y_d^2} \end{aligned} \qquad (2\text{-}22)$$

Where (x,y) is the undistorted sensor coordinates and (x_d, y_d) is the distorted sensor coordinates. $(\kappa_1, \kappa_2, \ldots \kappa_n)$ are the lens distortion parameters. The conversion from the distorted sensor coordinates (x_d, y_d) to image coordinates (x_f, y_f) is described below:

$$\begin{aligned} x_f &= S_x \frac{N_{fx}}{N_{cx} d_x} x_d + C_x \\ y_f &= \frac{1}{d_x} x_d + C_y \end{aligned} \qquad (2\text{-}23)$$

Where N_{fx} is the number of pixels in a line sampled by the user; N_{cx} is the number of camera elements in X direction; d_x and d_y are the center distances between adjacent camera elements in X and Y direction, respectively; S_x is the scale factor and (C_x, C_y) is the image center.

We have described how the world object could be projected to image coordinates by perspective projection and a radial lens distortion model. The extrinsic and intrinsic camera parameters need to be calibrated to perform a projection. There are total 11 parameters among all the parameter and then 11 equations are needed to obtain the 11 parameters. Then the transformation from world coordinates to image coordinates could be described as:

$$\begin{pmatrix} x_s \\ y_s \\ s \end{pmatrix} = \underbrace{\begin{pmatrix} \alpha_x & 0 & C_x & 0 \\ 0 & \alpha_y & C_y & 0 \\ 0 & 0 & 1 & 0 \end{pmatrix}}_{\text{A}} \underbrace{\begin{pmatrix} r_1 & r_2 & r_3 & t_x \\ r_4 & r_5 & r_6 & t_y \\ r_7 & r_8 & r_9 & tz \\ 0 & 0 & 0 & 1 \end{pmatrix}}_{B} \begin{pmatrix} X \\ Y \\ Z \\ 1 \end{pmatrix} \qquad (2\text{-}24)$$

In that equation, matrix B is the rigid transformation matrix and A includes the projection from camera to sensor coordinates, the transformation from the sensor to image coordinates. As noted, 11 equations are needed to calculate the extrinsic and intrinsic camera meters, and it could be expressed as the following equation:

$$\begin{pmatrix} x_{s1} & x_{s2} & \cdots & x_{sn} \\ y_{s1} & y_{s2} & \cdots & y_{sn} \\ s_1 & s_2 & \ldots & s_n \end{pmatrix} = \begin{pmatrix} \alpha_x & 0 & C_x & 0 \\ 0 & \alpha_y & C_y & 0 \\ 0 & 0 & 1 & 0 \end{pmatrix} \begin{pmatrix} r_1 & r_2 & r_3 & t_x \\ r_4 & r_5 & r_6 & t_y \\ r_7 & r_8 & r_9 & tz \\ 0 & 0 & 0 & 1 \end{pmatrix} \begin{pmatrix} X_1 & X_2 & \ldots & X_n \\ Y_1 & Y_2 & \ldots & Y_n \\ Z_1 & Z_2 & \ldots & Z_n \\ 1 & 1 & \ldots & 1 \end{pmatrix} \qquad (2\text{-}25)$$

Where, (X_i, Y_i, Z_i) is the world coordinate and (x_i, y_i) is the image coordinate. Other parameters have been described before.

b) Projector calibration

The projector is a kind of device for display and in our system, the projector calibration followed the method proposed by Song Zhang[126] who considered the projector as the inverse-camera through phase-shift technology. The flat plane used with 8×6 green filled circle before and after projector projected are shown in Figure 2-23 and Figure 2-24.

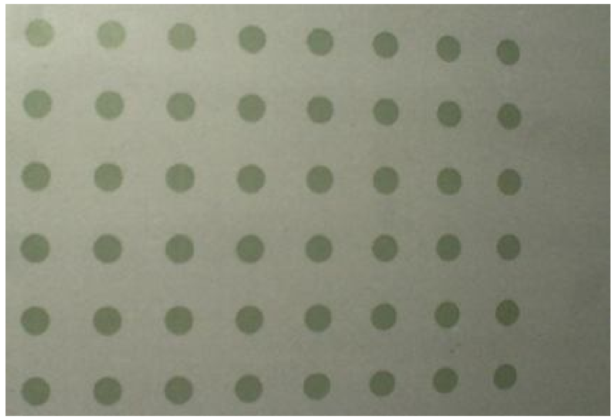

Figure 2-23 Camera captured image

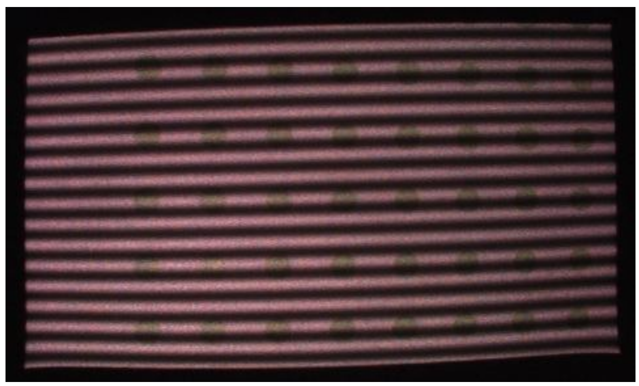

Figure 2-24 Camera captured projected image

The detected circle center position in the camera image could be easily transferred to the corresponding position in the projector image plane by equation 2-16 and 2-17 for x-axis and y-axis, respectively. Then after changing 15 different positions and directions, the equation 2-23 could be used to estimate the projector parameter.

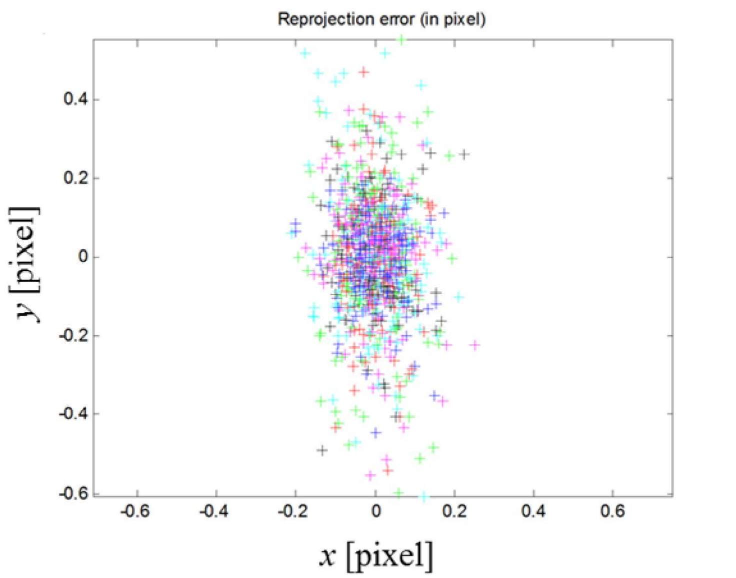

Figure 2-25 Projector calibration re-projection error

The re-projection error of the projector calibration is shown in Figure 2-25 and it shows very small projection error. The extrinsic parameters of the calibration are shown in Figure 2-26. From the results it shows that the 19 different calibration image plans are listed from different direction and position. One of the re-projected image error is shown in Figure 2-27. The error direction and magnitude is described. The estimated projector distortion model is shown in Figure 2-28.

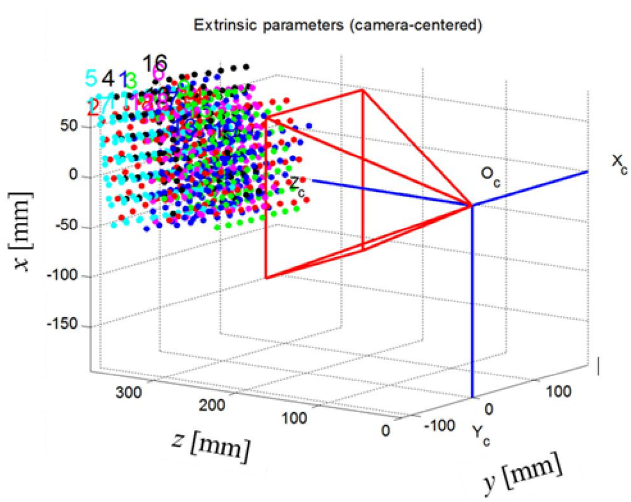

Figure 2-26 Projector calibration extrinsic parameters

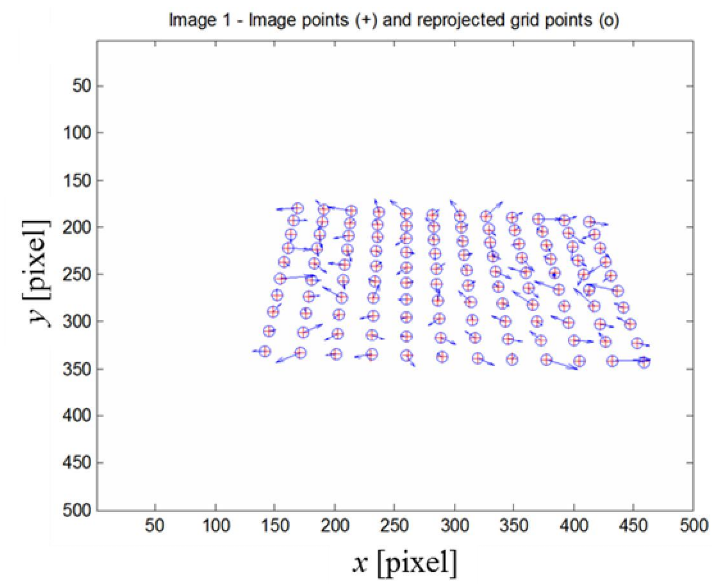

Figure 2-27 Projected points and target points

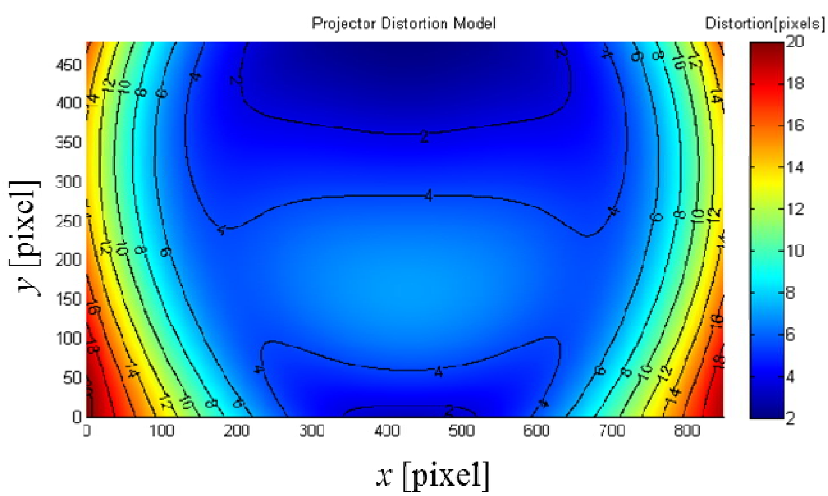

Figure 2-28 Calculated projector distortion model

C) Gamma calibration

The gamma effect of the projector makes the output of the projector signal not an ideal sinusoidal wave form with a power gamma, as shown in Figure 2-29.

$$I^{c} = (I^{p})^{\gamma} \tag{2-26}$$

We apply a Fourier transformation to the curve of the projector image and we can find the second order harmonics of the projection sin-curve, as shown in Figure 2-30. However, an ideal sinusoidal wave form should not have this. So, it is very important for us to do the gamma correction.

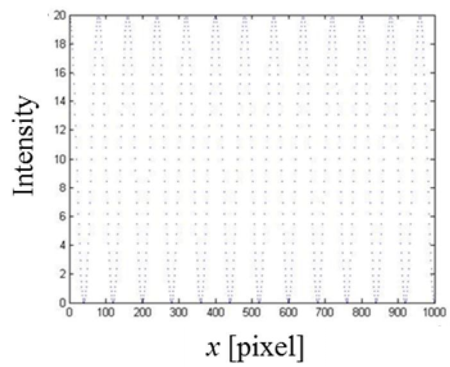

Gamma = 1

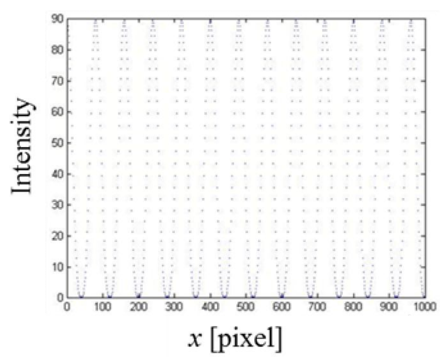

Gamma = 1.5

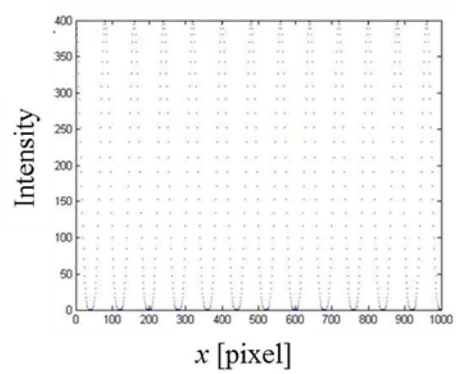

Gamma = 2

Figure 2-29 Gamma effect of the projector

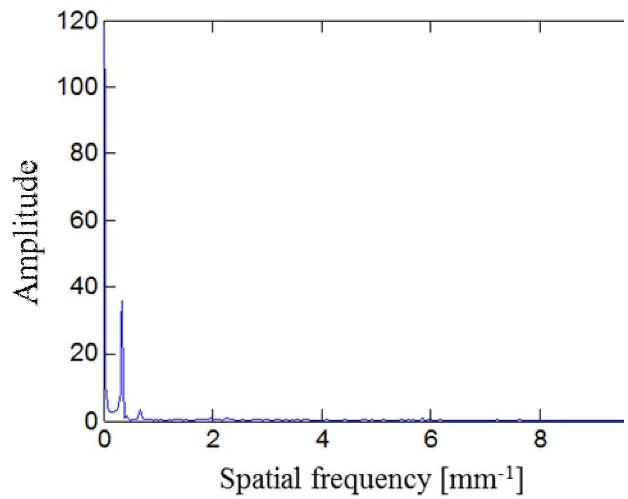

Figure 2-30 Fourier transformation of the projector image

The result of scanning a plane before gamma correction is shown in Figure 2-31 . A sin/cos shape wave is observed in both the vertical and horizontal direction of the plane.

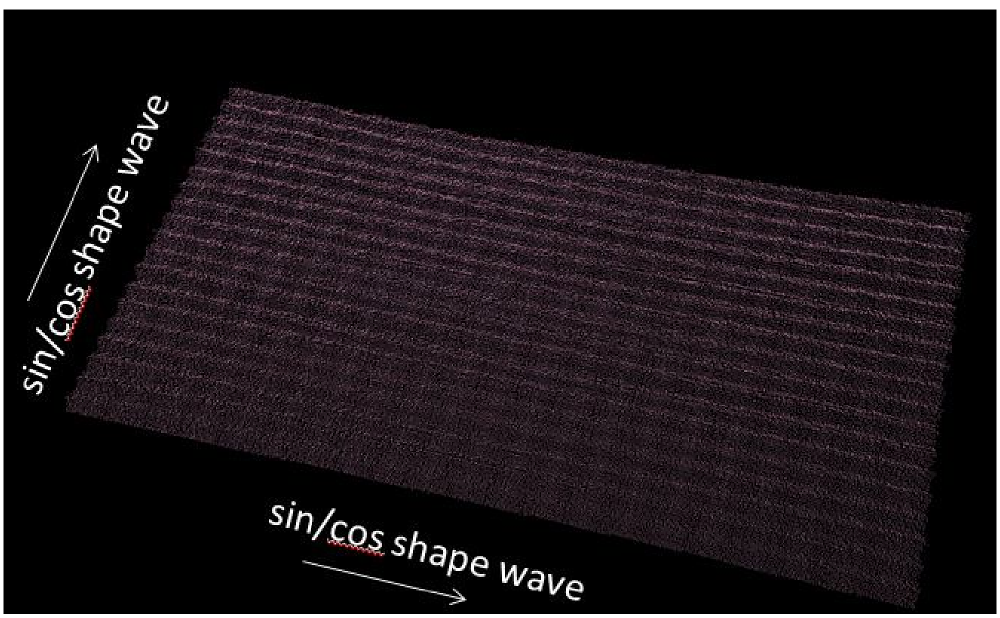

Figure 2-31 The flat plane before gamma correction

A pixel of the projected pattern can be expressed as

$$I_n^{\mathrm{p}} = \alpha^{\mathrm{p}}(0.5 + 0.5\cos(\phi - \frac{2\pi n}{N})) \tag{2-27}$$

Where α^{p} is a modulation constant controlling the intensity range of a sine wave. In the camera image, the captured image distorted by gamma is described as

$$I_n^{c} = \alpha^{c}(0.5 + 0.5\cos(\phi - \frac{2\pi n}{N}))^{\gamma} \tag{2-28}$$

Where I_n^{c} is the intensity of a pixel, $\alpha \in [0,1]$ is the reflectivity of a scanned object, γ is the combined gamma value for the projector-camera pair ($\gamma \geq 1$).

Apply the binomial series

$$(1+x)^{t} = \sum_{m=0}^{\infty}\left[\binom{t}{m}x^{m}\right] \tag{2-29}$$

Then I_n^{c} could be calculated as

$$I_n^{c} = 0.5^{\gamma}\alpha\alpha_{p}\sum\nolimits_{m=0}^{\infty}\left[\binom{\gamma}{m}\cos^{m}(\phi - \frac{2\pi n}{N})\right] \tag{2-30}$$

Then we can have

$$I_n^{c} = A + \sum_{k=1}^{\infty}\left\{B_k \cos\left[k\left(\phi - \frac{2\pi n}{N}\right)\right]\right\} \tag{2-31}$$

Where

$$A = 0.5B_0 \tag{2-32}$$

$$B_k = 0.5^{\gamma-1}\alpha\alpha_{p}\sum\nolimits_{m=0}^{\infty} b_{k,m} \tag{2-33}$$

With

$$b_{k,m} = 0.5^{2m+k}\binom{\gamma}{2m+k}\binom{2m+k}{\gamma} \tag{2-34}$$

Then we can have

$$(\gamma - k)b_{k,m} - 2(k+1)b_{k+1,m} = 2mb_{k,m} + 2mb_{k+1,m} \tag{2-35}$$

If summing the left- and right- hand side of the function, we can obtain

$$\frac{B_{k+1}}{B_k} = \frac{\gamma - k}{\gamma + k + 1} \tag{2-36}$$

This is the function we used to find the similar γ of the projector. And

$$B_k \approx \frac{2}{N}\left\{\left[\sum_{n=0}^{N-1} I_n^c \sin(m\frac{2\pi n}{N})\right]^2 + \left[\sum_{n=0}^{N-1} I_n^c \cos(m\frac{2\pi n}{N})\right]^2\right\}^{0.5} \quad (2\text{-}37)$$

In our gamma correction procedure, we use the function shown below to calculate the gamma.

$$\frac{B_2}{B_1} = \frac{\gamma - 1}{\gamma + 2} \quad (2\text{-}38)$$

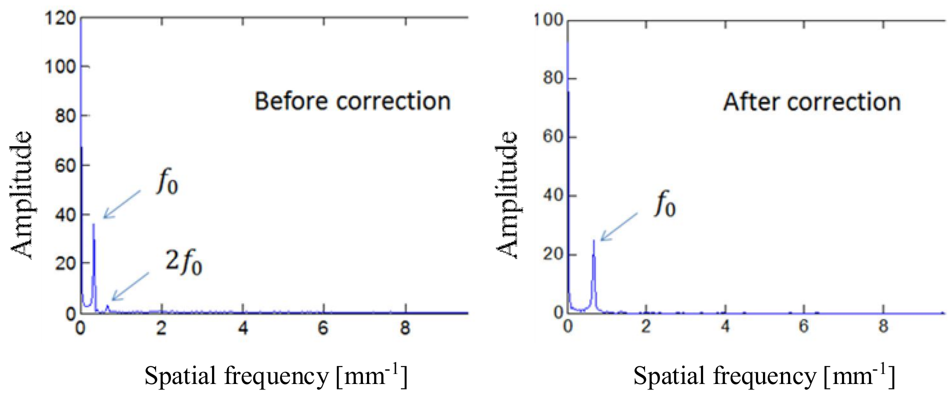

Figure 2-32 Fourier analysis for the projection waveform of before and after correction

The Fourier analysis of the waveform before and after the gamma correction is shown in Figure 2-32 and it can see that the $2f_0$ is suppressed.

The 3D reconstruction of a flat panel of before gamma correction and after gamma correction is shown in Figure 2-33. It is clear that after the gamma correction, the sin/cos waveform has been suppressed.

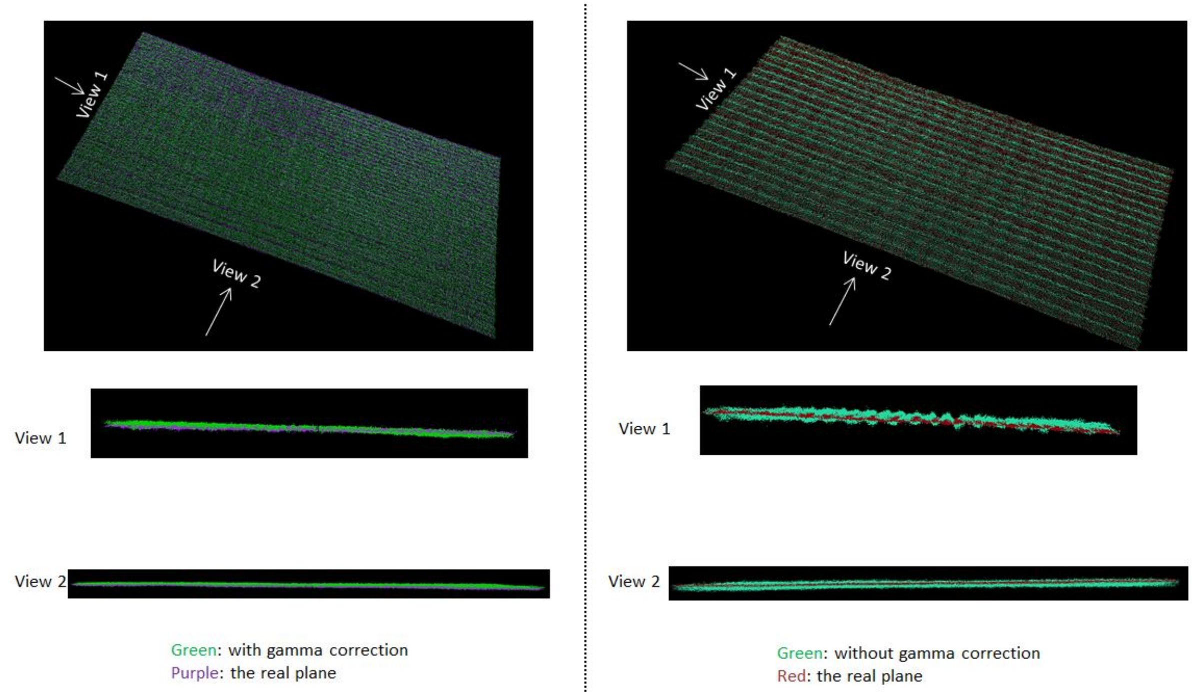

(a) After correction

(b) Before correction

Figure 2-33 Flat panel reconstruction result

3 Non-rigid Registration Method

In this chapter, the proposed non-rigid registration method, integrating texture and shape, and the implemented 3D shape measurement are introduced. Chapter 3 is comprised of non-rigid registration method overview, texture extraction, corresponding-point estimation, and spatial interpolation for deformation constraint, optimization.

3.1 Non-rigid registration method overview

3.1.1 Related previous studies

Registration is a technology to transform 2D or 3D datasets into the same coordinate system so as to align overlapping components of these sets. Registration can be divided into rigid and non-rigid registration. The rigid registration assumes that the surface is transformed by a rigid transformation matrix while the later allows deformation (*e.g.* morphing, articulation) between images or surfaces.

The impetus of our research is tracking the brain surface deformation in different surgery stages using non-rigid registration to offer sparse data for MUIGS. In the previous methods, Sun *et al.* proposed to implement Iterative Closest Point (ICP)[94], a rigid registration method, to align brain surface during brain surgery. The ICP registration method assumes that the brain did not deform largely in the surgery. However, if the brain has large deformation, the ICP method would fail in such kind of situation because large deformation usually happened in brain surgery. Also, the ICP method only considered the surface information, which will easily cause the sliding error along the surface, as suggested in Figure 1-17. In Figure 1-17, (a) is an example of the source with line/curve texture on it; (b) is the target surface with the same texture on it; (c) is one of the registration results. As suggested in (c), even the surface can achieve good alignment while the texture remains as sliding error on the surface. Accordingly, 3D surface registration integrating texture is necessary to overcome the problem of surface only registration method.

Perrine *et al.* proposed a non-rigid registration method for registering 3D brain surfaces using video sequences by minimizing an energy function including geometry, intensity, and landmark costs[117]. Their results showed an improvement in registration accuracy relative to ICP. However, their approach requires that video streams be continuously acquired to identify and track landmarks, incurring additional image processing during sudden appearance/ disappearance of elements, such as blood or surgical tools. Furthermore, their energy function did not contain any constraint for surface deformation, which could cause disordered shape deformation. Thus to solve this problem, a brain shift estimation method using optical flow has been proposed[90]. The calculated brain shift magnitude was reported to agree with the tracked probe data. However, a disadvantage lies in that if the intensity changes, the algorithm fails to track brain images. This disadvantage can be avoided by using the Normalized Cross Correlation (NCC) based on feature point tracking method proposed by Faria *et al.* [113]. However, this method is based on the assumption that the motion of the feature between frames is limited, and it fails when significant deformations occur.

Besides the intensity-texture, vessels or sulci, which are the most readily visible structures on the brain surface, have been used for brain surface registration. Marreiros *et al.* proposed a non-rigid deformation pipeline for compensating superficial brain shift using superficial blood vessels as landmarks[116]. They used the coherent point drift (CPD) to determine the correlation between intraoperative vessels and preoperative vessels from magnetic resonance angiography and then used TPS to generate volume deformation. However, their method also failed to compensate for deformation in areas where blood vessels were not present. Cao *et al.* also proposed a non-rigid registration method using 3D vessel information registration by robust point matching (RPM) to find the corresponding points[96]. Similar to Marreiros's method, TPS was implemented to generate a global deformation calculated by 3D vessels corresponding between two shapes. The influence of surrounding materials could be decreased by integrating vessel structures; however, large errors similarly occurred in points far away from the texture because displacement calculated by the TPS with the 3D vessels could be arbitrary around those points.

Thus, to overcome the disadvantage of previous related methods (sliding error[6], large error occurred far away from texture[90, 96, 101], the assumptions on some special conditions (intensity keeps constant[90] or feature keeps similar in frames[113])), a 3D non-rigid registration method which combines *shape* and *texture*, robust to texture-feature numbers change and extend of deformation, was proposed. The overview of the proposed method will be described in the next section.

3.1.2 Overview of proposed method

In this thesis, a surface and texture integrating non-rigid registration algorithm was proposed to track brain surface. Similar to Cao *et al.*'s research (TPS based[96]), by integrating vessel texture, the sliding error can be reduced. The results of previous methods showed that in TPS based registration methods, large errors occurred at points far away from the vessels because displacement calculated by the TPS with the 3D vessels could be arbitrary around those points. We believe that this is a common problem with the TPS method, because TPS is an interpolation method, which highly depends on the control point feature (control point number and position). However, we offer a distinct and effective approach to integrating vessels for surface registration compared with Cao *et al.*'s method. The differences lie in: firstly, all the points are involved into registration while Cao *et al.* only use vessels for registration; secondly, we introduced a smoothness and rigidness constraints for surface deformation instead of TPS.

Moreover, the proposed method is presented by a new energy cost function. Normally, the difficulty in non-rigid surface registration lies in determining the corresponding points and in deforming the shape. The difficulty in determining corresponding points and deforming the shape could be solved using the proposed new energy cost function, which is a weighted combination of geometric information, 3D texture matching, deformation smoothness constraint, and rigidness constraint. The first two elements help in estimating the corresponding points while the last two elements help in shape deformation. The novel point of this method lies in the combination of texture and surface registration with smoothness and rigid constraint for brain surface deformation, as well as the proposed new energy function.

The flow chart of the proposed non-rigid registration algorithm is shown in Figure 3-1. At time t_i, a textured brain surface was acquired through our phase-shift 3D shape measurement (explained in 2.2). Subsequently, the 3D texture was extracted from a 2D image using a Frangi filter (described in 3.2). At time t_j, a new 2D texture image and surface were acquired by repeating the same measurement procedure applied at time t_i. Here, the surfaces acquired at time t_i and t_j are named source surface and target surface, respectively. The source and target surfaces were matched using the proposed registration method (described in 3.3 and 3.4).

In the proposed method, space deformation is defined by a group of affine transformations in R^3. **A** is the affine transformation matrix and t is the translation vector, shown in Figure 3-2. These transformation matrices indicate the degrees of freedom in our optimization, i.e., 12 degrees of freedom per point to define an affine transformation. Undirected edges connect each point to indicate local dependencies and influences. In Equation 3-1, the x_k^0 refers to the

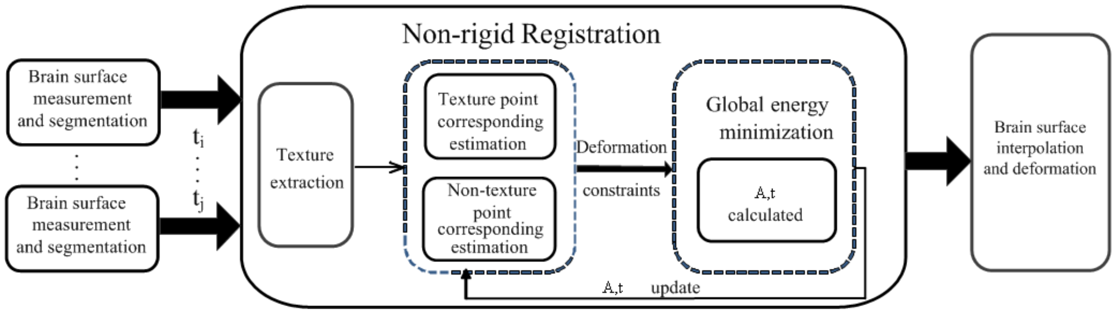

Figure 3-1 Registration work-flow

position of every point before deformation and point x_k^0 is transformed to new position $x_k(t)$ after applying translation $\mathbf{A}_k$, $\mathbf{t}_k$, :

$$x_k(t) = \mathbf{A}_k x_k^0 + \mathbf{t}_k \tag{3-1}$$

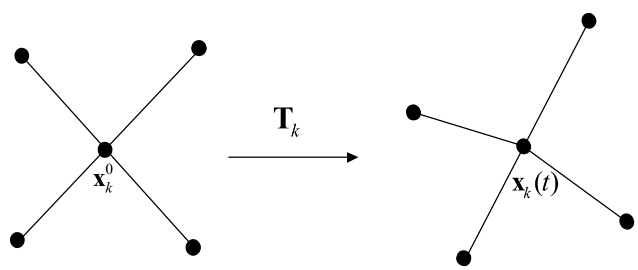

Figure 3-2 Affine transformation

Then the strategy of registration of the two shapes is to calculate transformation matrix **A** and translation vector **t** for every point of the surface by minimizing an energy function as shown below:

$$E(\mathbf{A},\mathbf{t}) = E_{\text{cor\_surface}}(\mathbf{A},\mathbf{t}) + \alpha E_{\text{cor\_texture}}(\mathbf{A},\mathbf{t}) + \beta E_{\text{smooth}}(\mathbf{A},\mathbf{t}) + \gamma E_{\text{rigid}}(\mathbf{A},\mathbf{t}) \tag{3-2}$$

In equation 3-2 $E_{\text{cor\_surface}}$ constraint is mainly used to reduce the error in surface matching. (We call it the vertical residue error). It is the residue distance from a point on a surface to the closest point on the other surface and it gets perpendicular to the latter surface. $E_{cor\_texture}$ constraint reduces the residue error in texture matching. The error component that is reduced by $E_{cor\_texture}$ in addition to $E_{cor\_surface}$ is residue in texture mismatch. It is mainly occurred along the surface and called horizontal residue by us. E_{smooth} constraint describes spatial smoothness among the matrix set corresponding two points being on each of the base and the floating surfaces. Brain surface misses texture at white matter without vessels. In such area, $E_{cor\_texture}$ does not work and instability of $E_{cor\_surface}$ point-pair matching often occurs, which is called as aperture problem. E_{smooth} interpolates and reduce the spatial matching instability. E_{rigid} is additional constraint to describe appropreatenss on rigidity of brain deformation. It is orthonormality of each matrix corresponding two points on the two surfaces.

By minimizing the equation 3-2, the affine transformation matrix of every point could be estimated. In following paragraphs, the source means the surface before deformation and the target means the surface after deformation. The detail of every energy function part will be described below.

Table 2 Role of each component of energy function

	$E_{cor\_surface}$	$E_{cor\_texture}$	E_{smooth}	E_{rigid}
Reducing vertical residue	✓	✓	N/A	N/A
Reducing horizontal residue	N/A	✓	N/A	N/A
Removing instability in spatial interpolation	✓	N/A	✓	N/A
Reducing shrinkage or expansion	N/A	N/A	N/A	✓

3.2 Texture extraction

Vessels, as texture, have been used in the registration of brain surface in either 2D images or 3D surfaces. The Frangi filter has been used for segmenting vessels in previous studies.

Marreiros *et al.* used the Frangi filter to extract brain surface vessels from infrared images. Ding *et al.* proposed a semi-automatic method for segmenting brain surface vessels to register brain images and they further extended their method to an automatic one. Their results showed that the Frangi Filter was applicable to animal brains and clinical situations in segmenting tube-like structures. Therefore, we implemented the Frangi Filter to segment brain surface vessels.

Frangi filter considers the Eigen value of local hessian matrix, as shown in Equation 3-3

$$\mathbf{H} = \begin{bmatrix} I_{xx} & I_{xy} \\ I_{yx} & I_{yy} \end{bmatrix} \tag{3-3}$$

$$\mathbf{H}\mu = \lambda\mu$$

Where I_{ij} is the second spatial derivative of the image in the i and j direction; μ is the Eigen vector and λ is the Eigen value.

Assuming $|\lambda_1| \leq |\lambda_2| \leq |\lambda_3|$ the relation shape between the Eigen value λ_i in plate-like, tube-like and sphere-like shape is shown in Figure 3-3. From the Figure 3-3, it showed that the λ_3 has the largest Eigen value because in the μ_3 direction, the second deviation has the largest value while in the other direction, the Eigen value is much smaller. For a sphere-like structure (spot in 2D), because in the 3D Eigen vector direction the second deviation is almost same, the Eigen values are almost same. In the tube-like (vessel in 2D) structure, along with the tube direction, the second deviation is smaller and the Eigen value is smaller than the other direction. This is the Eigen value feature of local hessian matrix.

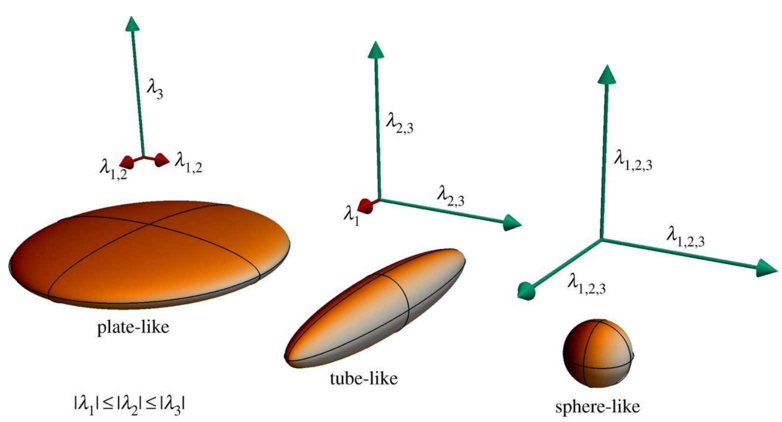

Figure 3-3 Eigen value description

Based on the Eigen value feature, Frangi *et al.* proposed a filter (described in equation 3-4) to enhance the line structure. In 2D case, the filter can be described as:

$$V = \begin{cases} 0 & \text{if } \lambda_1 < 0 \\ \exp(-\frac{R_B^2}{2\beta^2})(1-\exp(-\frac{S^2}{2c^2})) & \end{cases} \quad R_B = \frac{|\lambda_2|}{|\lambda_1|} \quad S = \sqrt{\lambda_1^2 + \lambda_2^2} \tag{3-4}$$

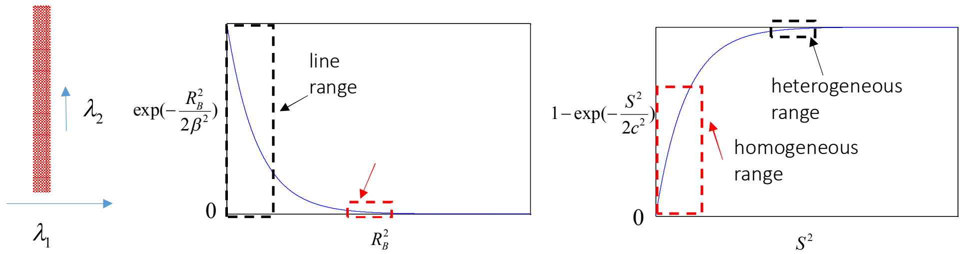

Figure 3-4 Analysis of frangi filter

Analysis of every component of Frangi filter is shown in Figure 3-4. We plot the value of $\exp(-\frac{R_B^2}{2\beta^2})$ and $1-\exp(-\frac{S^2}{2c^2})$ with the relation of R_B^2 and S^2. From the plot image, we can see that the Frangi filter can have a higher value in the line range and heterogeneous range which can make sure the line/vessel structure can be enhanced and extracted.

In our camera captured image, some dark curve structures existed which were considered as the texture, as shown in Figure 3-5 (b). A Gaussian blur filter is applied to the 2D image to decrease noise of the camera captured 2D image. Then a 2D Frangi filter is utilized to the 2D image to segment the texture as described by Eq. (3-4).

Once the 2D texture in image is extracted the corresponding 3D texture point can be obtained. One of the texture extraction result of one porcine brain is shown in Figure 3-5 (c) and Figure 3-5 (d) for each 2D and 3D.

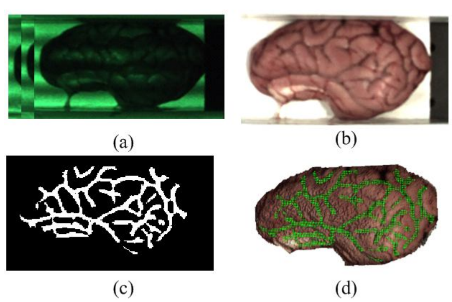

Figure 3-5 Images for brain surface scanning and texture extraction. (a) porcine brain scan (b) porcine brain 2D image (c) porcine brain extraction mask (d) porcine brain extraction 3D texture (green line)

3.3 Corresponding point estimation

In the registration, the corresponding estimation is usually applied to guide the direction of shape deformation, as shown in Figure 3-6. Point **x** is a point in the surface before deformation and **x**' is its estimated corresponding point on the surface after deformation. The estimated corresponding can drive the shape to deform toward the deformed surface.

In the previous research, Sun applied ICP algorithm to register the shape. In ICP, the corresponding is estimated by using closest point. The closest point with the global rigid optimization, the shape can align to the target shape rigidly. Ding *et al.* and Cao *et al.* proposed to use the Robust Point Matching (RPM) proposed by Chui *et al.* to obtain the corresponding point of the texture point. The two corresponding estimation methods either estimate the corresponding only on the surface or only on the texture. Then in our algorithm, we estimate the corresponding point both on the texture space group and the surface space group. Firstly, the measured brain source shape and target shape are separated by Frangi filter into texture points and surface points. Then, the texture point on source find its estimated corresponding point on target texture point by closest point and the surface point on source find its estimated corresponding point on target surface point by closest point. The detail will be described in the following section.

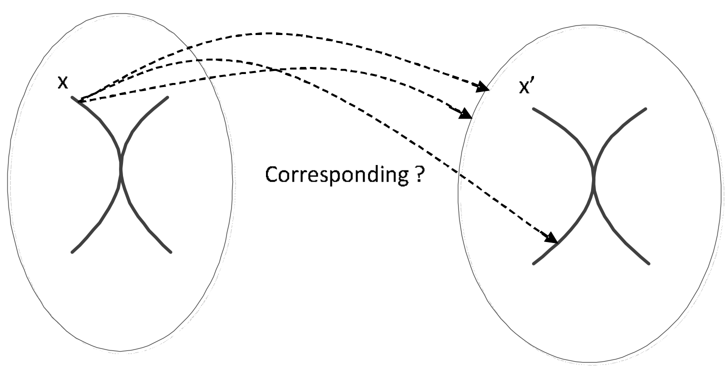

(a) Before deformation (b) After deformation

Figure 3-6 Corresponding finding

As mentioned above, we separated the whole surface into texture points and surface points group. After extracting the 3D texture points on both source and target, the texture points on source surface would estimate its corresponding from texture points on target surface by closest point, as shown in Figure 3-7. In Figure 3-7, the red point is the texture point and the red line suggested the corresponding estimation line. We assign an energy for the texture point the corresponding cost as described in Eq. (3-5)

$$E_{\text{cor\_texture}} = \sum_{i=0}^{k} \| \mathbf{A}_i \mathbf{p}_i + \mathbf{t}_i - \mathbf{p}_i^{\text{cor}} \|^2 \tag{3-5}$$

Where, $\mathbf{p}_i$ and $\mathbf{p}_i^{\text{cor}}$ represent texture point on source and its estimated corresponding point on target, respectively. The k is the total number of texture points. $\mathbf{A}_i$ is the affine matrix of point i and $\mathbf{t}_i$ is the translation vector of texture point with index i.

After estimating texture points' corresponding, the surface points should estimate their corresponding points. Before calculating the corresponding, the whole surface points are uniformly down-sampled. Then surface point on source will find its estimated corresponding point on target surface by closest point, as also shown in Figure 3-7. The cost function is calculated as:

$$E_{\text{cor\_surface}} = \sum_{j=0}^{m} \| \mathbf{A}_j \mathbf{p}_j + \mathbf{t}_j - \mathbf{p}_j^{\text{cor}} \|^2 \tag{3-6}$$

Where, $\mathbf{p}_j$ and $\mathbf{p}_j^{\text{cor}}$ represent surface points on source and its estimated corresponding point on target, respectively. Symbol m is the total number of surface points. $\mathbf{A}_j$ is the affine matrix of point j and $\mathbf{t}_j$ is the translation vector of surface point with index j.

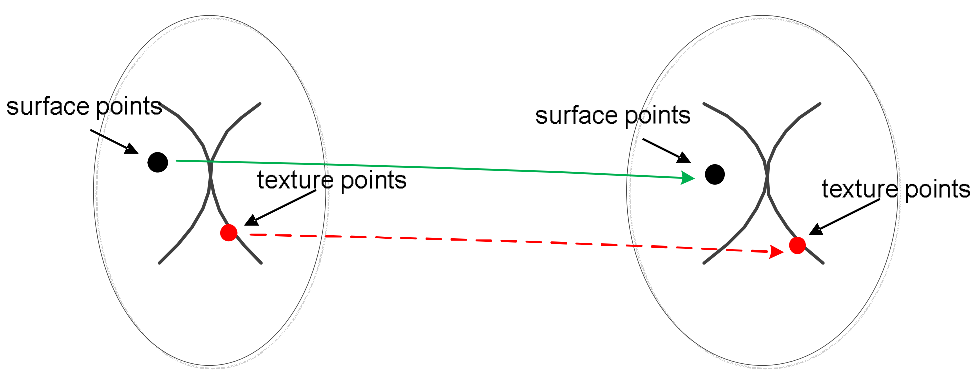

(a) Before deformation (b) After deformation

Figure 3-7 Example of the corresponding point

3.4 Spatial constraint for deformation

After obtaining the corresponding point, the shape should deform by deformation constraint.

In the previous research, Ding *et al.* and Cao *et al.* proposed to apply Thin-Plate-Spine (TPS) to interpolate and deform the brain shape which considering the second deviation of the deformation to be smooth.

3.4.1 Thin Plate Spline (TPS) interpolation and deformation

Generally speaking, thin plate splines are a spline-based interpolation technology for data smoothing and interpolation. It can be used in either 2D or 3D for interpolation. As shown in Figure 3-8, some control points are used to drive the surface to deform and the surface will deformed by TPS.

"Thin Plate" means that a TPS more or less simulates how a thin metal plate would act if it was forced through some control points. TPS for 3 control points is a plane and more than 3 is a curved surface and less than 3 is unknown condition. TPS could be used to deform 2D line or image and particularly popular in representing shape transformations. If there are two equally sized sets of 2D points with **A** being the vertices of the original shape and B the target shape. Then fitting a TPS over points (a_{ix}, a_{iy}, z_i) to get the interpolation function of a translation of points in x direction.

In TPS, there is an energy control function named "regularization" which is used to control how much the shape or the line could deform and also how robust to the noise data. If λ is zero, interpolation is exact and as it approaches infinity, the resulting TPS surface is reduced to a fitted plane.

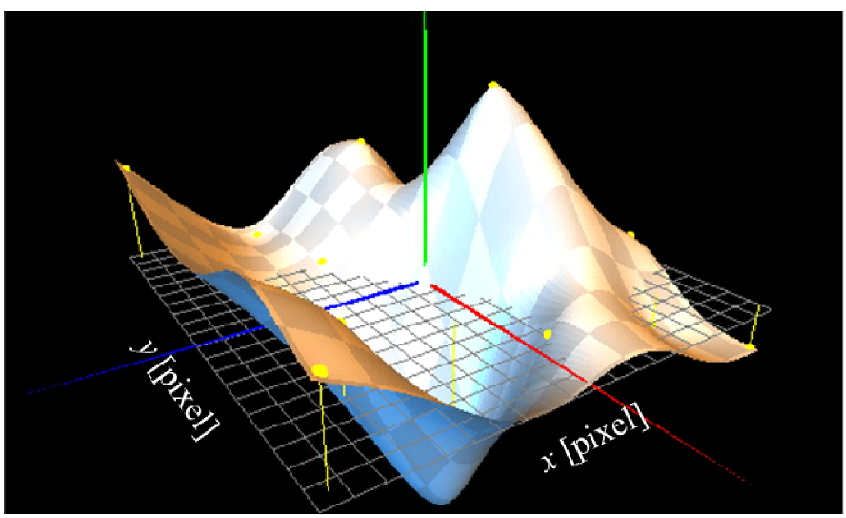

Figure 3-8 Surface deformed by TPS using control points (yellow points)[127]

The mathematical description of TPS could be described as:

$$E_{\text{tps,smooth}}(f)=\sum_{i}^{K}\| y_i - f(x_i)\|^2+\lambda\iint\left[\left(\frac{\partial^2 f}{\partial x_1^2}\right)^2+2\left(\frac{\partial^2 f}{\partial x_1 \partial x2}\right)^2+\left(\frac{\partial^2 f}{\partial x_2^2}\right)^2\right]\mathrm{d}x_1\mathrm{d}x_2 \qquad (3\text{-}7)$$

Where x_i is the control point and λ is the regularization parameter to control deformation magnitude. Next, we will show how TPS can deform a shape by using mathematical equation.

Given a set C of p 3D control points and we could have

$$\begin{Bmatrix} c_{i1}=x_i \\ c_{i2}=y_i \\ c_{i3}=z_i \end{Bmatrix},\ i\in[1....p] \qquad (3\text{-}8)$$

After solving unknown TPS weights w and, we can have a linear equation system.

$$\begin{bmatrix} K\ P \\ P^T O \end{bmatrix}\cdot\begin{bmatrix} \vec{w} \\ \vec{a} \end{bmatrix}=\begin{bmatrix} \vec{v} \\ \vec{o} \end{bmatrix}=Lx=b \qquad (3\text{-}9)$$

Once we calculate the $\vec{w}$ and $\vec{a}$ we can interpolate z for a point (x,y) by

$$z(x,y)=a_1+a_2x+a_3y+\sum_{i=1}^{p} w_i U \qquad (3\text{-}10)$$

From equation 3-10, we can see that TPS is a linear interpolation system. The TPS interpolation result depends on the selection of the control point and it is very difficult to control the deformation only by λ. The deformed shape is very easy to shrink in the deformation.

3.4.2. Proposed deformation constraint

We proposed a smoothness and rigidness constraint to deform the shape. The purpose of smoothness constraint is trying to make the shape deform smoothly and the rigidness constraint is used for making the shape deform rigidly and keep local feature detail as much as possible.

a. Smoothness constraint

When brain deforms, it should deform smoothly. Thus, smooth shape deformation constraint is introduced in our algorithm. In the algorithm, it is not referred to the smoothness of the deformed surface but the smoothness of the actual deformation. In other words, the affine transformations applied to a region of the surface should be consistent with each other. In Figure 3-9, n is the index of current interesting point and q is the index of the k-closest points around the interesting point. To achieve the smooth deformation around point $\mathbf{p}_n$, the local transformation matrix should follow the Eq. (3-11):

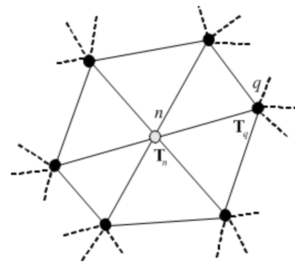

Figure 3-9 Neighbor points

$$E_{\text{smooth}} = \sum_{n} \sum_{q \in N_n} \| \mathbf{T}_n - \mathbf{T}_q \|_{\mathrm{F}}^2 \tag{3-11}$$

where the Frobenius-norm was calculated for the local transformation matrix **T**. By applying the smooth constraint, a smooth deformation of the shape in the local region was maintained and adjacent parts of the source surface were prevented from being mapped to disparate parts of the target surface.

b. Rigid constraint

When brain surface deforming, local feature details should be reserved as much as possible. And when shape deform, the shape should avoid from shrinking. In our method, we use another energy cost E_{rigid} to constraint the deformation rigidly. The E_{rigid} penalizes the deviation of each transformation from a pure rigid motion. Local features deform as rigidly as possible to avoid shearing or stretching artifacts. The cost of rigid constraint is defined by:

$$E_{\text{rigid}} = \sum_i ((\mathbf{a}_1^t \mathbf{a}_2)^2 + (\mathbf{a}_1^t \mathbf{a}_3)^2 + (\mathbf{a}_2^t \mathbf{a}_3)^2) + \sum_i ((1 - \mathbf{a}_1^t \mathbf{a}_1)^2 + (1 - \mathbf{a}_2^t \mathbf{a}_2)^2 + (1 - \mathbf{a}_3^t \mathbf{a}_3)^2) \tag{3-12}$$

Where $\mathbf{a}_1$, $\mathbf{a}_2$ and $\mathbf{a}_3$ are the 3×1 column vectors of affine matrix **A** ($\mathbf{A} = [\mathbf{a}_1 \mathbf{a}_2 \mathbf{a}_3]$).

3.5 Optimization and interpolation

The energy function mentioned above is a nonlinear square least problem. Initially, $\alpha = 10$, $\beta = 100$, $\gamma = 1000$ and all the parameters in the energy function are halved when $|E_K - E_{K-1}| < 10^{-5}(1 + E_K)$ until $\alpha<0.1$, $\beta<0.1$ and $\gamma<1$. The weighting choice of each coefficient will be explained in experiment 4.1. At the beginning, γ is assigned a larger value which means at the beginning, the shape will deform as rigid deformation. And the shape will deform from rigid deformation to non-rigid as the iteration time increasing because γ is released. The adaptation of the weights initially favors global rigid alignment and subsequently lowers the stiffness of the object to allow an increase in the deformation as the optimization progresses. In addition, the large weight for texture points would make the 3D texture act as a skeleton in the registration. The texture point will have the priority to deform toward to their corresponding point.

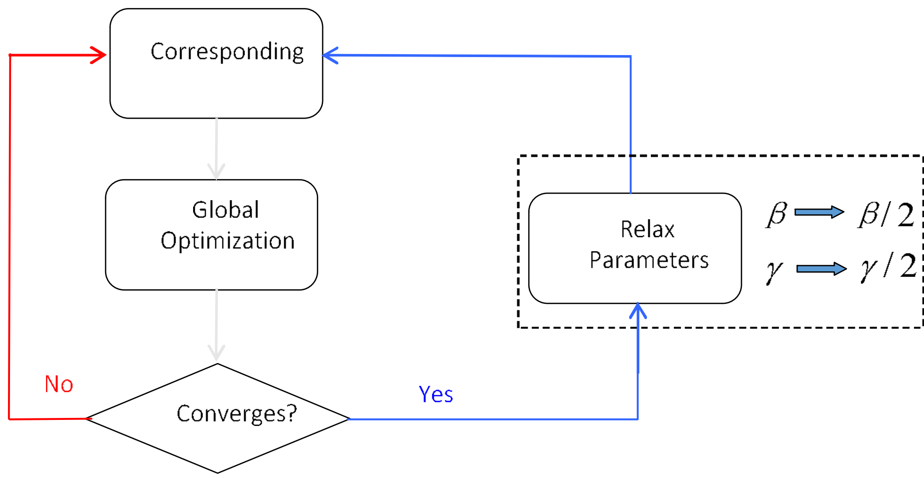

Figure 3-10 Optimization work flow

The optimization procedure is shown in Figure 3-10. We solve this nonlinear least-squares problem by using the Levenberg-Marquardt algorithm[112]. Since the system matrix is sparse, we solve the normal equations in each iteration by a direct solver that employs sparse Cholesky factorization.

The energy function could be described by mathematical function, as shown in equation 3-13

$$\chi^2(p) = \sum_{i=1}^{m}\left[\frac{y(t_i)-\hat{y}(t_i;p)}{w_i}\right]^2 = \mathrm{y}^T\mathrm{W}\mathrm{y} - 2\,\mathrm{y}^T\mathrm{W}\hat{\mathrm{y}} + \hat{\mathrm{y}}\mathrm{W}\hat{\mathrm{y}} \tag{3-13}$$

Where w_i is a measure for the error of y(t_i). The weighting matrix W is the diagonal $W_{ii} = 1/w^2$. The Levenberg-Marquardt adaptively change the parameter updates between gradient descent and the Gauss-Newton methods, as described in equation 3-14.

$$\left[\mathrm{J}^T\mathrm{W}\mathrm{J} + \mathrm{lI}\right]\mathrm{h}_{\mathrm{lm}} = \mathrm{J}^T\mathrm{W}(\mathrm{y}-\hat{\mathrm{y}}) \tag{3-14}$$

Where λ control the algorithm is like Gauss-Newton or gradient descent method. Small value of λ results in a Gauss-Newton method and large step of λ results in a gradient descent method. At the beginning, the parameter λ is assigned a very large value, and as the iteration going, λ is decreased. In the iteration, the solution typically converges rapidly to the local minimum.

The Marquardt's update relationship is

$$\left[J^T WJ + l\,\mathrm{diag}(J^T WJ)\right] h_{lm} = J^T W(y - \hat{y}) \tag{3-15}$$

The result of our registration algorithm is a set of deformed positions for the sampled point on the source surface. After calculating the transformation matrix for sampled points, we extrapolate these deformations to the entire source points by a simple partition of unity approach. Then the new position of point $\mathbf{p}_i$ is given by

$$\mathbf{p}_i' = \sum_{\mathbf{p}_k \in N_{\mathbf{p}_i}} \bar{\theta}_{ik} (\mathbf{A}_k p_i + \mathbf{t}_k) \tag{3-16}$$

Where $\mathbf{A}_k$ and $\mathbf{t}_k$ are the rotation and translation matrix associated with $\mathbf{p}_k$. Normalized weights $\bar{\theta}_{ik} = \theta_{ik} / \sum_l \theta_{il}$ with $\theta_{ik} = \exp(-\|\mathbf{p}_i - \mathbf{p}_k\|^2 / \sigma^2)$ is designed to smoothly decay with increasing distance.

4 Experiments and Results

In this chapter, selection of energy function coefficients is conducted. Also, the 3D measurement, non-rigid registration and projection accuracy are evaluated. For evaluating the 3D measurement accuracy, 20 metal balls were used and bias and precision error are evaluated. Moreover, five porcine brains were used to evaluate the registration accuracy by calculating Residual Error (RE) and Target Registration Error (TRE) using OPTOTRAK.

4.1 Selection of energy function coefficients

4.1.1 Purpose

As different energy function coefficients will generate different registration results, selection of the proper coefficients is important. Thus, we set up an experiment in order to obtain acceptable coefficients.

4.1.2 Materials and Method

Surface registration error and texture registration error with respect to three coefficients α, β, γ were evaluated. Distribution of surface registration error and texture registration error were mapped (Figure 4-1), and three coefficients are selected which give us small surface registration error and texture registration error. One porcine brain data was used as the object for calculation. We changed the value of coefficient α, β and γ from 1 to 10^7 and increased it 10 times of its value for each interval. Detail of experimental conditions is shown in Table 3.

Table 3 Experimental conditions

Object	Porcine brain
Total point number	12642
Texture point number	2662
α range	1, 10, 10^2, 10^3, 10^4, 10^5, 10^6
β range	1, 10, 10^2, 10^3, 10^4, 10^5, 10^6
γ range	1, 10, 10^2, 10^3, 10^4, 10^5, 10^6

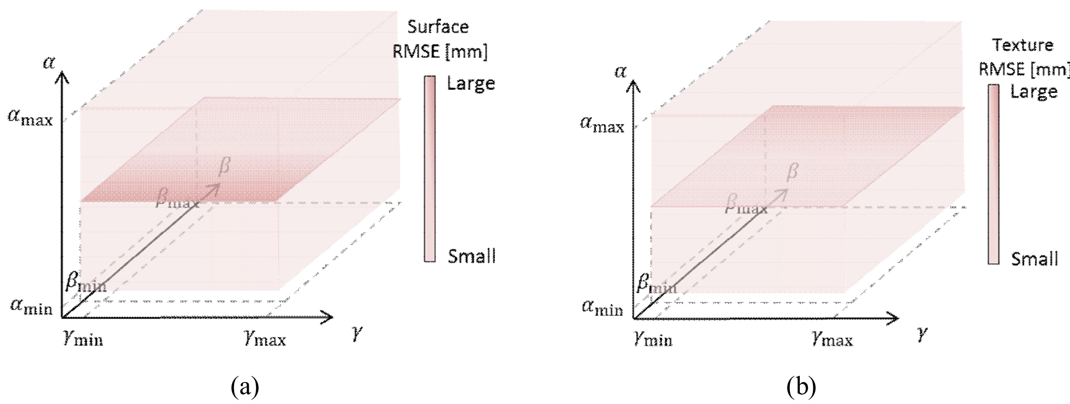

Figure 4-1 3D mapping of (a) surfaceRMSE and (b) texture RMSE with respect to different coefficients

4.1.3 Result

The registration error distribution of different α is shown in Figure 4-2. The result showed that when α is larger than 1000, the registration error increases throughout the whole range of β, γ. Thus we only consider α = 1, 10 and 100 for further investigation.

The enlarged scale of surface registration error and texture registration error at α = 1, 10 and 100 are shown in Figure 4-3 and Figure 4-4, respectively. Figure 4-3 and Figure 4-4 showed that α = 10 has smaller surface registration error and texture registration error than that registration in α = 1 and 100. α = 10 might be one of the acceptable coefficient. Therefore, we set α is equal to 10.

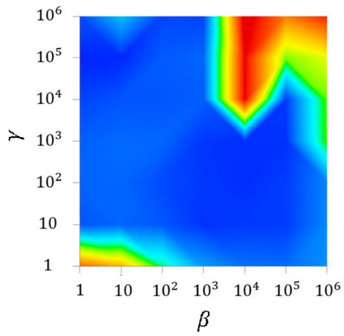

(a) $\alpha = 1$

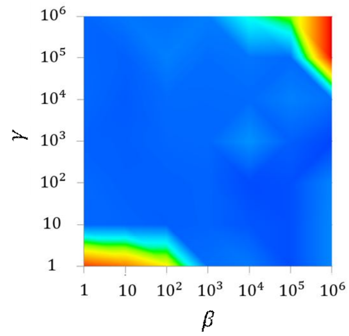

(b) $\alpha = 10$

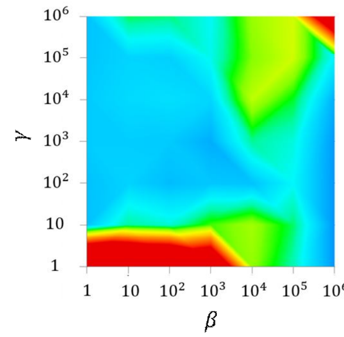

(c) $\alpha = 10^2$

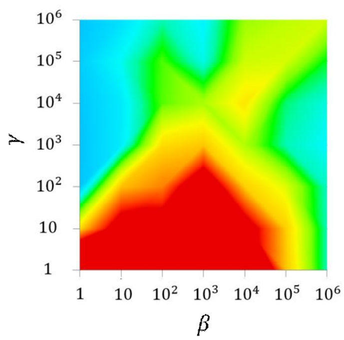

(d) $\alpha = 10^3$

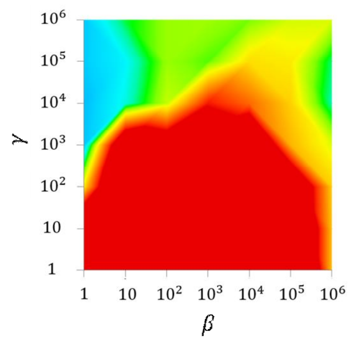

(e) $\alpha = 10^4$

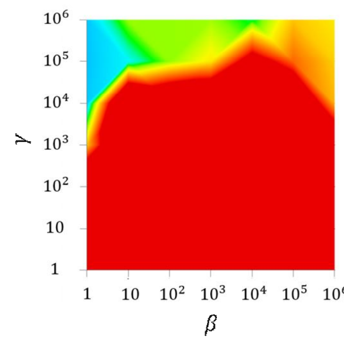

(f) $\alpha = 10^5$

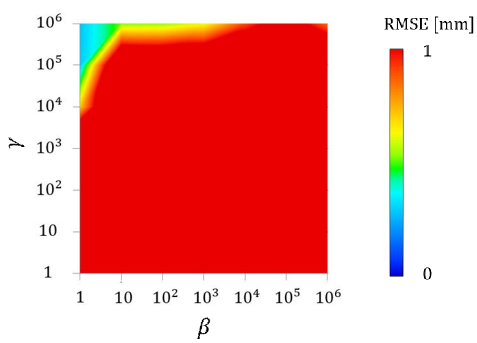

(g) $\alpha = 10^6$

Figure 4-2 Registration error at different α

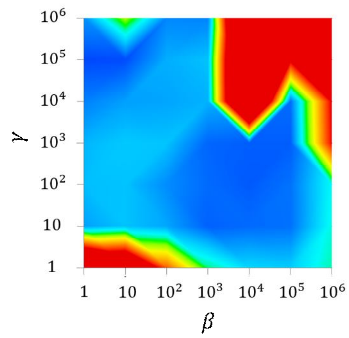

(a) $\alpha = 1$

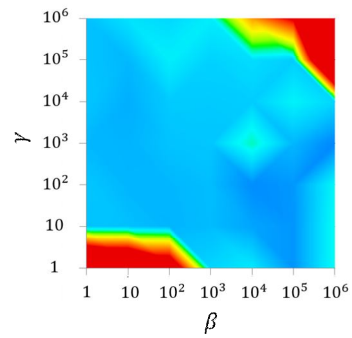

(b) $\alpha = 10$

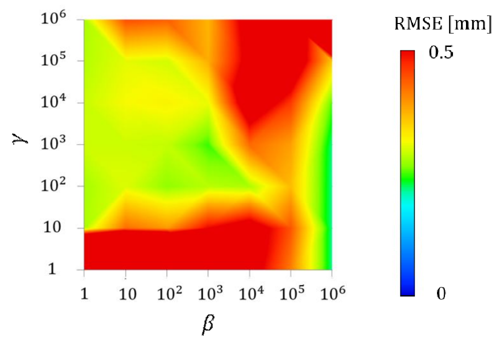

(c) $\alpha = 10^2$

Figure 4-3 Scale enlarged surface registration error when $\alpha = 1$, 10 and 100

Some typical registration results with combination (β, γ) when α = 10 are shown in Figure 4-5. Combination of (1,5) and (5,1) showed the obvious over-rigid and over-smooth registration result; (3,3) showed an improvement from (3,2) but (3,4) is over-rigid from (3,3). The combination (2,3) generate the accecptable result. Thus we decided to use the coefficient (10, 100, 1000) as the "estimated" coefficients.

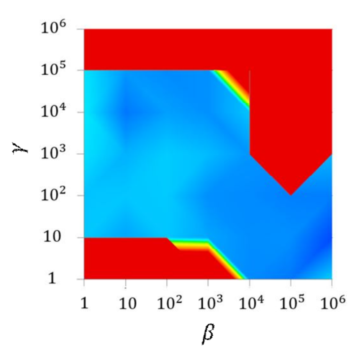

(a) $\alpha = 1$

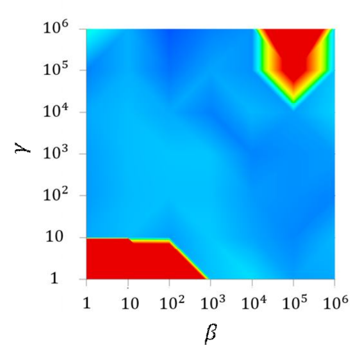

(b) $\alpha = 10$

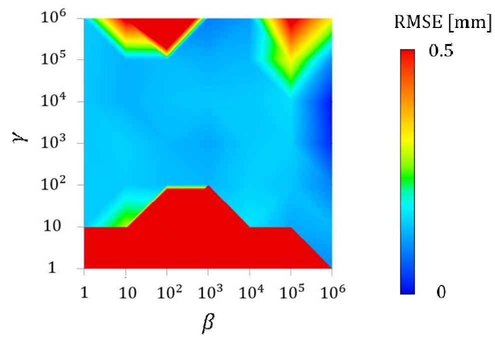

(c) $\alpha = 10^2$

Figure 4-4 Texture registration error at different α

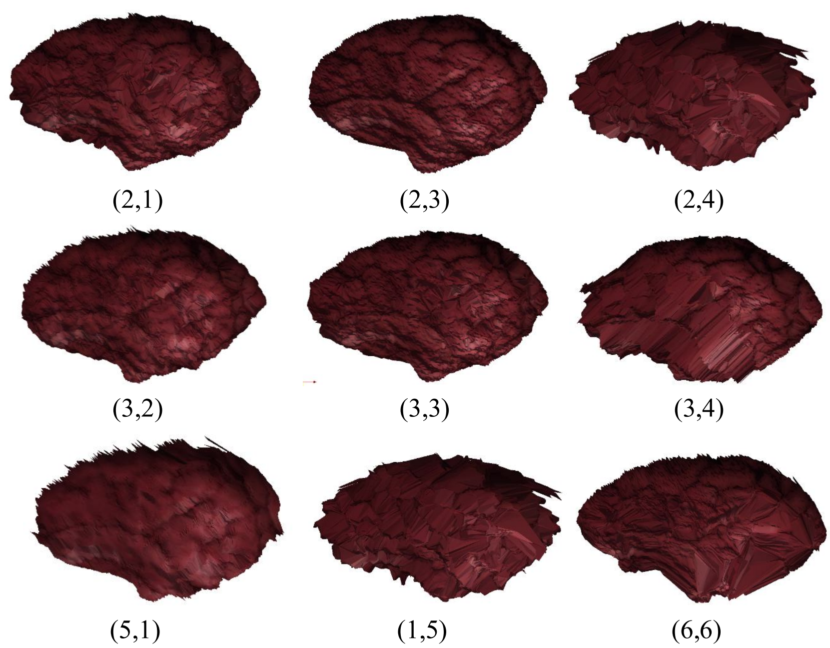

Figure 4-5 registration result of (β, γ) when α = 10

In the energy function, the weight of E_{shape} is considered as 1. As the coefficient α changes, the weight of E_{shape} and E_{texture} will change. Thus, we further investigate the balance of E_{shape} and E_{texutre} on registration accuracy. We calculate the surface registration error and target registration error at different α with fixing β and γ as 100 and 1000. The quantitative result is shown in Figure 4-6. In Figure 4-6, the horizontal axis is the different α value; the vertical axis shows the registration result. The red line is the texture residual error and the black line is the surface residual error. It showed that at the beginning, when α is increasing from 0, the registration leads a larger surface residual error around 0.2 mm and texture residual error around 1.6 mm. With the increasing of α, the surface residual error and texture residual error both decrease to around 0.1 mm. While α keep increasing, the surface error increases again. To be specific, the qualitative result when α = 0, 10, 50, 500 is shown in Figure 4-7. The result in Figure 4-7 showed that when α is 0, during the registration only shape points was used for registration. When α increased to 10, the registration results seems reasonable for both texture and shape alignment. As α keeps increased to 50, the relatively weight for other shape points will decrease and we can see a larger misalignment of the surface, shown in Figure 4-7(c). Moreover, the relative weight of smooth and rigid also reduced and the texture become "soft" and some shrink error appear, shown in Figure 4-7 (g). Thus, smaller α fails to work well but too large α will cause shape alignment error.

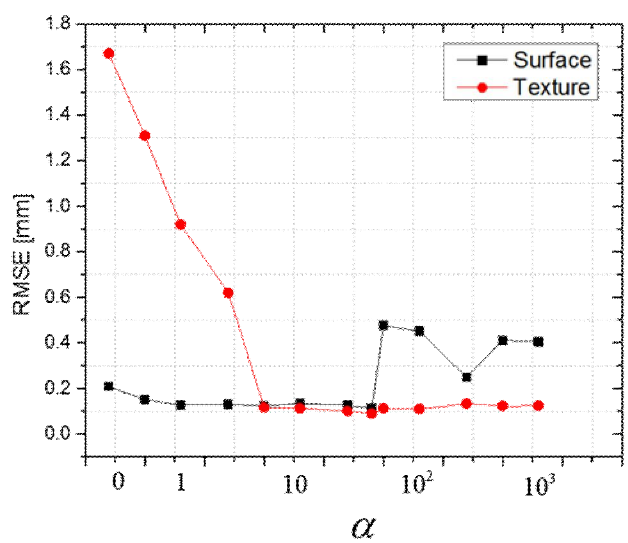

Figure 4-6 Registration error regarding on different α

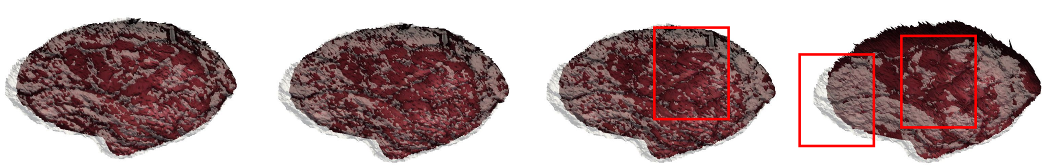

(a) α = 0 (b) α = 10 (c) α = 50 (d) α = 500

Registration result

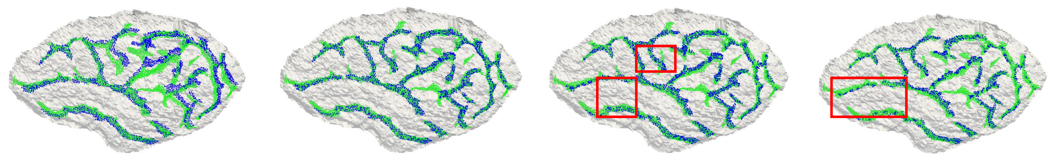

(e) α = 0 (f) α = 10 (g) α = 50 (h) α = 500

Texture alignment

Figure 4-7 registration result and texture alignment

4.1.4 Discussion

In the energy function, there are three parameters, α, β, γ which can influence the registration result (acutually there are four parameters but during optimization, we set the coeffcient of E_{shape} as constant value 1). The larger the α is, the easier the texture alignment will be. However, a relatively larger α would make the E_{shape} relatively smaller and it produces a larger registration error as shown in Figure 4-2 (d)-(f). On the other hand, a small α, such as in case of $\alpha = 1$ causes larger texture alignment error because texture points have lower weight during registration, as shown in Figure 4-4.

The larger the γ is, the more detail of the shape can be conserved during registration (not over large), however, higer γ might cause longer computing time since γ controls the coefficient of E_{rigid} which has a $O(n^4)$ computing complexity. On the other hand, a smaller γ or relatively larger β would lead over-smooth of surface and the brain would shrink during registration. Therefore, from Figure 4-5 we chose γ as 1000 when α is equal to 10 and β as 100 when fixing $\alpha = 10$. Currently, we set a larger γ for the E_{rigid} since we wanted to keep the brain shape deforming as rigid as possible, especially the brain real deformation in clinical surgery would be larger and elastic. Such kind of rigid deformation can prevent brain shrink during registration. A larger γ would make the brain deformation from rigid to non-rigid in the optimization procedure.

In Figure 4-6, the texture residue and surface residue is reduced to around 0.1 mm when $\alpha = 5$. Also we found the ratio between shape point and texture point is around 4. Then choosing of α for balance shape and texture might should consider the point ratio between shape point and texture point to balance their contribution during registration. Further investigation of the ratio between shape points and texture points of other four porcine brains showed a value of 4.51. Moreover, we want to make the texture point would work as deformable skeleton during registration, we assign $\alpha = 10$ as the coefficient value for the E_{texture} component. Even this might not be an optimal value, it is an acceptable value considering the shape points is larger than texture point number.

The energy function is a global energy function and every coefficient influent others. In fact, the parameters rely on the input data size, the texture number, initial deformation magnitude and so on. Currently, we chose α, β and γ with acceptable values. In the future, we might need to use our method in the real human brain surface registration. In that circumstance, more brain data is needed to be evaluated in order to obtain the optimized coefficient values.

4.2 Evaluation of 3D Measurement Accuracy

4.2.1 Purpose

The purpose of this experiment is to evaluate the 3D shape measurement accuracy. 3D shape measurement is very important and the basic requirement for our registration method since we combine surface and texture for evaluation.

4.2.1 Materials and Method

To evaluate the 3D shape measurement accuracy, bias error and precision error of 20 spherical metal balls were used, as shown in Figure 4-8. The bias error can reflect the 3D displacement error while the precision error can show the local surface variation error. The 20 spherical metal sphere balls with 8 mm diameter were aligned in 4×5. The measurement distances *d* is calculated from the bottom plane to the front of camera, shown in Figure 4-9. Commercial scanner (Range 7/Range 5) is used to measure a golden standard value of 3D surface of balls, as shown in Figure 4-10. The experimental conditions are listed in Table 4:

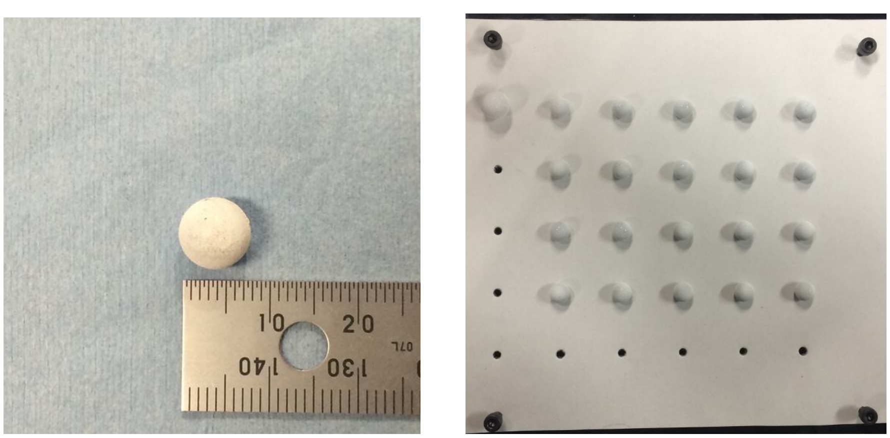

(a) Spherical metal ball with 8 mm diameter (b) 4×5 alignment of balls

Figure 4-8 Spherical metal balls used in 3D shape measurement evaluation

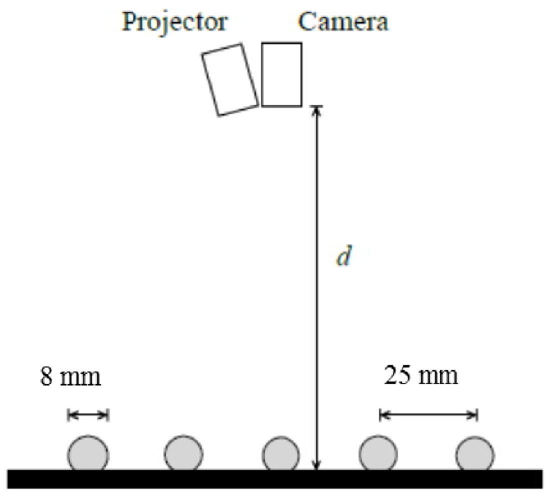

Figure 4-9 Scheme of the 3D measurement evaluation experiment

Figure 4-10 Commercial scanner (Range5/Range7) used for evaluating the 3D surface measurement accuracy

Table 4 3D measurement experiment conditions

Laser projector	SHOWWX, MICROVISION Inc.
Camera	IDP Express R2000, Photron Inc.
Distance *d* [mm]	250, 275, 300, 325, 350, 375, 400
Metal ball diameter ϕ [mm]	8
Metal ball accuracy [mm]	0.037±0.009
Metal ball number	20 (4×5)
Measurement Time	10
Scanner	Range7/Range5 Accuracy: ±40 µm [128]

1. 3D Measurement Bias Error

In 3D measurement, the bias error exists which is cause by the calibration. The bias error can cause some displacement in the 3D coordinates. We used 20 spherical metal balls and measured their centers and then the balls were scanned by using the commercial 3D scanner Range7/Range5 with an accuracy: ±40 µm.

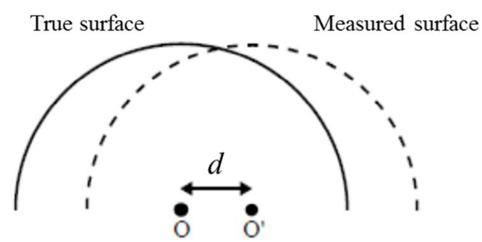

Figure 4-11 Bias error. *d* is the bias error to show the distance between the center of measured surface to the true surface

In Figure 4-11, the bias error of the sphere is calculated by

$$E_{\mathrm{bias}} = d = |\mathrm{O} - \mathrm{O}^{'}| \qquad (4\text{- }1)$$

Where O and O' are the measured sphere center and the sphere center measured by Range7/Range 5. The bias error is calculated by the distance between the measured sphere center and the real sphere center, as described in the equation 4-1.

2. Precision Error

In 3D measurement, there exists another error which is called precision error, as suggested in Figure 4-12. Precision error can reflect the local surface variation which is also influenced by system calibration.

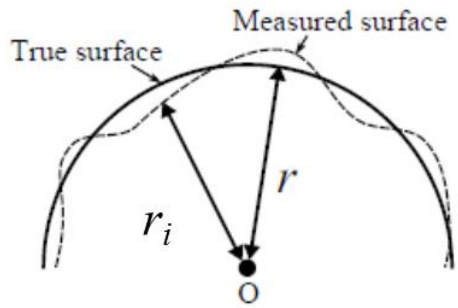

Figure 4-12 Precision error. Precision error shows the difference between the estimated sphere radius and the true sphere radius

The measurement precision error is calculated by the difference between the measured radius and the "real" radius, as described in the equation 4-2:

$$E_{\text{precision}} = \sqrt{\frac{\sum_{i=1}^{N}(r_i - r)^2}{N}} \qquad (4\text{- }2)$$

Where r is the real sphere radius and r_i is the estimated radius.

4.2.2 Result

The measured surface of 20 spherical metal balls at the distance of 250 mm is shown in Figure 4-13. The 3D measurement bias error is shown in Figure 4-14 with respect to the distance of 250, 300, 350, and 400 mm. The color of the figure means the magnitude of the bias error. It was shown that the bias error increased at the boundary of the measurement area. Also, it was shown that the bias error increased when measurement distance increased.

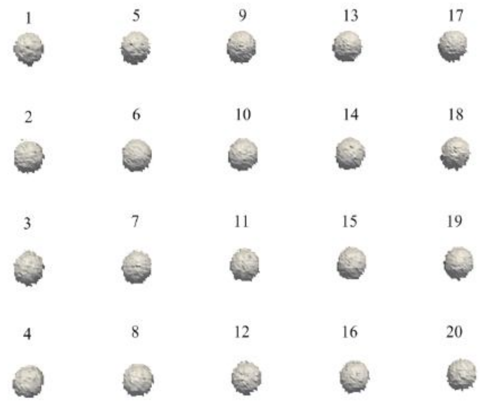

Figure 4-13 Measured surface of spherical metal ball at 250 mm distance

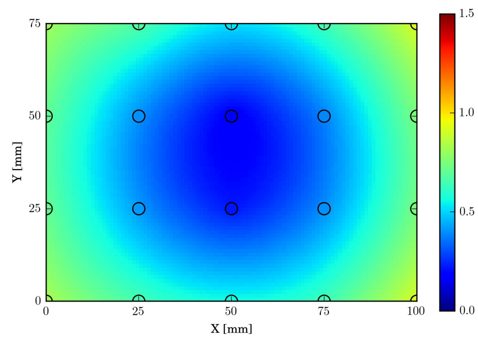

(a) d =250 mm

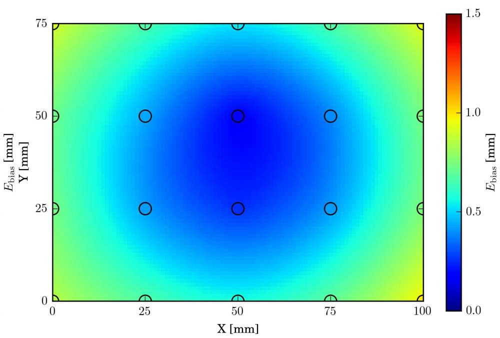

(b) d = 275 mm

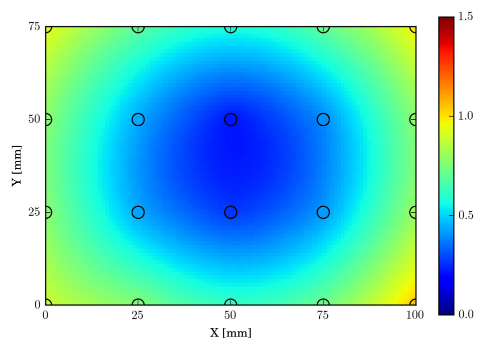

(c) d = 300 mm

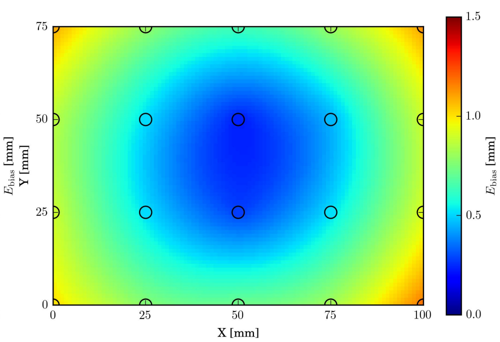

(d) d = 325 mm

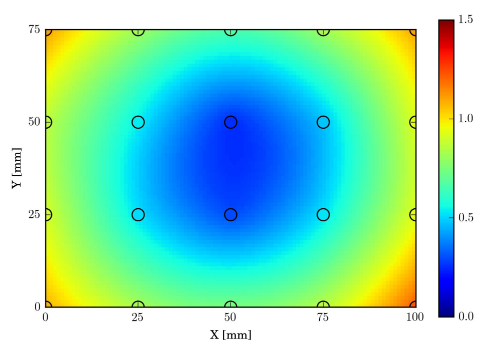

(e) d = 350 mm

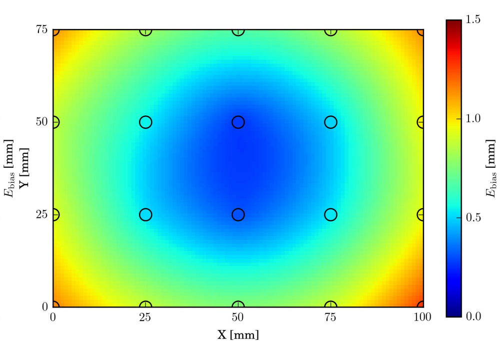

(f) d = 375 mm

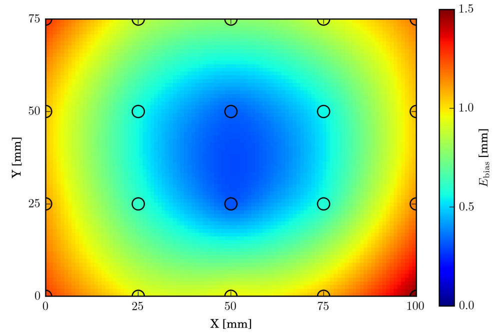

(g) d = 400 mm

Figure 4-14 Bias error distribution with respect to the different measurement distances

The 3D measurement precision error is shown in Figure 4-15. It was shown that the precision error increased as the measurement distance increased. Also, the precision error increased in the boundary of the measurement area.

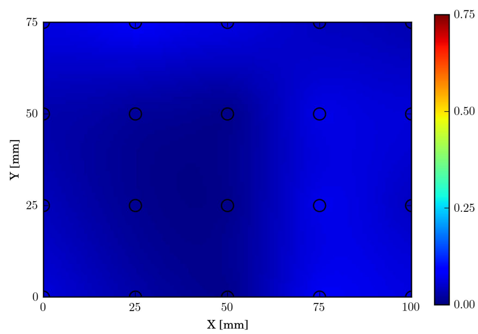

(a) d = 250 mm

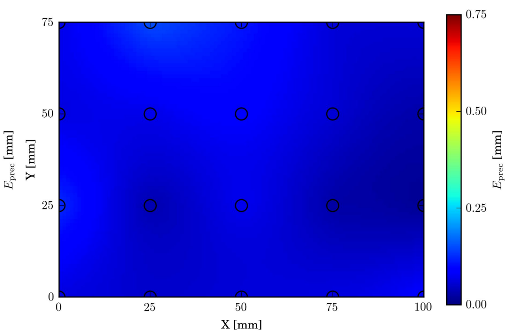

(b) d = 275 mm

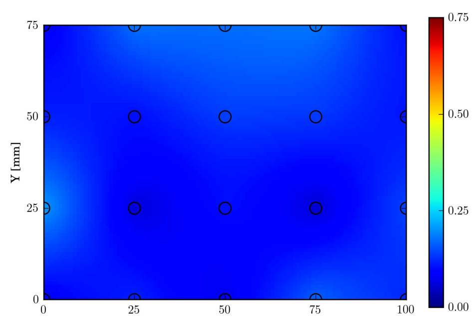

(c) d = 300 mm

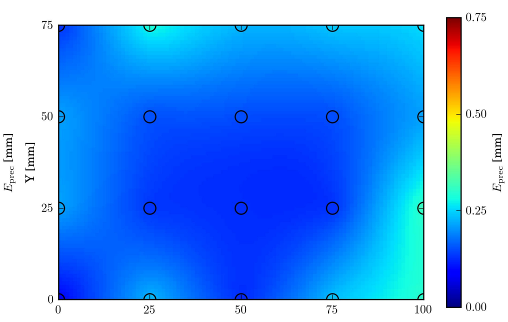

(d) d = 325 mm

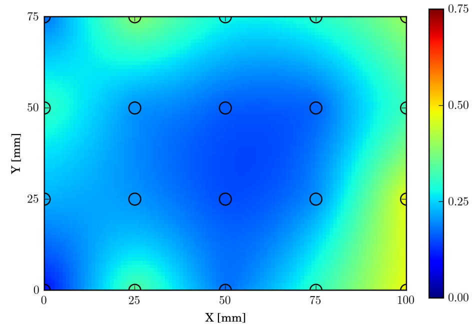

(e) d = 300 mm

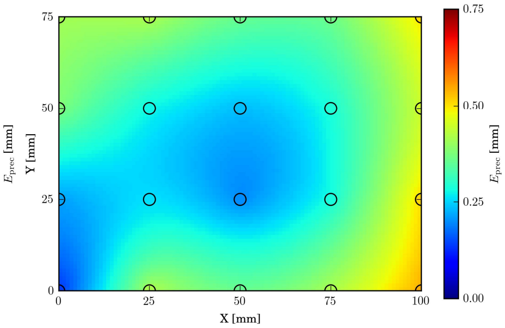

(f) d = 325 mm

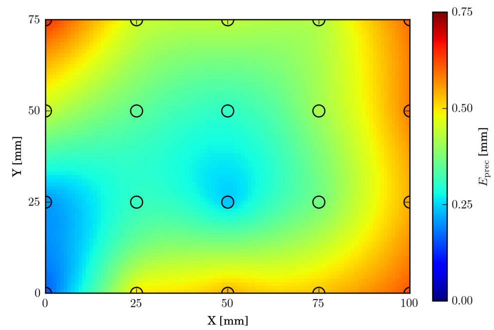

(g) d = 400 mm

Figure 4-15 3D measurement precision error distribution with respect to different distances

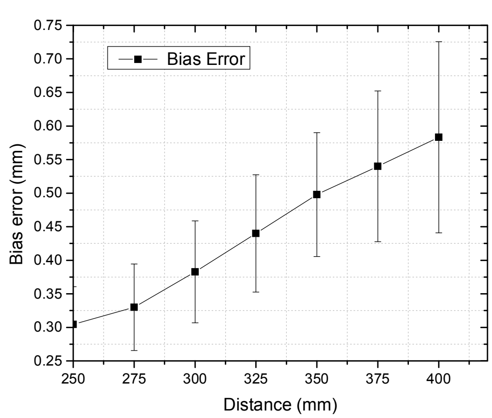

(a) Bias error

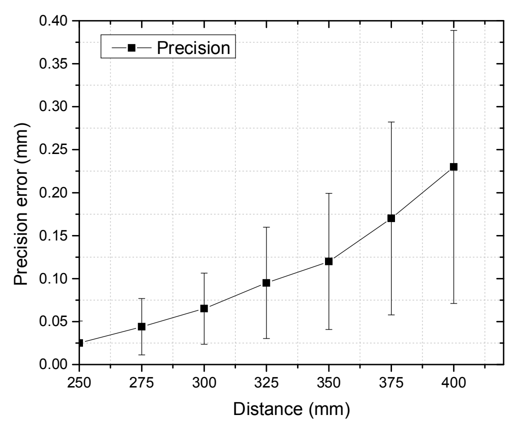

(b) Precision error

Figure 4-16 3D measurement error with respect to measurement distance

The quantitative result of the bias error and precision error is shown in Figure 4-16. The measured maximum and minimum bias error was 0.57 mm on average (distance of 400 mm) and 0.31 mm on average (distance of 250 mm), respectively; moreover, the measured maximum and minimum precision error was 0.27 mm on average (distance of 400 mm) and 0.025 mm on average (distance of 250 mm), respectively. Both results showed that when measurement distance increased, error increased.

4.2.3 Discussion

In this experiment, the 3D measurement accuracy was evaluated. The errors we evaluated include bias error and precision error. We scanned the 20 spheres and then we estimated the sphere centers and the radius of every sphere. The bias error, which indicates 3D measurement shift in 3D space, was calculated as the distance between the assessed sphere center and the real sphere center. The precision error, which reflects the local surface point variation, was computed using the radius difference between the measured sphere and the real sphere surface.

For both of these two error distribution, it showed that as shown in Figure 4-14 and Figure 4-15, the boundary error is larger than the center. This kind of error distribution is because the used projector has non-linear distortion and such kind of error distribution is consistent with the projector distortion model we calculated (Figure 2-19). In the further research, the boundary error could be reduced by a more accurate system calibration technology or a less-distorted projector might be used for measurement.

As shown in Figure 4-16 (a) and (b), both bias error and precision error increased when measurement distance increased. The bias error mainly related to the distortion of the projector. As the projector distortion degree increased with distance, the bias error keep the same trendency. The precision error increasing mainly caused by the distance. As the measuring distance increases, the increased distance might go out the range of our system calibration, and then the error might increase. Moreover, in the evaluation method, the 20 metal balls were used. And the estimated sphere centers were used to calculate the bias error. When the measurement distance increased, the point resolution decreased, and the number of points used to estimate sphere center will be fewer since the spherical ball is shown as small area in the 2D captured image. Thus the sphere fitting error will increase. So, when the distance increase, the bias error will increase.

Currently, the minimum measurement distance was chosen to 250 mm and we did not evaluate with shorter measurement distance because the 250 mm is known as the appropriate measurement distance used in clinical situations by other research group. As the result showed, the measurement accuracy was decreasing while measurement distance increasing. Under this circumstance, we did not evaluate the further longer measurement distance and the longest distance evaluated is 400 mm for evaluation.

4.3 Simulation experiment

4.3.1 Purpose

The purpose of this experiment is to evaluate the registration error of proposed method by simulation using surface with different curvatures, deformation magnitudes and texture number.

4.3.2 Materials and method

We simulated the non-rigid registration with cylinerical shape which is shown in Figure 4-16. This simple shape structure is the ideal shape to evaluate the proposed method on different parameters. The total point number size is 80 (horizontal) ×60 (vertical) in the plane.
Firstly, in order to evaluate the influence of texture direction, we rotated the texture from 0 degrees to 90 degrees with 15-degree increment, as shown in Figure 4-18. The parameter details are listed in Table 5. 3. The source surface shape curvatures were 0.015, 0.020, 0.025 and 0.030, shown in Figure 4-20. Larger curvature causes larger surface deformation and smaller curvature causes smaller surface deformation. The surface shape curvature 0.005 was considered as the target surface for registration. The texture frequency was fixed at 1/5.
Secondly, we also evaluated the influence of texture frequency by increasing the distance between the texture lines, as shown in Figure 4-19. The texture frequency was defined as the reciprocal of distance d between textures, shown in equation 4-2. When the distance d increases, the frequency is decreased. And also, by controlling and changing the curvature of the surface, we could deform the plane, as shown in equation 4-3. By doing this, we tried to evaluate the registration accuracy with respect to different curvatures, which showed the deformation magnitude, as shown in Figure 4-20. The detail of the experimental parameters is listed in Table 6. In this experiment, the texture direction was kept 0° direction (vertical direction).
Moreover, we evaluated the accuracy of the proposed method with the deformation along the surface, described by Equation 4-4, which showed the divergence deformation and shear

deformation, shown in Figure 4-21. In Figure 4-21 e_{xx}/e_{yy} is the normal strain in x and y direction; the e_{xy}/e_{yx} is the shear strain. The norm strain can determine the deformation in normal direction without any angle change along axis while the shear strain reflects the deformation with angle changing along axis. The experimental details are listed in Table 7. The texture direction was kept 0 degrees and texture frequency was kept at 1/5. Divergence strain and shear strain were set to 0.01, 0.02, 0.03, 0.04, and 0.05. Figure 4-21 showed the divergence deformation and shear deformation at 0.05 with curvature 0.030 for evaluation.
The experiment results were compared with TPS based registration method [116] [114] [115], which uses vessels for corresponding points and TPS for global deformation.

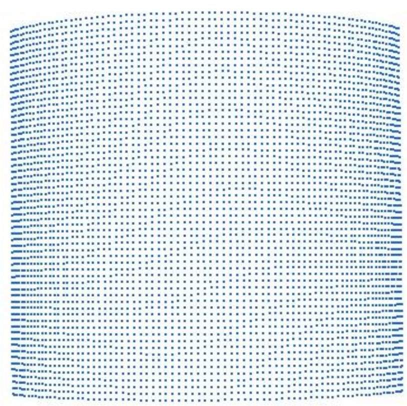

Figure 4-17 Simulated cylinder with 80×60 points.

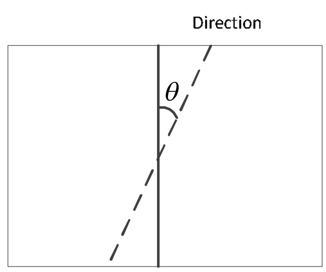

(a) Texture direction schematic diagram

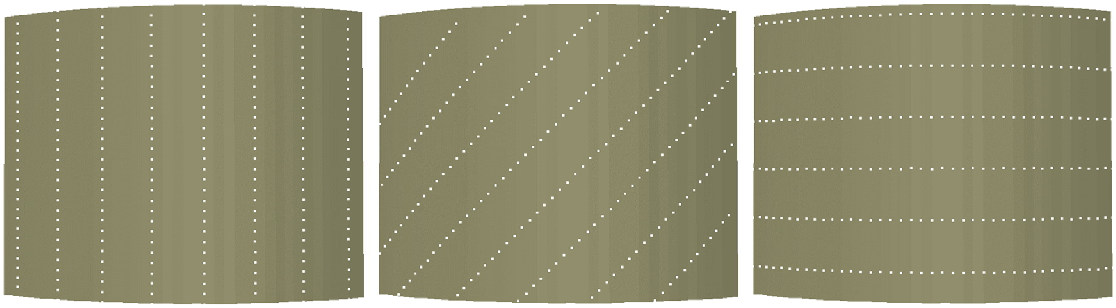

(a) 0 degrees (b) 45 degrees (c) 90 degrees

Figure 4-18 Texture direction of 0, 45 and 90 degrees

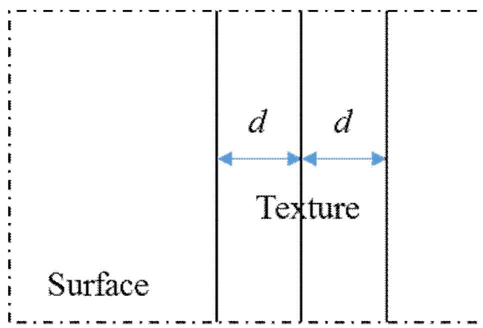

(a)Texture frequency schematic diagram

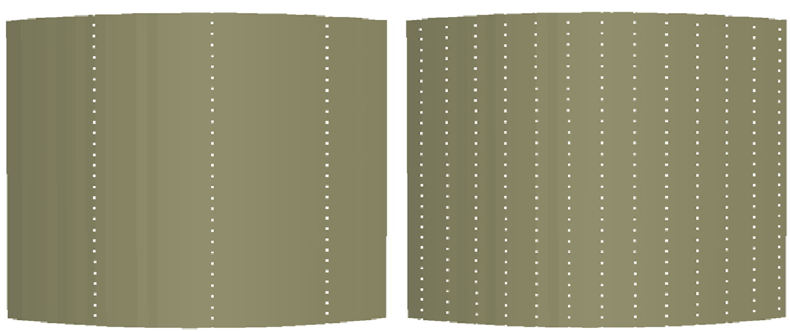

(b) Texture frequency at 1/11 (c) Texture frequency at 1/3

Figure 4-19 Texture frequency of 1/11 and 1/3

$$f = \frac{1}{d} \tag{4- 3}$$

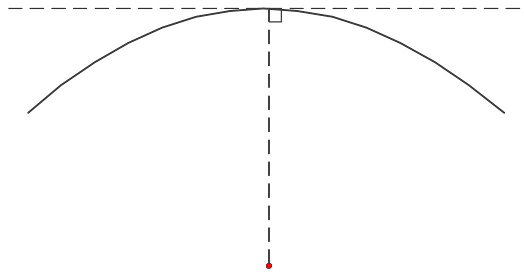

(a) Shape curvature schematic diagram

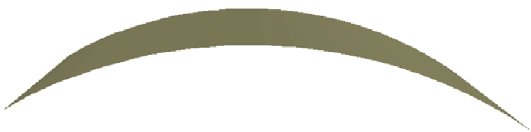

(b) Curvature of 0.030 (c) Curvature of 0.010

Figure 4-20 (a) example of shape curvatures (b) curvature of 0.030 (c) curvature of 0.010

$$\kappa = \frac{1}{r} \tag{4- 4}$$

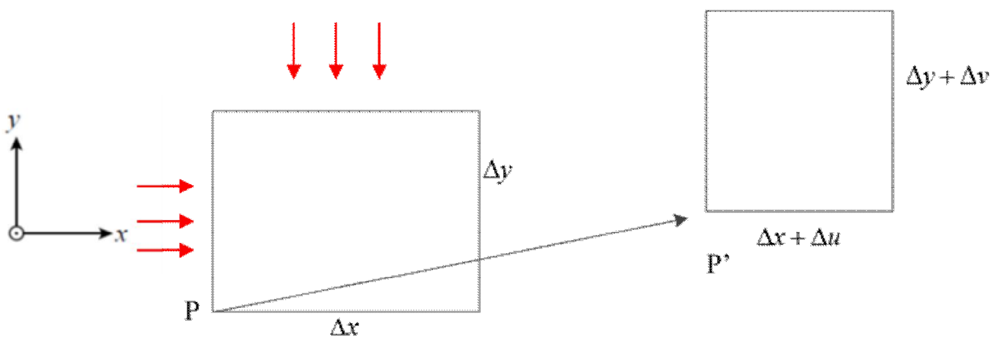

(a) Divergence deformation

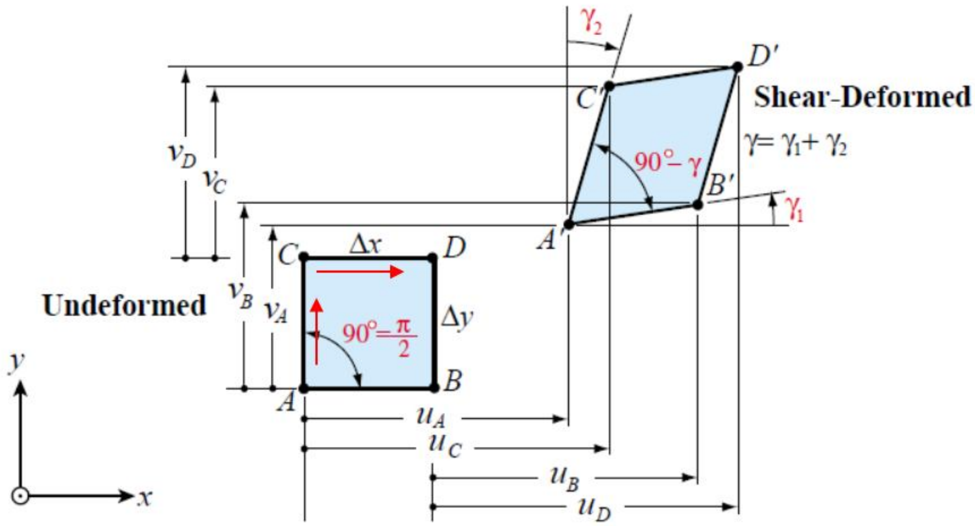

(b) Shear deformation

Figure 4-21 Divergence deformation and shear deformation

$$\nabla V = \begin{bmatrix} e_{xx} & e_{xy} \\ e_{xy} & e_{yy} \end{bmatrix} + \begin{bmatrix} 0 & \omega \\ -\omega & 0 \end{bmatrix}$$

$$\omega = \frac{1}{2}\left(\frac{\partial u}{\partial y} - \frac{\partial v}{\partial x}\right) \tag{4- 5 }$$

$$e_{xx} = \frac{\Delta u}{\Delta x} \quad e_{xy} = \frac{1}{2}\left(\frac{\Delta u}{\Delta y} + \frac{\Delta v}{\Delta x}\right)$$

Table 5 Simulation experiment 1: different texture directions with different curvatures

Object	Cylinder with Texture
Point Number	4800 (80×60)
Texture Direction θ [deg.]	0, 15, 30, 45, 60, 75, 90
Curvature κ [mm^{-1}]	0.015, 0.020, 0.025, 0.030
Texture frequency f [mm^{-1}]	1/5

Table 6 Simulation experiment 2: different shape curvatures and different texture frequencies

Object	Cylinder with Texture
Point Number	4800 (80×60)
Texture frequency f [mm^{-1}]	1/3,1/4, 1/5, 1/6, 1/ 7, 1/8, 1/ 9, 1/10, 1/ 11
Texture Direction θ [deg.]	0
Curvature κ [mm^{-1}]	0.015, 0.020, 0.025, 0.030

Table 7 Simulation experiment 3: different shear/divergence deformations

Object	Flat Plane with Texture
Point Number	4800 (80×60)
Texture Direction θ [deg.]	0
Texture frequency f [mm^{-1}]	1/5
Curvature κ [mm^{-1}]	0.030
Divergence strain: $\varepsilon_{xx}/\varepsilon_{yy}$	0.01, 0.02, 0.3, 0.04, 0.05
Shear strain: $\varepsilon_{xy}/\varepsilon_{yx}$	0.01, 0.02, 0.3, 0.04, 0.05

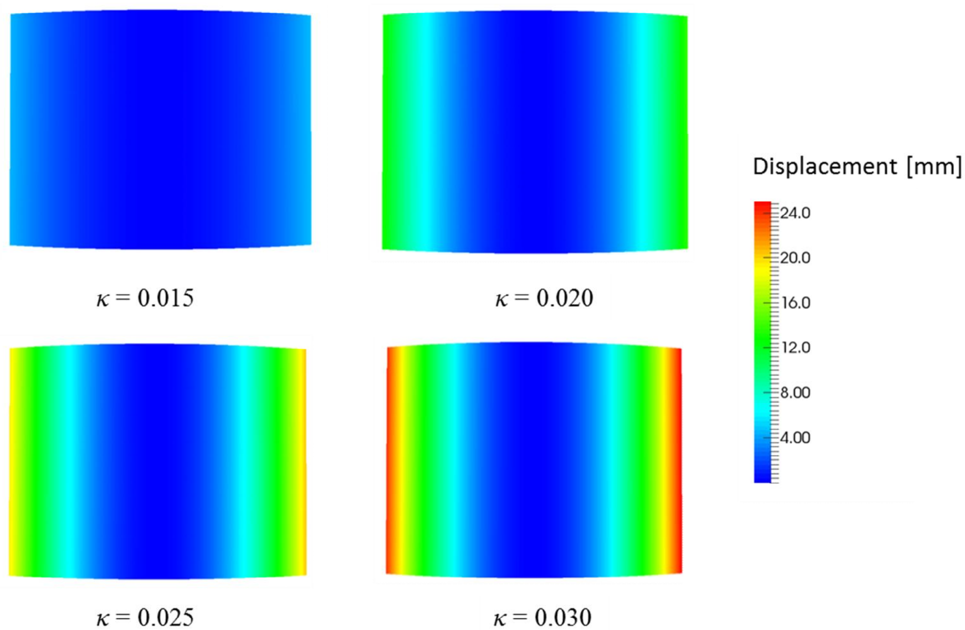

Figure 4-22 Deformation magnitude with respect to different curvatures

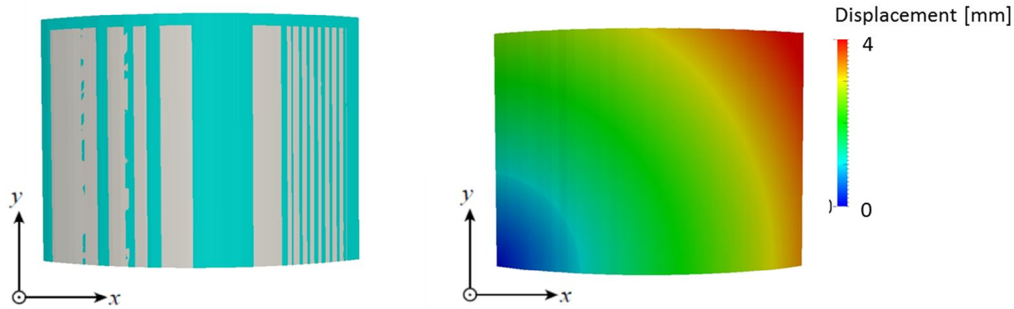

(a) Divergence deformation (b) Divergence deformation magnitude

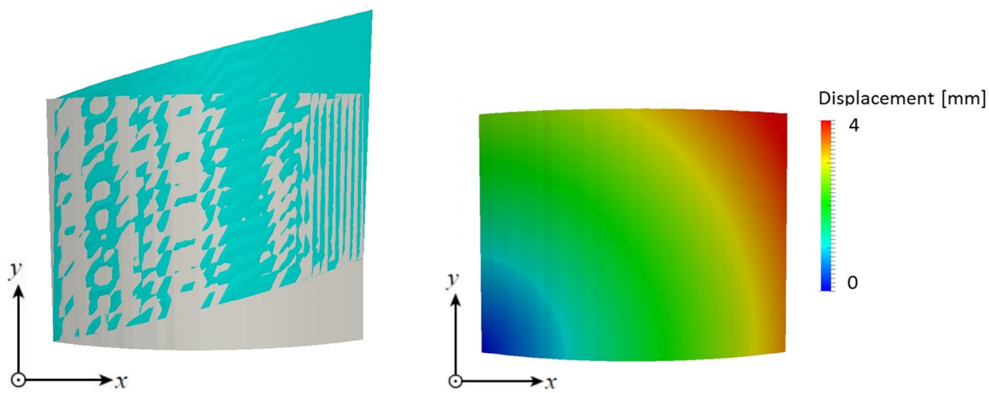

(c) Shear deformation (d) Shear deformation magnitude

Figure 4-23 Deformation magnitudes with respect to different divergence and shear strain

4.3.2 Result

The registration accuracy of the proposed method with regard to different curvatures with different texture directions are shown in Figure 4-24. The registration accuracy of TPS based method is shown in Figure 4-25.

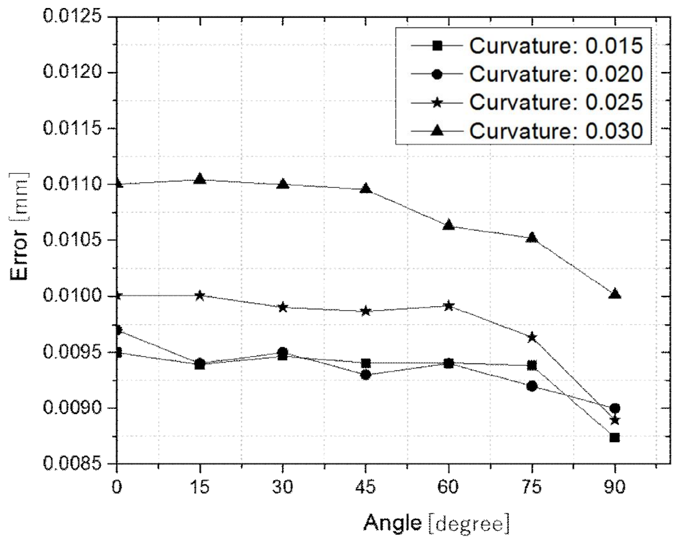

Figure 4-24 Registration result regarding on different texture directions and shape curvatures of the proposed method

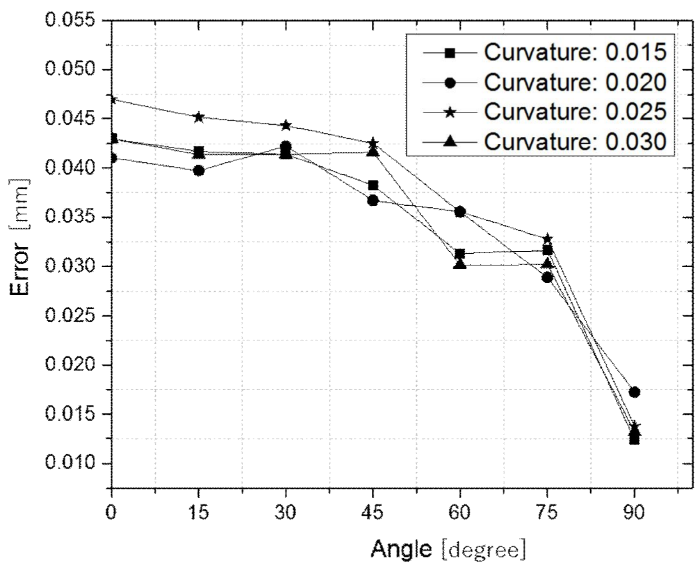

Figure 4-25 Registration result regarding on different texture directions and shape curvatures of the TPS based registration

The result showed that both the proposed method and TPS based registration method accuracy increased with the increase of texture direction. When the curvature increase, the proposed method accuracy is kept almost unchanged (around 0.01 mm), however, the TPS based registration showed relatively large increase.

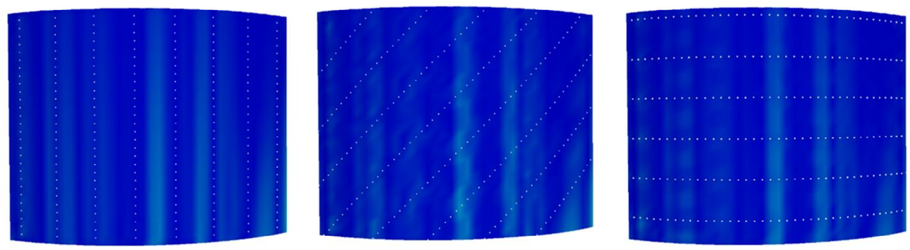

(a) Proposed: $\theta = 0$ degrees (b) Proposed: $\theta = 45$ degrees (c) Proposed: $\theta = 90$ degrees

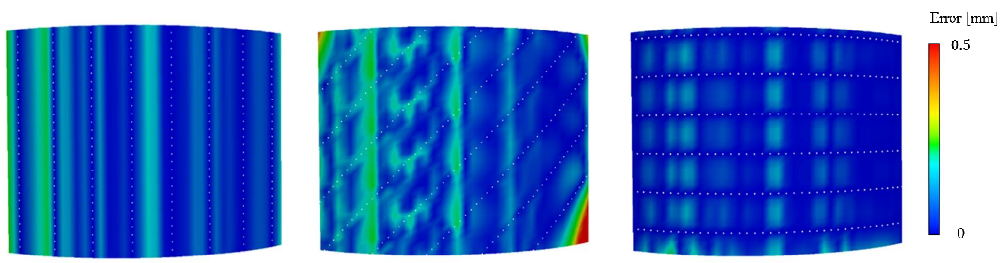

(d) TPS: $\theta = 0$ degrees (e) TPS: $\theta = 45$ degrees (f) TPS: $\theta = 90$ degrees

Figure 4-26 Error distribution at curvature 0.030 of texture direction 0 degrees, 45 degrees and 90 degrees

Figre 4-26 shows the registration error distribution of the proposed method and TPS based method in curvature 0.03 with texture angle 0, 45 and 90 degrees. In the proposed method, It can be seen that the error was almost kept unchanged. In the TPS based registration, it can be seen that the there were relatively large error especially at around the point which is far away from texture point, which is constant to Cao’s conclusion.

The registration accuracy of the proposed method with regard to different curvatures with different frequencies are shown in Figure 4-27. The registration accuracy of the TPS based registration with regard to different curvatures with different frequencies are shown in Figure 4-28.

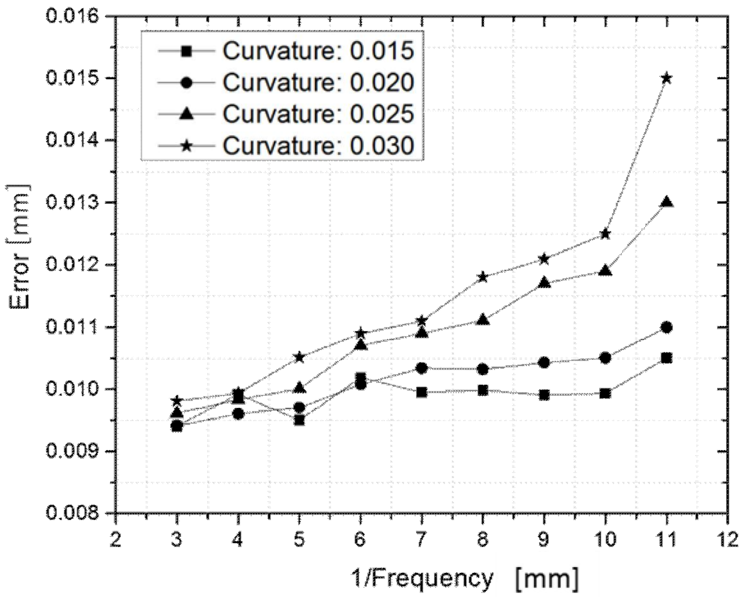

Figure 4-27 Registration error at different curvatures and texture frequencies of the proposed method

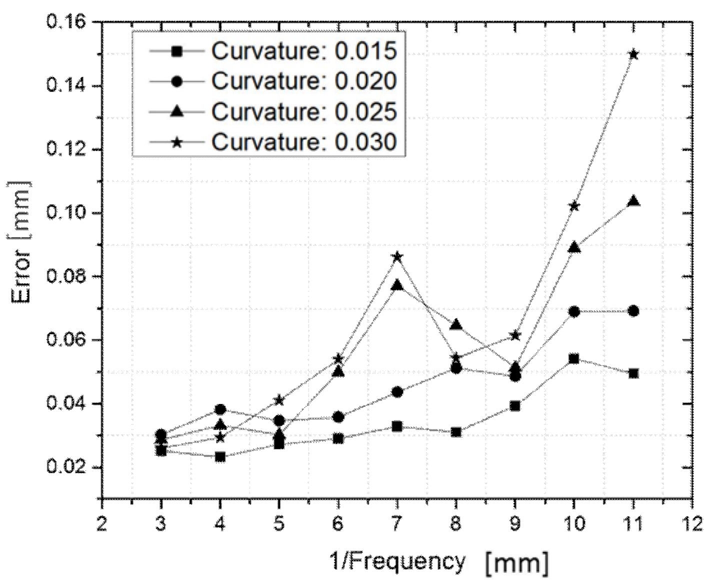

Figure 4-28 Registration error at different curvatures and texture frequencies of the TPS based registration

The result showed that for the proposed method, the registration accuracy was kept increasing with decrease of frequency. For curvature 0.015 and 0.02, which have less deformation magnitude, the gradient of registration error increasing was small. For curvature 0.025 and 0.035, when texture frequency is larger than 1/11, the gradient of registration error increasing was also small but when the texture frequency is less than 1/11, the registration error increased dramatically. As for different curvature, the registration error of the proposed method showed an increase tendency.

However, for the TPS based registration method, the error increased dramatically with the texture direction change, especially when the texture frequency is smaller than 1/9. As for the different curvatures, the TPS based registration error increased dramatically with increase of curvature.

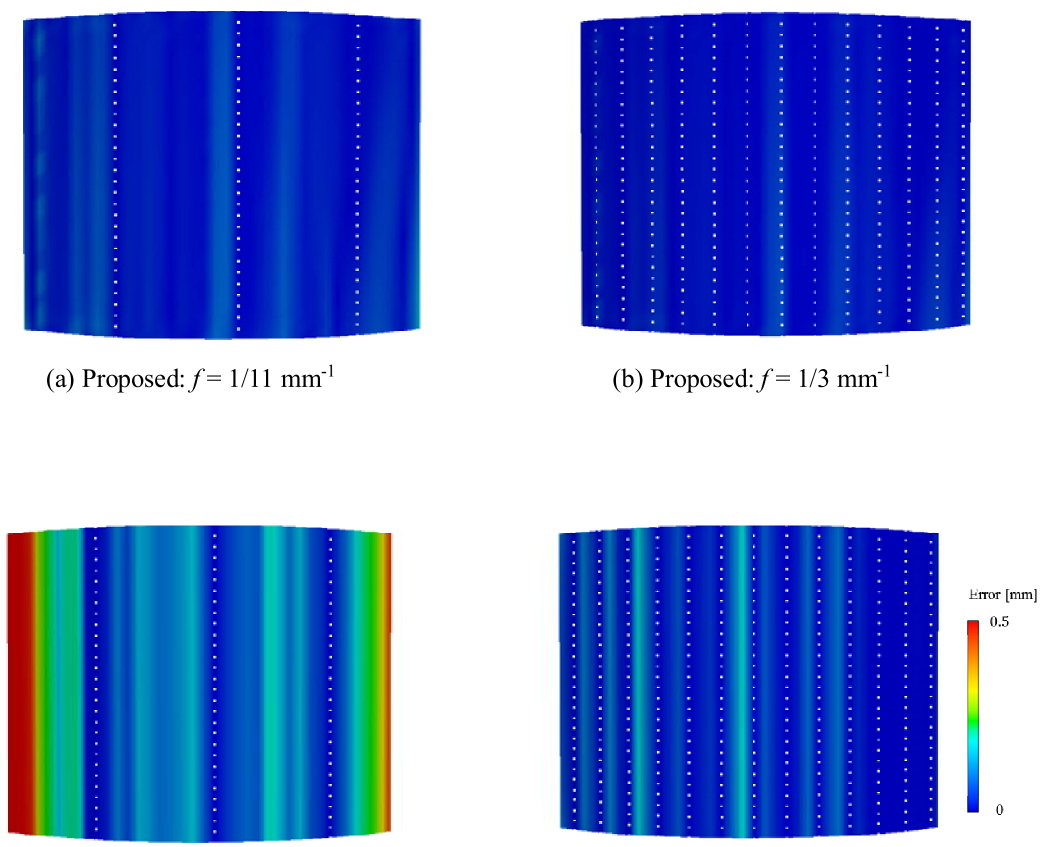

(a) Proposed: $f = 1/11\ \mathrm{mm}^{-1}$ (b) Proposed: $f = 1/3\ \mathrm{mm}^{-1}$

(c) TPS: $f = 1/11\ \mathrm{mm}^{-1}$ (d) TPS: $f = 1/3\ \mathrm{mm}^{-1}$

Figure 4-29 Error distribution at curvature 0.030 of texture frequency 1/11 and 1/3

To be specific, the registration error distribution of curvature 0.030 with frequency 1/11 and 1/3 are shown in Figure 4-29. In Figure 4-29, both the proposed method and TPS method aligned well. However, the TPS based method showed an increased error in some part of the surface. The Figure 4-29 (a) showed that the proposed method worked stable when texture frequency decreased. However, the TPS based registration method failed to register the surface especially in the boundary of the surface. The left part of the surface is far away from the texture and the TPS showed a low registration accuracy. However, the proposed method appears to be robust against the texture frequency change.

In conclusion, the simulation result of the proposed method was robust against texture frequency and deformation magnitudes change. However, the TPS based registration method was not robust to texture frequency and deformation magnitude variations.

The registration error against divergence deformation and shear deformation with different deformation magnitudes are shown in Figure 4-30 and Figure 4-31. The result showed that with the e_{xx}/e_{yy} or e_{xy}/e_{yx} increasing, the registration error was kept slightly increase, however, registration error still remained small in whole measurement range. The TPS registration error was also kept increase and held a larger error compared to the proposed method. The result showed that the proposed method is robust to divergence deformation.

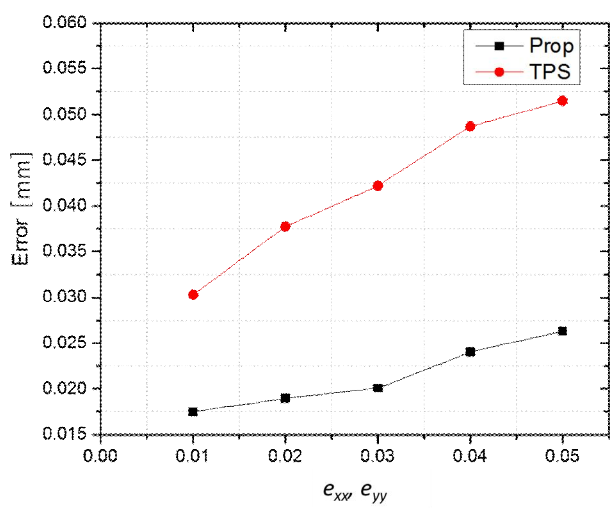

Figure 4-30 Divergence deformation

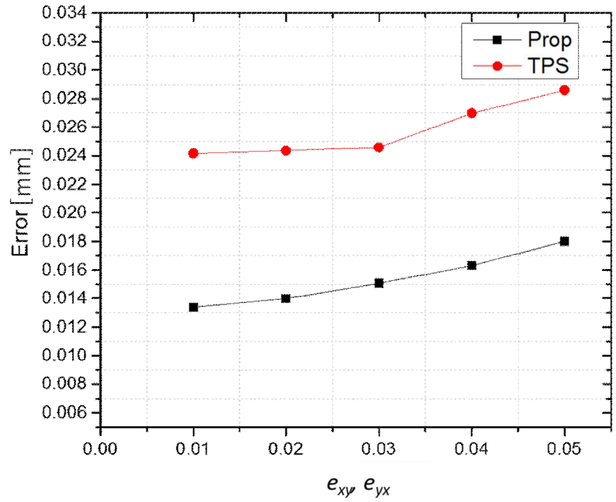

Figure 4-31 Shear deformation

To be specific, the error distribution of proposed method and TPS against divergence deformation at 0.01, 0.03 and 0.005 are shown in Figure 4-32. The result showed that the proposed method resulted in smaller error, and the error of TPS based registration distributed with disordered manner. Moreover, the error distribution of the proposed method and the TPS based registration against shear deformation at 0.01, 0.03, and 0. 05 are shown in Figure 4-33. The result also showed that the proposed method resulted in smaller error and the error of the TPS based registration distributed with disordered manner.

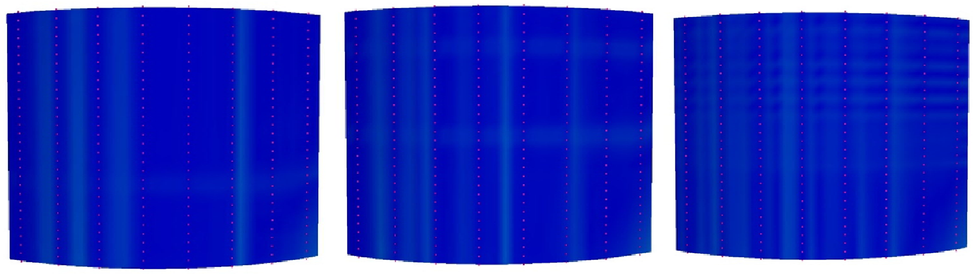

e_{xx}, e_{yy} = 0.01 e_{xx}, e_{yy} = 0.03 e_{xx}, e_{yy} = 0.05

(a) Proposed method

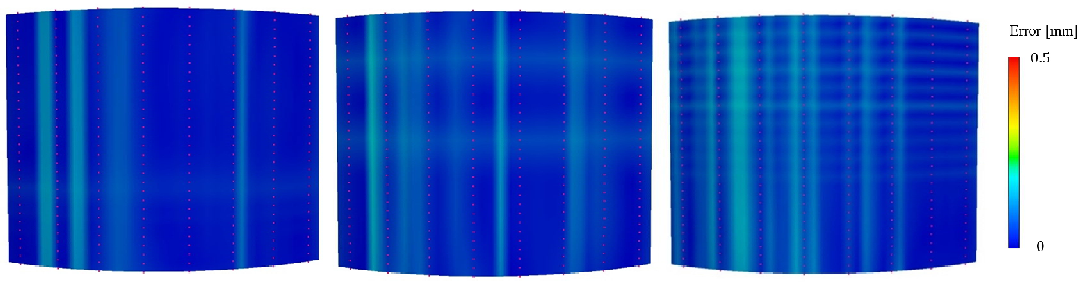

e_{xx}, e_{yy} = 0.01 e_{xx}, e_{yy} = 0.03 e_{xx}, e_{yy} = 0.05

(b) TPS

Figure 4-32 Divergence deformation against different strain of proposed method and TPS based registration

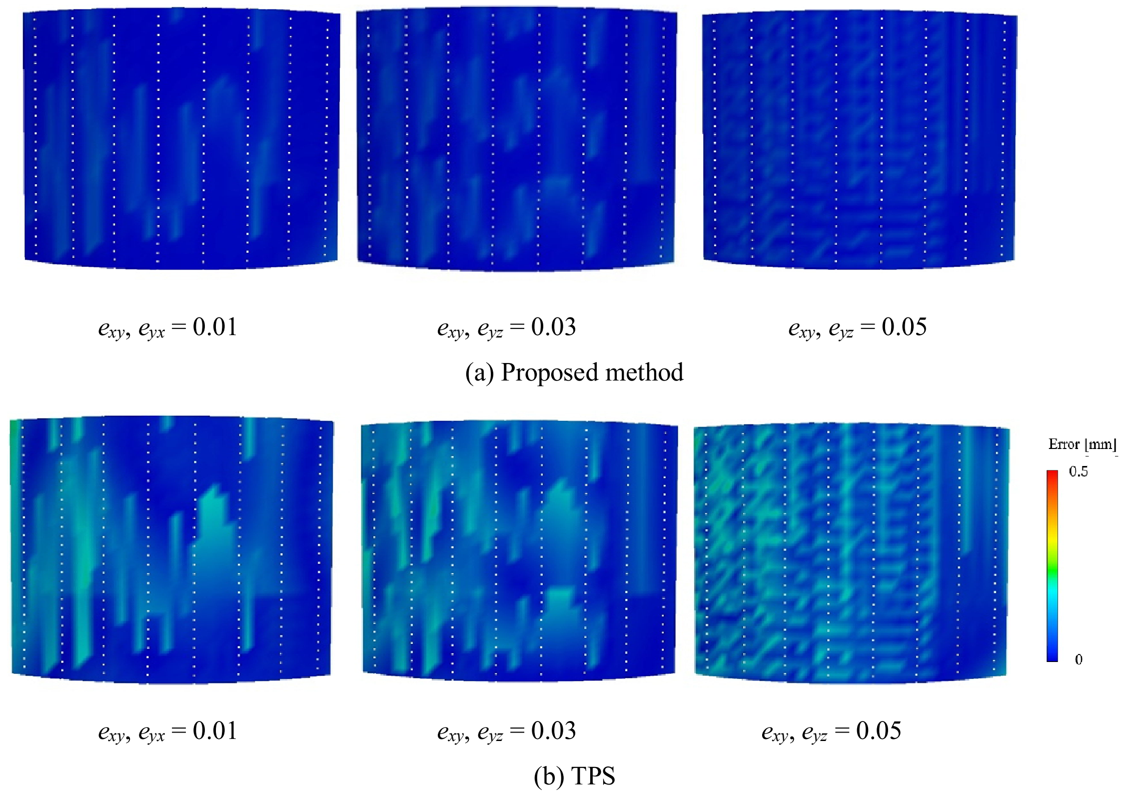

Figure 4-33 Shear deformation against different shear of proposed method and TPS based registration

4.3.3 Discussion

In this experiment, the simulated registration accuracy of a cylinderical shape was evaluated and the relation between the registration accuracy and the curvature, the texture frequency, texture direction, magnitude of divergence and shear deformation were evaluated. The registration results were compared with TPS method.

The result showed that when the texture frequency decreased, the proposed method worked stable compared with TPS based method. As noted, our non-rigid registration algorithm uses texture for registration. In the registration, texture will only find corresponding point from the texture space which will make the texture deform to texture space and surface deformed to the surface space. When texture number reduced, the TPS based registration will give worse registration result, since the TPS based registration is not robust to texture frequency change. As shown in Figure 4-29, the left part of the surface showed a misalignment with high registration error. The TPS method uses vessel for registration and the surface deformed by the TPS deformation transformation matrix calculated by the vessel registration. Accordingly, the vessel can align well, however, the surface points far away from the texture/vessel with large amount of deformation would cause a large error. Since TPS consider the deformation as a thin-plate deformation, the farer point from texture, the more rigid deformation it is. However, the proposed method uses all surface points including both the surface and texture for registration, and the smoothness and rigidness constraint are also introduced for registration. The Figure 4-28 showed an error increasing trendency of the proposed method. Such trendency is reasonable since if few points are considered as texture point, the proposed method would be a near non-rigid ICP method. Thus, it also showed one limitation of our method- registration accuracy relied on texture number (even not so much compared with TPS method). Fortunately, in the real brain surface, there is sufficient vessel information which can be used for registration.

As for the influence of texture direction, when the texture direction increased, the registration error reduced, which appeared in both the proposed method and the TPS based registration. This happened because of the cylinderical shape used in this experiment. For example, when the texture direction follows 0 degrees, from the texture, there is no deformation alone the texture; while when the texture direction increases, the texture can “cause” some deformation and this kind of texture deformation can be compensated by the texture. In the real brain surface, the vessel structure is very complicated, which could or could not follow the deformation of the shape deformation. The registration result showed that the proposed method worked robustly on this kind of situations, while the TPS based registration was sensitive to the texture direction variation.

The error distribution of the proposed method and TPS against divergence and shear deformation at 0.05 mm is shown in Figure 4-32 and Figure 4-33. Some regular pattern appears in the TPS result, since TPS method is an interpolation method. The denser texture around, the more interpolated the point get involved. The right below part of image, shown in Figure 4-33, has relatively simple texture corresponding and its interpolation is simple. Therefore, the registration result there is relatively stable (no pattern). On the contrary, the left and the middle part has complex texture corresponding, which lead a registration error pattern because the point position is interpolated by the texture point around.

All the experimental result revealed that the deformation magnitudes, texture frequency, texture direction, shear deformation and divergence deformation migh influence the registration accuracy. Thus, we need to evaluate the procine brain by considering such conditions.

4.4 Evaluation of Brain Surface Tracking

In this experiment, five porcine brains were used to evaluate the accuracy of the proposed method. Two kinds of experiments were conducted in this section. 1) Vertical displacement experiment; 2) Horizontal displacement experiment. The two experiments intend to evaluate the brain surface tracking accuracy in different deformations. Firstly, by pushing the porcine brain from the bottom in the vertical direction, the porcine brain experiences deformation under gravity (one source of brain shift in a clinical setting). This vertical deformation is important because in the brain surgery, the main brain deformation direction is in gravity direction and it is necessary to test the accuracy of the tracking in the direction of the vertical direction. Secondly, by pushing the porcine brain in the horizontal direction, the porcine brain experiences shrinking deformation by manual force.

4.4.1 Purpose

The purpose of this experiment is to test the tracking accuracy of the proposed method when the brain experiences different direction and magnitude of deformation.

4.4.2 Materials and Method

We evaluated the accuracy of the proposed method by using 5 porcine brains, and brain deformed in the vertical direction and horizontal direction. According to the previous researches, the brain shift mainly happens in gravity direction. Thus, we made the brain displaced and deform in the vertical direction. We also evaluated brain deformation in the horizontal direction by pushing a porcine brain in the horizontal direction because the brain can be deformed by manual pushing during the surgery.

a) Vertical displacement experiment set up

The vertical deformation experiment set up is shown in Figure 4-34 and Figure 4-35. The porcine brain was fixed on a rubber sheet with thickness of 0.5 mm, and supported by a screw placed under the rubber sheet. By rotating the screw, the vertical position of the brain was adjusted, thus the porcine brain could be deformed in a non-rigid manner. The displacements of the screw were 5, 10, 15, and 20 mm, corresponding to the average vertical displacement of the brain shift. In the vertical displacement experiments, the shapes before and after deformation were considered as the target and source shapes, respectively. The detail of the experimental conditions is described in Table 8.

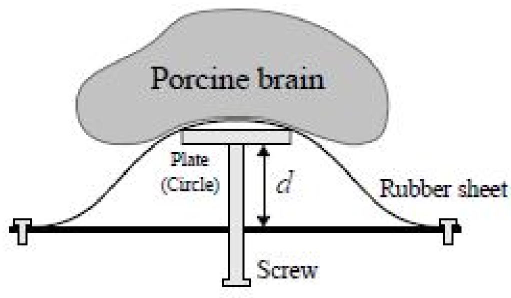

Figure 4-34 Schematic diagram of vertical displacement experiment set up

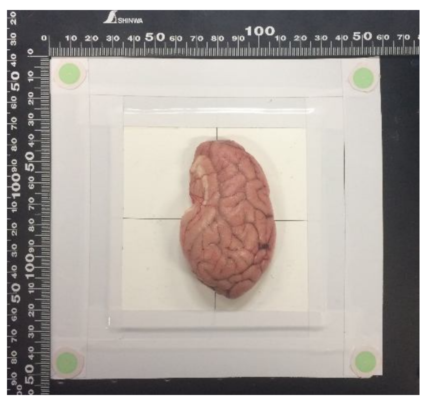

Figure 4-35 Experimental set up of vertical displacement experiment with a porcine brain

Table 8 Vertical disaplacement experiment

Object	5 Porcine Brains
Measurement distance [mm]	250
Projector Resolution [pixels]	848×480, 8 bit depth of each color
Camera Resolution [pixels]	512×512, 8 bit depth of intensity
Vertical displacement d [mm]	5, 10, 15, 20
Brain shift direction	Parallel with gravity direction
Measurement equipment	OPTOTRAK (Northern Digital Inc.)

b) Horizontal displacement experiment set up

The horizontal displacement experiment set up is shown in Figure 4-36 and Figure 4-37. The porcine brain was placed between two walls, one of which was fixed while the other could move in horizontal direction. By controlling the linear stage, the wall moved horizontally, thus the porcine brain was pushed, thereby inducing deformation. Displacement of the linear stage *d* were 5, 10, and 15 mm, as suggested in Figure 4-36. The detail parameters of horizontal experiment are listed in Table 9. Five porcine brains were evaluated.

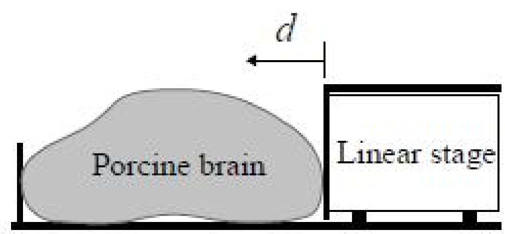

Figure 4-36 Schematic diagram of horizontal displacement experiment set up

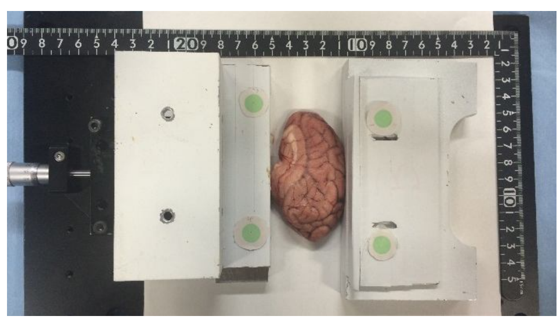

Figure 4-37 Horizontal displacement experiment set up with porcine brain

Table 9 Horizontal displacement experiment

Object	5 Porcine Brains
Measurement distance [mm]	250
Projector resolution [pixels]	848×480, 8 bit depth of each color
Camera resolution [pixels]	512×512, 8 bit depth of intensity
Horizontal displacement *d* [mm]	5, 10,15
Brain shift direction	Perpendicular with gravity direction
Measurement equipment	OPTOTRAK (Northern Digital Inc.)

c) Evaluation methods

1) Residual Error (RE)

Firstly, the proposed method was evaluated using Residue Error (RE), which was calculated using Equation 4-6.

$$\mathrm{RE} = \sqrt{\frac{\sum_{i=1}^{n} e_i^2}{n}} \tag{4-6}$$

where, e_i is the closest distance between the registered surface point and the target surface point; n is the total point number. RE reflects the proximity of two shapes to each other, and is widely utilized to evaluate the registration accuracy. However, the closer distance between the two surfaces does not necessarily mean the better registration since there exists some sliding error between the two surfaces. Accordingly, another evaluation criterion Target Registration Error (TRE) is also adapted.

2) Target Registration Error (TRE)

To evaluate the proposed method using TRE, 3 dimensional localizer OPTOTRAK was used to calculate TRE. The tracked feature point position was compared with the point position measured from OPTOTORAK. Appearance of OPTOTRAK stylus and the procedure for measuring the point is shown in Figure 4-38.

(a) Measuring procedure

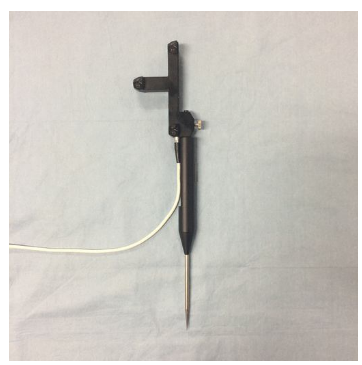

(b) The stylus of OPTOTRAK

Figure 4-38 Feature point measuring by OPTOTRAK

We divided the error along the surface and vertical to the surface to see how much the error contribution of the texture and surface is. The error along the surface will show the texture error while the error vertical to the surface will show the surface error.

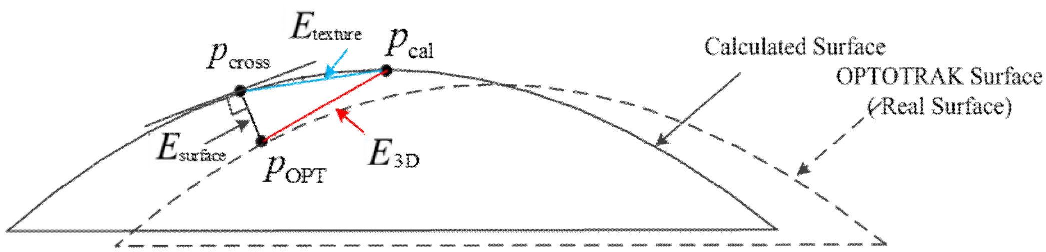

Figure 4-39 Tracking error calculation

As shown in Figure 4-39 p_{OPT} is the point measured point position by OPTOTRAK; p_{cross} is the perpendicularly projected point position of p_{OPT} onto the deformed surface; p_{cal} is the calculated point position by using our method. The error calculation could be expressed as:

$$\begin{aligned} E_{3D} &= \| p_{\text{OPT}} - p_{\text{cal}} \| \\ E_{\text{surface}} &= \| p_{\text{cross}} - p_{\text{OPT}} \| \\ E_{\text{texture}} &= \| p_{\text{cal}} - p_{\text{cross}} \| \end{aligned} \tag{4-7}$$

In equation 4-7, E_{3D} represented the real registration error in the 3D space; E_{surface} showed the error vertical to the surface and the misalignment of the two surface (the error of the surface fitting); E_{texture} showed the error along the surface (the error of the texture sliding).

4.4.3 Result

4.3.3.1 Vertical displacement experiment

1) RE

a) Quantitative Result

The registration surface RE error and texture RE error are shown in Figure 4-40 and Figure 4-41, respectively. Our registration results were compared with ICP method, Non-rigid ICP method and TPS based registration method (Cao *et al.*). The difference between the three methods and the proposed method is shown in Table 10. ICP method only uses shape for registration with a rigid transformation assumption. The nonrigid-ICP method use only shape for registration with smoothness and rigidness constraint. The TPS based method uses texture as control point to generate a deformation field while the shape is deformed interpolation. The proposed method uses both shape and texture for registration and uses a smoothness and a rigidness constraint for interpolation. From the quantitative result, it was shown that ICP method could cause the largest error, and as the deformation magnitude increased, the registration error was kept increasing. The surface RE of the Non-rigid ICP method was smaller, but it caused a large texture error, shown in Figure 4-41. The TPS based registration method had less texture registration error, but had a larger surface registration error. The proposed method could achieve less surface registration error and less texture registration error.

Table 10 Differentces between ICP, nonrigid-ICP, TPS and the proposed method

	$E_{surface}$	$E_{texture}$	E_{smooth}	E_{rigid}
ICP	✓	N/A	N/A	✓
Nonrigid-ICP	✓	N/A	✓	✓
TPS	N/A	✓	✓	N/A
Proposed	✓	✓	✓	✓

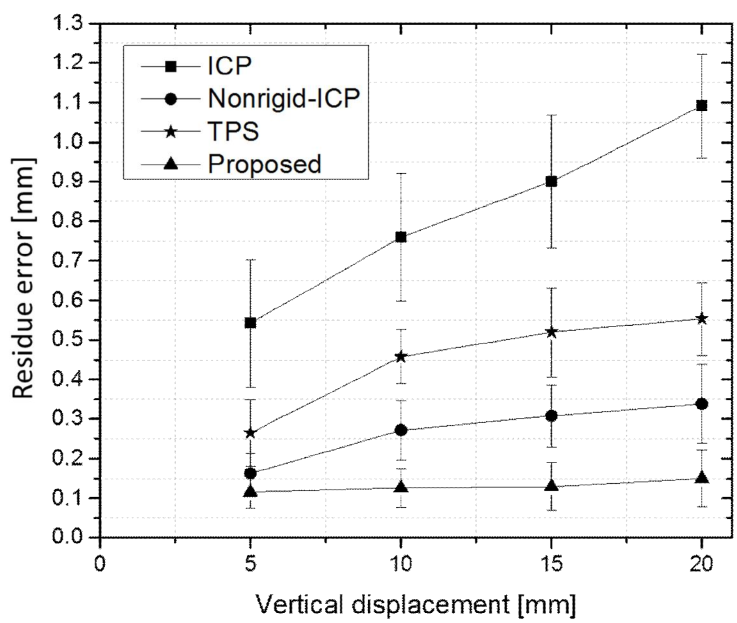

Figure 4-40 Registration surface RE of ICP, Nonrigid ICP, TPS based and the proposed method

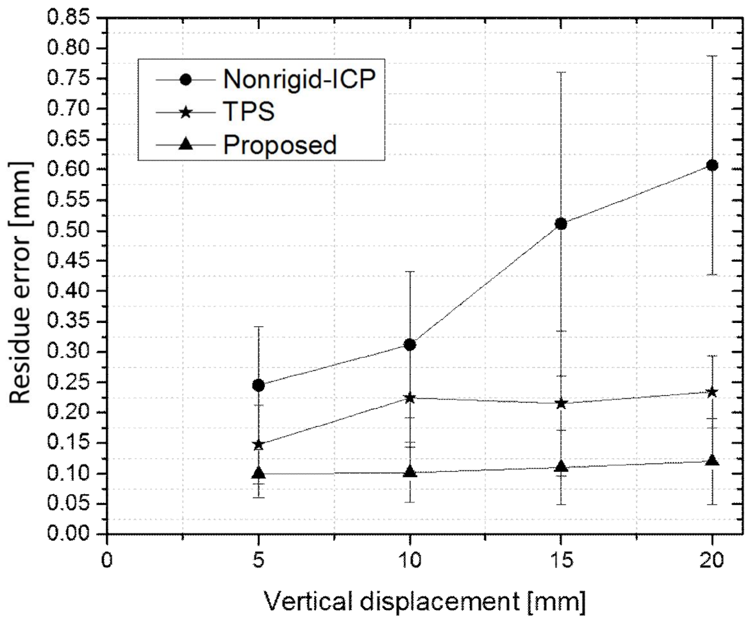

Figure 4-41 Registration texture RE of ICP, Nonrigid ICP, TPS based and the proposed method

b) Qualitative Result

The qualitative registration result is shown in Figure 4-42 and the registration surface fitting error distribution is shown in Figure 4-43. The texture alignment of the non-rigid ICP method and the proposed method are shown in Figure 4-44. Green line is the target texture; red line is the proposed registration texture and blue line is the non-rigid-ICP registration method.

From the result, it was shown that ICP failed to compensate the shape deformation, as suggested by the ICP result of Figure 4-43. The TPS based method could achieve a better result but at the boundary of the shape, it failed to align well. The non-rigid-ICP could obtain good registration from the surface, but it would bring the sliding error, suggested by Figure 4-44. However, the proposed method had a good surface alignment and texture alignment.

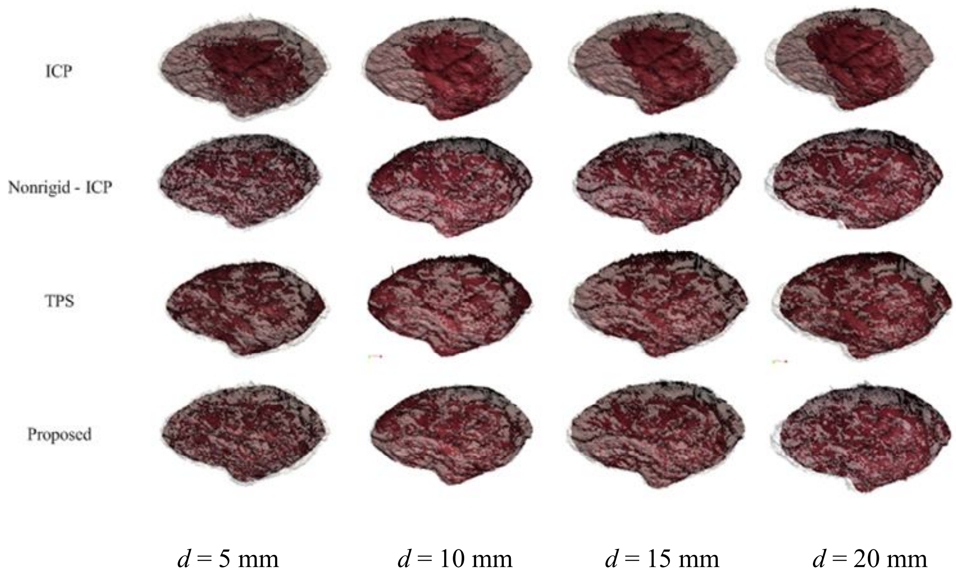

Figure 4-42 Registration result at different vertical displacements of ICP, Nonrigid ICP, TPS based and the proposed method

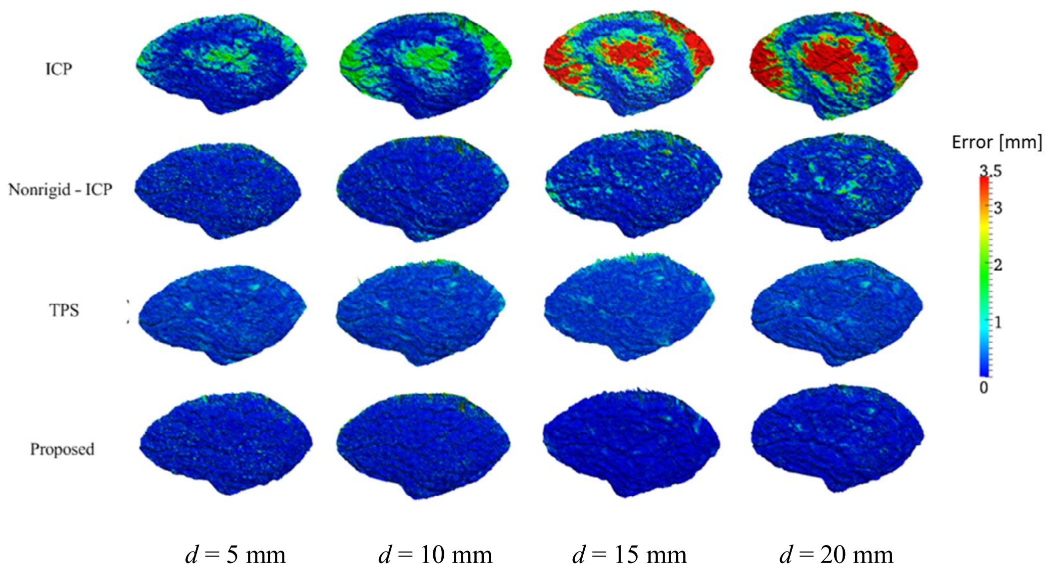

Figure 4-43 Vertical registration error distribution of ICP, Nonrigid ICP, TPS based and the proposed method

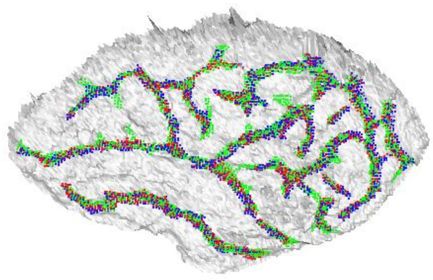

(a) d = 5 mm

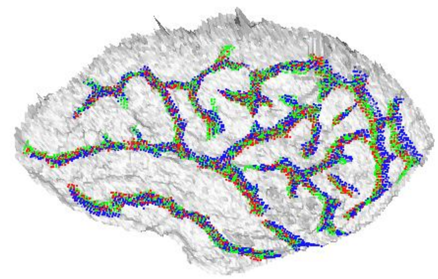

(b) d = 10 mm

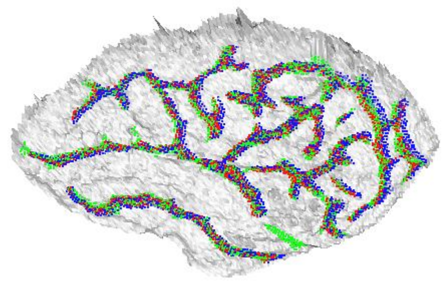

(c) d = 15 mm

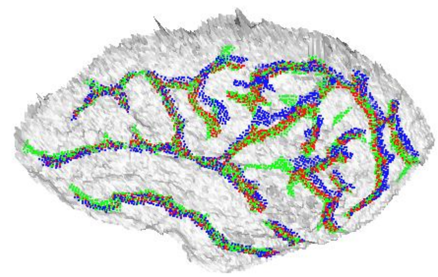

(d) d = 20 mm

Figure 4-44 Texture alignment comparison (green: target texture, red: proposed method, blue: non-rigid-ICP method)

One of the calculated deformation fields is shown in Figure 4-45 (a) and Figure 4-45 (b). The deformation field agreed with the result of vertical displacement experiment. In the boundary, it deformed largely while in the middle range, it deformed smaller, which was also consistent with the ICP alignment result (Figure 4-43).

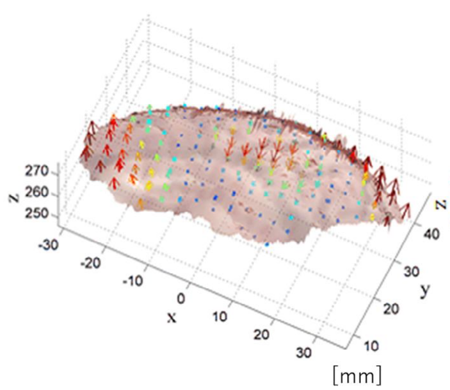

(a) Brain with 3D deformation field

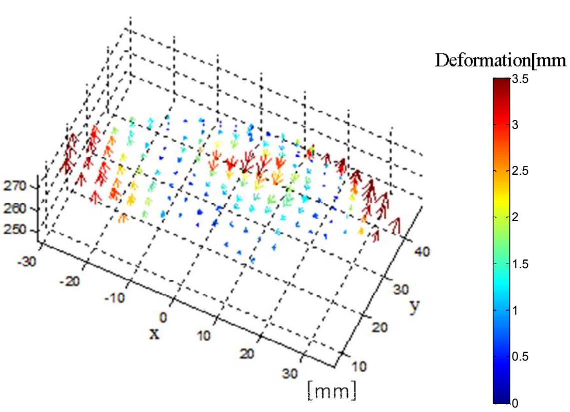

(b) 3D deformation field

Figure 4-45 Deformation field of one porcine brain at 25 mm vertical displacement

2) TRE

a) Quantitative Result

To evaluate TRE, the proposed method was compared with ICP and non-rigid-ICP method. ICP assumes a rigid transformation and non-rigid-ICP only considers the surface information (without texture information) for registration. The quantitative result evaluated using 5 porcine brains is shown in Figure 4-46. It is shown that the tracking error of the proposed method by combing texture was smaller than both ICP method and non-rigid ICP method. The error of the proposed method remained stable when the displacement increased while that of the non-rigid-ICP was kept increasing.

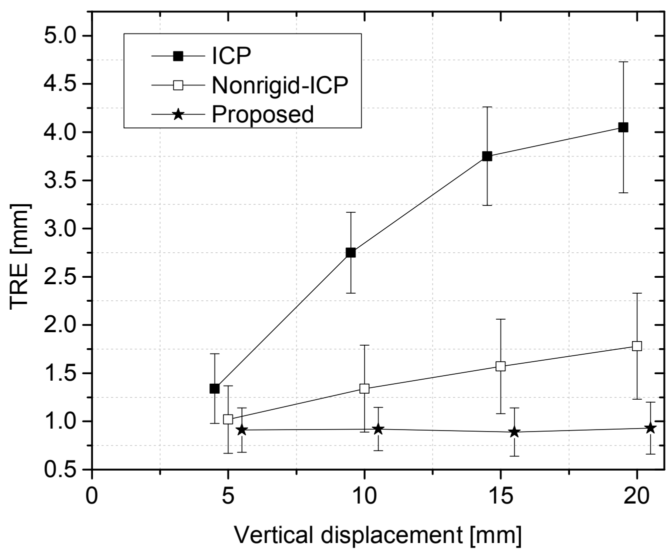

Figure 4-46 TRE with respect to different displacements of ICP, Nonrigid ICP and the proposed method

The result of $E_{surface}$ and $E_{texutre}$ for the 5 porcine brains are shown in Figure 4-47. The horizontal axis showed the different displacements (5, 10, 15 and 20 mm during the vertical displacement experiment). The vertical axis shows the error of $E_{surface}$ and $E_{texture}$ of the proposed method and non-rigid-ICP method. The result showed that with the displacement increasing, the $E_{surface}$ and $E_{texutre}$ of non-rigid-ICP increased and more texture sliding error was caused. However, the $E_{surface}$ and $E_{texutre}$ of the proposed method were stable and it reduced the surface sliding error of non-rigid ICP method which only considers the surface for registration. The proposed method can enhace the registration error 1 mm on average at displacement 20 mm compared with non-rigid-ICP method.

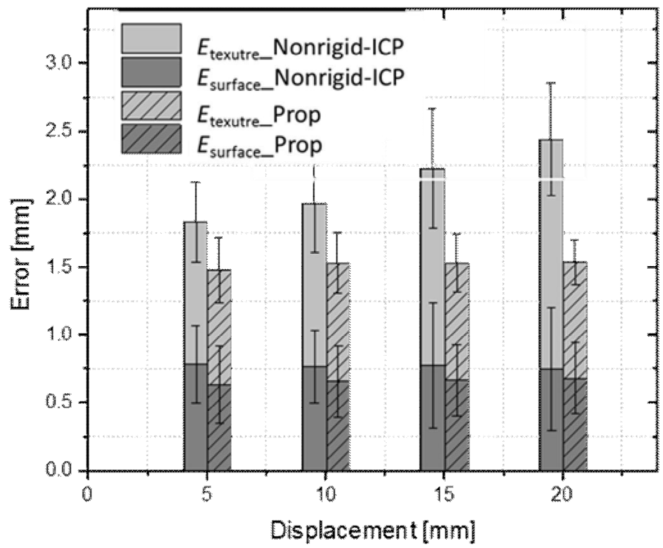

Figure 4-47 E_{surface} and E_{texture} of five porcine brains at different displacements

b) Qualitative Result

The TRE error distribution of the feature points of one porcine brain is shown in Figure 4-48. In Figure 4-48, (a), (b) and (c) show the TRE distribution after registration of ICP, non-rigid-ICP and the proposed method, and different rows show the different displacement. Different method means different error with red the largest error and the blue smallest error.

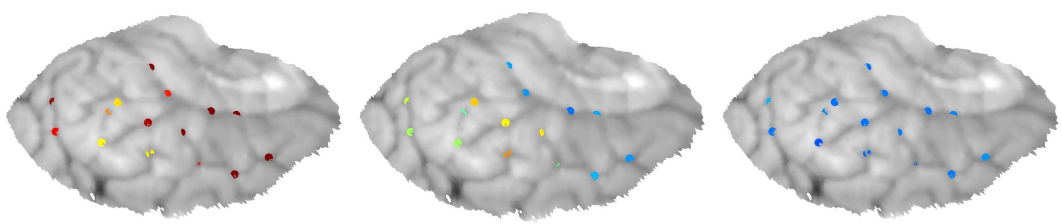

(a) (b) (c)

Figure 4-48 TRE error of one porcine brain (a) ICP result (b) non-rigid-ICP result (c) proposed

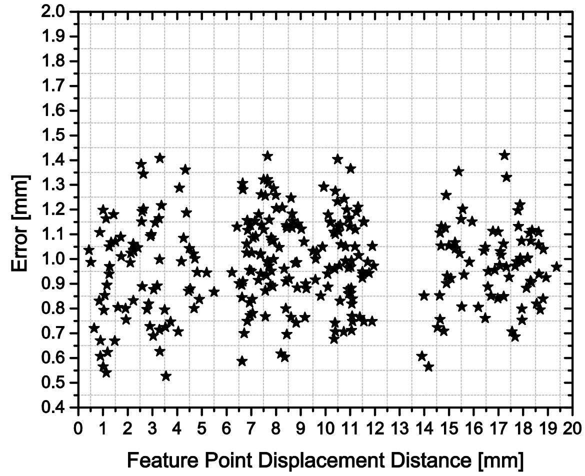

Figure 4-49 Tracking correlation coefficient

Figure 4-49 shows the correlation coefficient of the tracking error and distance change, r = 0.0862. The related smaller r showed the robustness of the proposed method to brain shift displacement.

4.3.3.2 Horizontal displacement experiment

1) RE

a) Quantitative evaluation

The registration RE quantitative result of the horizontal experiment is shown in Figure 4-50. While the texture alignment RE is shown in Figure 4-51. The RE results were also compared with ICP, non-rigid-ICP and TPS method. It showed that by using ICP, the initial alignment had some deformation error. Also, the registration RE error increased when pushing distance increased. From the result it is shown that the RE of the proposed method was below 0.01 mm and smaller than non-ICP. Figure 4-51 showed that when the pushing distance increased, the texture alignment of the proposed method was stable while non-ICP texture alignment increased.

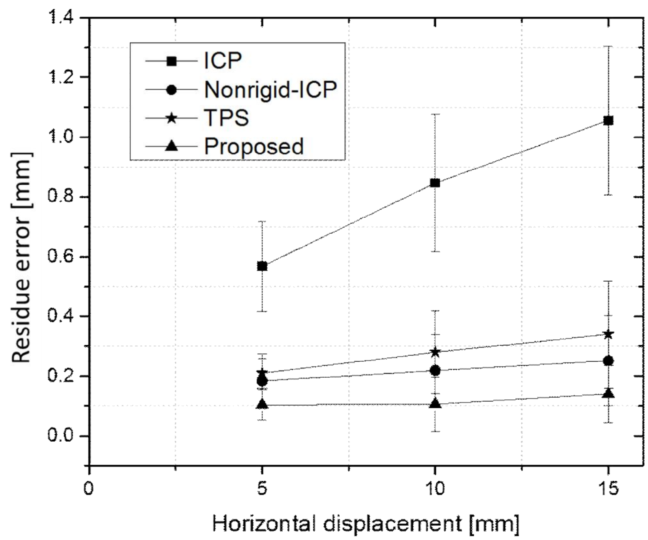

Figure 4-50 Horizontal registration surface RE error of ICP, Nonrigid ICP, TPS and the proposed method

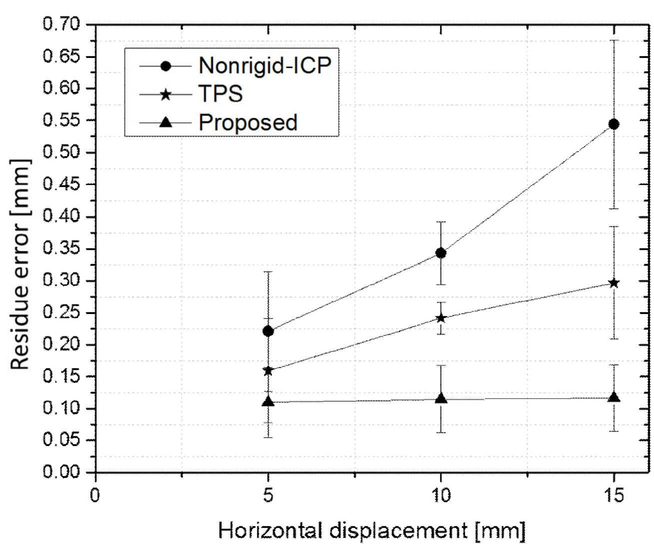

Figure 4-51 RE of Texture alignment at different displacements of Nonrigid ICP and the proposed method

b) Qualitative result

One brain surface alignment result of ICP, non-rigid-ICP, TPS and the proposed method are shown in Figure 4-52 and their surface fitting error distribution is shown in Figure 4-53. Their texture alignment result is shown in Figure 4-54.

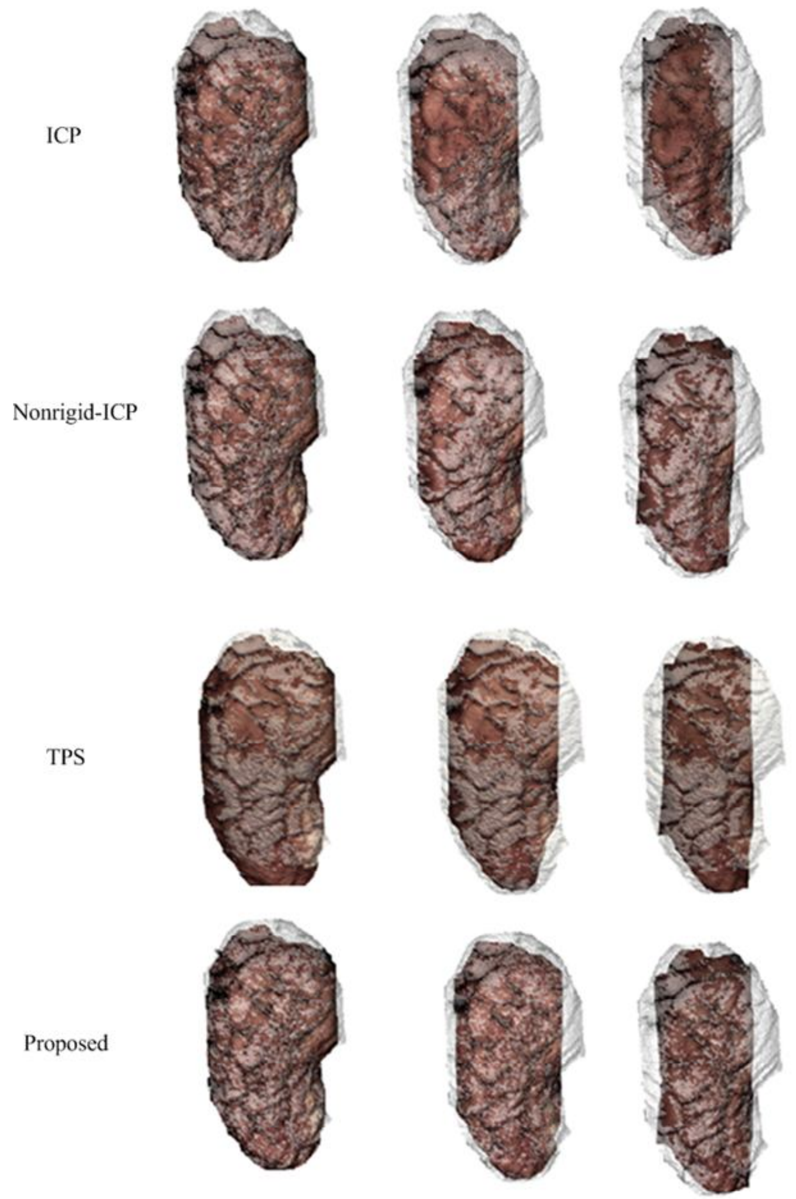

(a) d = 5 mm (b) d = 10 mm (c) d = 15 mm

Figure 4-52 Registration result of ICP, Non-rigid-ICP, proposed 5 mm, 10 mm and 15 mm displacement

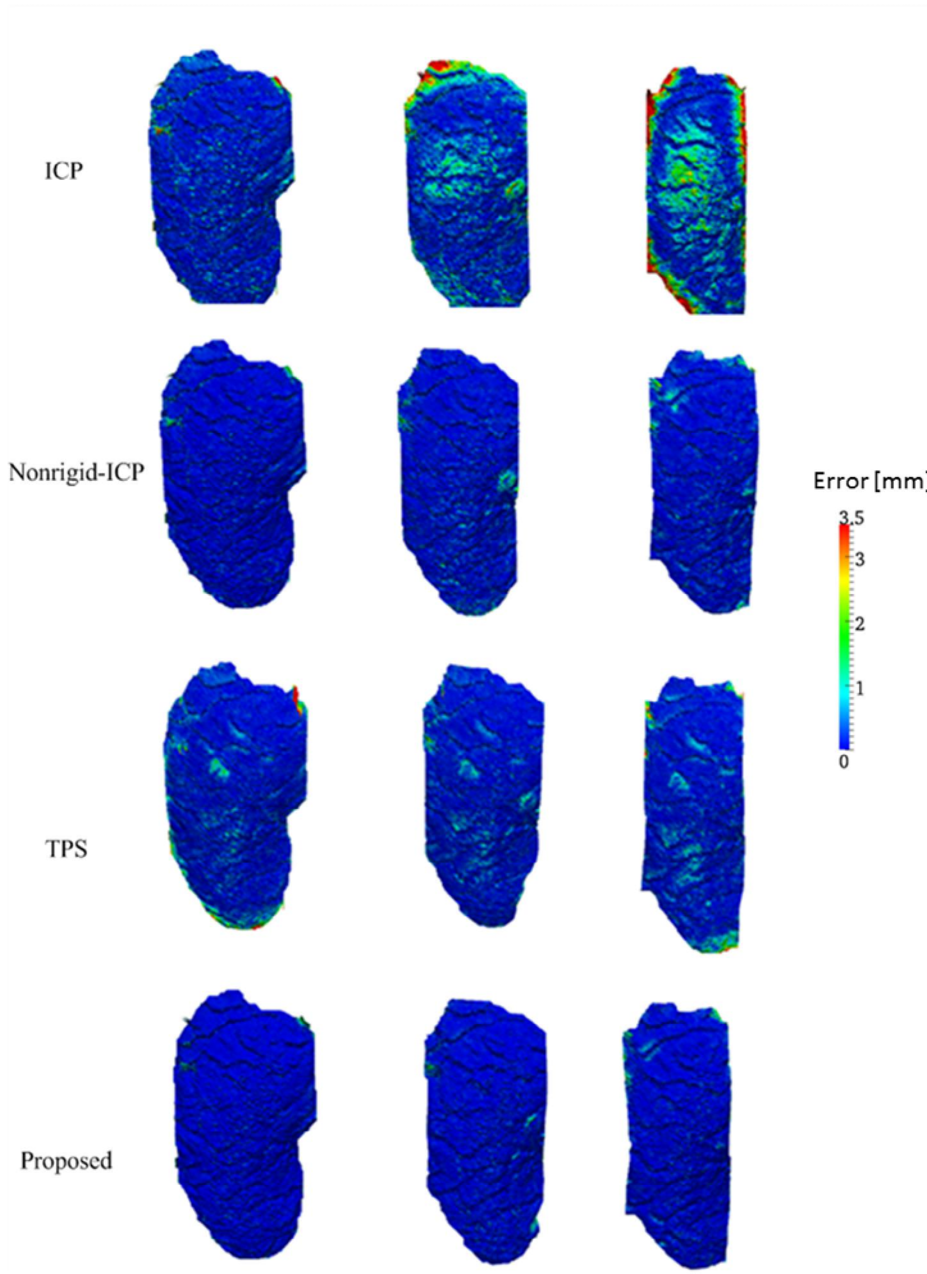

(a) d = 5 mm (b) d = 10 mm (c) d = 15 mm

Figure 4-53 Horizontal RE distribution at 5 mm, 10 mm and 15 mm displacement

From the result, the ICP result showed that it failed to compensate the brain surface deformation especially in 10 mm and 15 mm displacement. At the boundary area of brain surface, the alignment error was larger. For the non-rigid ICP method, it could achieve a good surface alignment with smaller RE, however, it caused large texture-sliding error along the surface, suggested in Figure 4-54. In Figure 4-54 green line is the target texture; red line is the proposed texture alignment while blue line is the non-rigid-ICP registration result. It was shown that in displacement 10-mm and 15-mm, the non-rigid-ICP caused a sliding alignment error even they had a smaller surface alignment error.

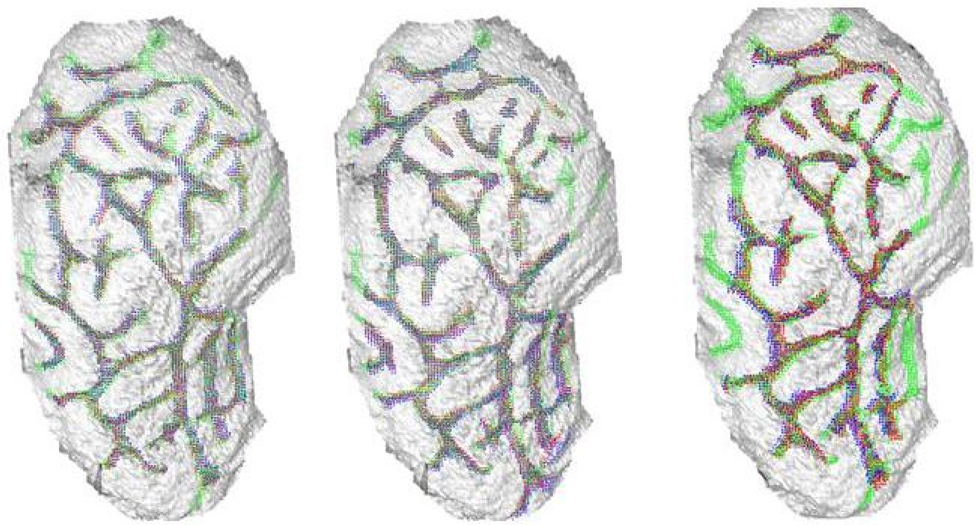

(a) d = 5 mm (b) d = 10 mm (c) d = 15 mm

Figure 4-54 Horizontal texture alignment result. Green line is the target texture, red line is the proposed texture alignment while blue line is the non-rigid-ICP registration result.

2) TRE

a) Quantitative Result

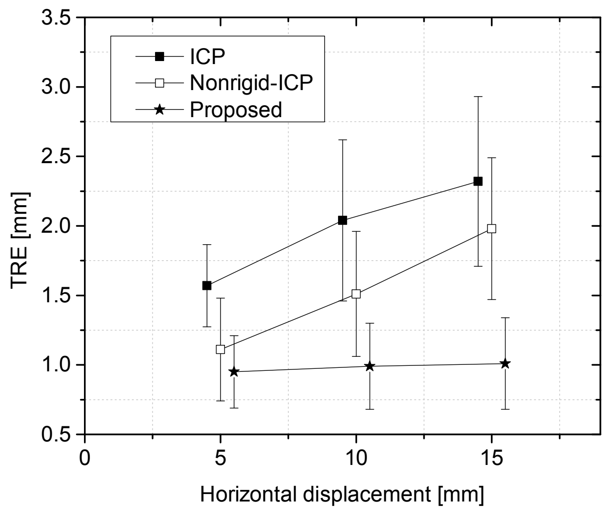

Figure 4-55 TRE of horizontal experiment at different displacements of ICP, Nonrigid ICP and the proposed method

The TRE quantitative result is shown in Figure 4-55. ICP, and non-rigid-ICP were compared to the proposed method. From the result, it was shown that the TRE of ICP was kept increasing when displacement increased. And the TRE of the non-rigid ICP also increased when distance increased.

The detail of E_{surface} and E_{texture} for the 5 porcine brains are shown in Figure 4-56. The horizontal axis shows the 3 different displacements (5, 10, and 15 mm) and the vertical axis shows the E_{surface} and E_{texture} of the proposed method and the non-rigid-ICP method. The result showed that for both the proposed method and the non-rigid-ICP method, the E_{surface} was smaller. However, the non-rigid-ICP method caused a large surface sliding error shown as E_{texture} in Figure 4-54.

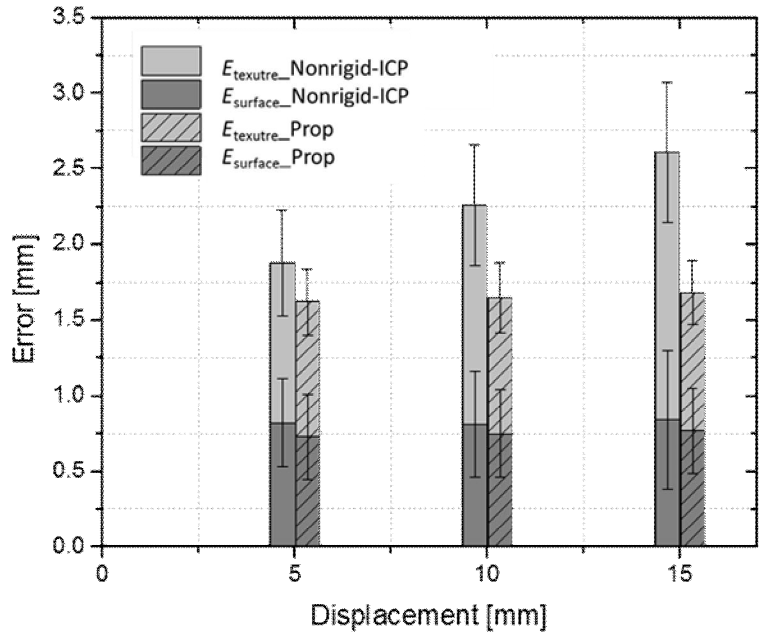

Figure 4-56 E_{surface} and E_{texture} in horizontal experiment at different displacements

(b) Qualitative Result

One porcine brain deformation field is shown in Figure 4-57. It was shown that the near the pushing area would bring large deformation while the other area was smaller. The TRE distribution is shown in Figure 4-58. (a), (b) and (c) show the TRE distribution of ICP, Non-rigid-ICP, and the proposed method. The result showed that ICP would result in higher error even in the horizontal pushing experiment, the deformation was smaller. The non-rigid ICP resulted in higher TRE.

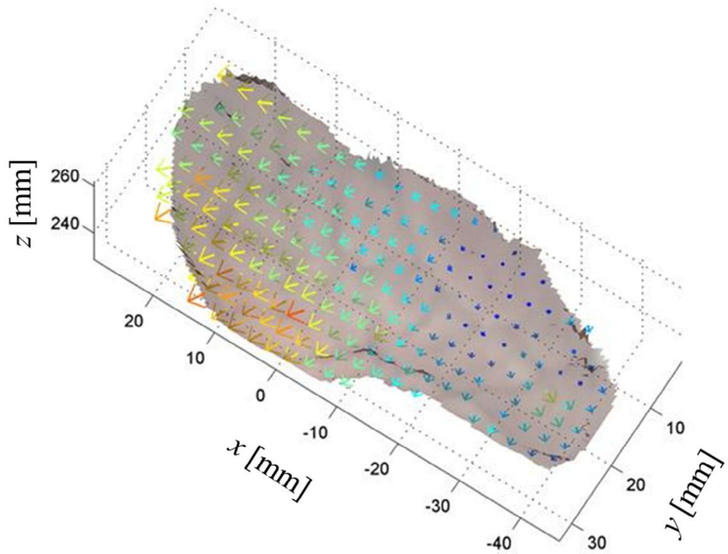

Figure 4-57 One brain deformation field of horizontal displacement

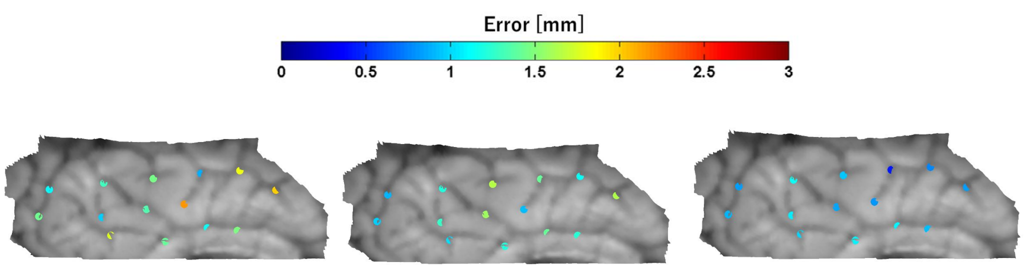

(a) ICP (b) non-rigid-ICP (c) Proposed

Figure 4-58 TRE of ICP, non-rigid-ICP and proposed method of one porcine brain

4.4.4 Discussion

The proposed method integrated 3D texture and 3D surface points. Recently, Ji *et al.* used optical flow to track brain surface in the assumption that the intensity of brain surface did not change[90]. Their result depends on the intensity consistency of the 2D image. Also, other previous studies employed brain surface texture either in 2D or in 3D. Their approaches are obtaining the texture points corresponding and deform shape by Thin-Plate-Spline [104, 114-116]. It might have the large error when in the surface with less texture. TPS is a linear interpolation method and the surface point deformation are greatly influenced by the condition of texture points such as position and number.

In the proposed method, we implemented smoothness and rigidness constraint to deform all the points. The deformation between surface and texture are relatively independent. The smoothness constraint can generate a smooth deformation and rigidness constraint can keep the local detail information by constraining the transformation matrix to be a rotation matrix. The proposed method can register surface and texture simultaneously; also texture works as a skeleton in the registration. RE and Target Registration Error (TRE) were evaluated to quantitatively evaluate the result. Two kinds of deformation were generated in the exapriments: one in vertical direction and other in horizontal direction. The figure 4-52 and 4-53 showed that the ICP method would generate registration error on the boundary part since no non-rigid deformation was considered. The ICP method works when brain deformation magnitude was small, as Sun *et. al* has done. The TPS reigtration use vessel/sulci on the brain surface as control point and this method would lead error occurred where less control point presented. Our implemented TPS registration result do show large error at the boundary(less texture) (shown in Figure 4-53) which is consitant with TPS disadvantage. The non-rigid ICP method generated texture sliding error as shown in Figure 4-54 since only using shpe point can not compensate the horizontal residue. The proposed method combined shape and texture for registration and generated acceptable results. During registration, α = 10 and the ratio between shape points an texture points is 4.2:1. Therefore the α value assigned might be a reasonable value for registration. Further investigation of the ratio between shape points and texture points of all the tested porcine brains showed a value of 4.51. The result of evaluation of brains in the Figure 4-40, Figure 4-41, Figure 4-50 and Figure 4-51 further prove the the assigned α value 10 is acceptable.

Figure 4-47 and Figure 4-56 clearly showed the advantage of the proposed method compared to nonrigid ICP method. For example, in Figure 4-56, when the displacement increased from 5 mm to 15 mm, the E_{surface} of both proposed method and nonrigid ICP keep almost same error, which might be the limitation of the surface alignment of both methods. However, a clearly decreased E_{texture} is shown. The reduced texture error is up to 49% of the error in nonrigid ICP method at 15 mm displacement experiment. Moreover, in the horizontal experiment, especially in 15-mm displacement experiment, some parts of the brain surface are missing because of pushing, as shown in Figure 4-52. In this circumstance, the texture point can work as deformable skeleton to guide registration.

The bifurcation points on porcine surface were used to evaluate the TRE. TRE can be influenced by several factors, such as manual point picking error, OPTPTRAK measuring error, registration error of OPTOTRAK system and 3D measurement system. In order to evaluate our non-rigid registration algorithm, we chose the distance of 250 mm in the experiment as in 250 mm the system has the highest 3D measurement performance. The TRE of the proposed method was 0.93 on average, which meets the requirement of the clinical application (2 mm).

We divided the TRE into E_{surface} and E_{texture} in order to further investigate the error contribution from texture (along brain surface) and shape (vertical to surface), as shown in Figure 4-47 and Figure 4-56. Both results showed that the proposed method can reduce the error along brain surface. The amount of reduced error might be influced by the coefficient α (in Equation 3-2) since if $\alpha = 0$, the proposed method become a nonrigid ICP method. However, it does not necessarily mean larger α would reduce more error along surface. As the Figure 4-6 showed, the texture error decreased as α increase and the error keep stable in a range. When increased α exceeds this range, the texture alignment error will increase. The registration result in Figure 4-47 and Figure 4-56 showed that the balance between E_{shape} and E_{texture}, we assigned, is acceptable.

The brain surface is smooth and there is sufficient texture information on the brain surface. Since the surface points construct a smooth surface, if only using surface, it could cause the sliding errors along the brain surface. However, by combining the surface and texture information, the surface sliding error can be reduced. The proposed method takes the advantages of texture for registration. The proposed method registered surface and feature simultaneously. Accordingly, good registration was obtained for surface points both near and far from feature points. In addition, we did not make a large number of comparisons because Cao[104] compared brain surface tracking in an objective manner with different registration methods, and observed that methods were performed differently according to the patient and the particular clinical case.

Clinical brain surfaces are complex and segmentation of surface vessels is challenging. Ding *et al.* proposed an automatic brain surface vessel segmentation by applying a Frangi filter and evaluated their method using clinical data[100, 101]. They reported that in a clinical situation, only large vessels, such as tube-like structures, were used for registration because it was difficult to establish a correspondence between small vessels[100, 101]. Furthermore, the brain surface may be incomplete during deformation. Eventhough the edge part of the shape is missing (such as occlusion), horizontal displacement experiments showed that the proposed method performed well in this type of incomplete situation. In another case, if the missing part of the shape is located in the middle of the shape (not the edge), in forms such as a hole, some manual ROI (Region Of Interest) selection or surface interpolation for filling in the incomplete surface might be needed. Therefore, further evaluation using clinical data is required in the future work. Our current 3D shape measurement system is limited to a single camera viewpoint, and with the multiple synchronizations of cameras and projectors, it is possible to acquire more accurate brain surface from different angles.

As all the 3D points are involved for calculation and the non-linear square least problem takes long time, the calculation time is long in the proposed method. However, the computing speed can be enhanced by using CUDA calculation.

5 Discussion

Proposed method applies a phase shift method to project patterns onto the patient's brain surface for the 3D shape measurement. The projector can also be used to project some brain surface information such as brain function area onto the patient's brain. By doing this, the surgeon can directly recognize the visualized brain function area instead of monitoring the screen. The projecting accuracy might be influenced by the projection distance, since our projector has large distortion and the distortion increases as the distance increases. Thus, a suitable projection distance is needed during the application, such as 250 mm far from the brain surface.

Besides, the proposed method still remained some limitations, drawbacks. They will be introduced below in Table 11 as well as the feasibility to apply the proposed method to clinic.

Table 11 Limitation of the proposed method

		$E_{cor\_surface}$	$E_{cor\_texture}$	E_{smooth}	E_{rigid}	Affected
Brain conditions (on each of position, shape, texture and hardness)	Position (distance from the device)	×	×			✓*2
	Size					Not affected
	Large deformation	×	*1			Not affected
	Small deformation					Not affected
	Shape smoothness	×	*1			Not affected
	Shape complexity					Not affected
	Texture-less		×	*1		✓
	Texture complexity		×	*1		✓*3
	Texture color					Not affected
	Diseased (material hardness)				×	✓*3
Lighting conditions	Illumination power	×	×			✓
	Ray color					Not affected
	Addition of other light sources					✓*3
Obstacles	Occlusion by hand and tools	×	×			✓

*1 This constraint compensates the drawbacks affecting another constraint
*2 Discussed in the thesis with experiments
*3 No soluton found by us

(The top row shows four constraints of the proposed method.) The right column shows our summarization if the proposed method can be affected by the conditions at the left side. The body at center shows possibility if each constraint can be affected by the issues shown at the left side. The left column shows influences, which we should consider. "×" means the energy component is influenced; "✓" means this specific parameter can influence the performance of our system; blank means not applicable. The table shows that our system was influenced by the hardware position, target conditions, and optical measurements. (Target conditions includes patient brain diseased (change in hardness), brain deformation, texture and shape conditions. On environmental conditions, lighting conditions and obstacles are chosen because our system employs optical measurement which can be mainly affected by illumination.) Discussing on how to overcome above effects, some solutions can be proposed: illumination power change can be avoided by introducing infra-red light source since infra-red-light component is cut off in operation rooms; texture-less problem can be also solved by infra-red light source because infra-red light is absorbed by hemoglobins in blood thus it is adequate to highlight vessels; and the obstacles caused by hands or surgical tools can be overcome by using graph-cut based segmentation methods. Regarding the issues marked with *3, texture complexity would not occur so frequently; material hardness would be acquired in the future but not at the present; addition of other light sources depends on each case and it is difficult to summarize it here.

Moreover, our system can be used into brain tumor resection surgery. One of commonly used methods is finite-element model (FEM). (A generally used FEM is a linear elastic model which can treat brain tissues with homogeneous linear elastic continuum.) One of the requirements to apply FEM is mathematical model describing material inner condition such as hardness. The other is boundary conditions. Regarding the model, we can employ homogeneous elastic model which is a kind of spring-damper connection models. The finite-element mesh is usually generated from a patient-specific pre-operative MR images. On the other hands, closing of boundary condition is required to achieve high accuracy as shown in Figure 5-1. The boundary condition of the top brain surface can be obtained by the proposed method. The other boundary part, which is the inner sculpture and cannot be obtained by the proposed method, can be given by combination of pre-operative MRI scanning, rigid registration and intra-operative rigid-motion tracking with markers attached onto the head skin.

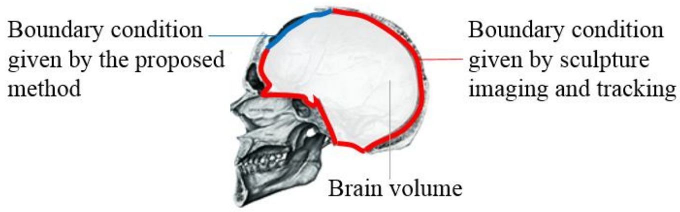

Figure 5-1 application example of our system

6 Conclusions

In this thesis, a marker-less non-rigid method for tracking brain surface by combining shape and texture is proposed.

In brain surgery, the eloquent area which controls patients' speaking, motor and sensor should be avoided and protected in the brain surgery especially when the tumor is near or in these areas. This kind of area is quite important in the surgery. However, the brain shift will happen which make these areas unstable and the brain area should be tracked. Compared to previous on brain surface tracking method, we proposed a new non-rigid registration method to track brain surface by integrating shape and texture information.

Firstly, a brain surface measurement system was implemented by projecting vertical and horizontal patterns on to the brain surface. The 3D measurement system can measure the textured brain surface since the corresponding between the camera image pixel and projector pixel can be obtained simultaneously. Phase-shift 3D shape measurement method can reduce the influence of the texture change because they only consider the phase information projected from the projector.

Secondly, a new non-rigid registration algorithm combines shape and texture information has been proposed to track brain surface during deformation. The texture on the brain surface is extracted by using frangi filter and then the whole textured brain surface is divided into texture points set and surface points set. The texture point obtains the corresponding from the texture point sets and surface point obtains the corresponding from the surface point sets. Then the surface deformed by a smoothness and rigidness constraint to make the shape deform smoothly and as rigidly as possible. After solving a non-linear square least problem, the brain can deform toward the deformed brain surface to achieve tracking.

The 3D measurement experimental result showed that our system had 3D shape measurement of the bias error around 0.31 mm and precision error around 0.025 mm at distance 250 mm and the 3D shape measurement error increases with distance increase. The simulation result showed that the proposed method appeared to be superior to the TPS based registration method regarding on the deformation magnitude, texture frequency and texture direction. Experiments according to brain deformation on vertical and horizontal direction was evaluated using five porcine brains. The vertical experiment can show the capability of the proposed method in tracking brain surface when brain deforms caused by gravity and horizontal experiment shows the capability of the proposed method in tracking when brain deform by pushing. The result showed that proposed method RMSE is around 0.1 mm and smaller than ICP, non-rigid ICP and TPS based registration. For the tracking error evaluated by OPTOTRAK, our proposed method also can achieve an accuracy around 0.9 mm on average and compared to other methods, the proposed method performs better than them. And the error of 0.9 mm on average satisfy the 2 mm accuracy requirement of INGS. All the experiments showed the advantages of the proposed methods and the feasibility in clinical application.

7 Acknowledgment

Foremost, I would like to express my most sincere gratitude to my supervisor Prof. Yoshikazu Nakajima at The University of Tokyo for his continuous support of my Ph. D. study and research, for his passion, diligence, patience, dedication, and immense knowledge. I couldn't have imagined having a better supervisor and mentor for my Ph.D. study. Besides my supervisor, I would like to thank the rest of my thesis committee: Prof. Hideaki Haneishi, Prof. Ichiro Sakuma, Prof. Hiroyuki Takahashi and Prof. Masaki Sekino for their encouragement, insightful comments and career suggestions. In addition, I would like to thank all professors in Bioengineering department. They gave me impressive lectures and insightful suggestions for my research. I thank my group members in Nakajima Lab. former Ph. D. candidate students including Dr. Takaaki Takeshita, Dr. Toki Saito, Dr. Takehito Doke, Dr. Yaming Xu, Dr. Akira Bekku, and Dr. Minkyu Kim were always very patient, modest and passionate about my endless questions. Ph. D. candidate students including Mr. Ben Younes Lassad, Herol Gaibin and Joonhwan Kim always kindly helped me and discussed with me about studies and life in Japan. Also, I would like to thank all the master students in our lab including Mr. Nobuyuki Tanigaki, Masanori Ito, Zijian Cao, Yoshio Sohma, Ryosuke Sudo, Toshiki Manaka who already graduated; all the M2 Mr. Taisuke Isozaki, Kenta Kobayashi, Takahiro Tohchika, and all the M1 Mr. Yuto Shimada, Junnichi Tani, Naoto Masuzawa. Other students in our lab also brought happiness, useful discussion, and helpful suggestion to me. Our beautiful secretaries Mrs. Hiromi Kushibiki and Masayo Seno brought a lot of happiness to us and made our lives easier when they came to administrative support.

I would like to say here thank Yoshio Sohma again. He was always very smart and gave me a lot of suggestions and helped me with my experiments. Without his help, it might be difficult for me to complete my experiments and submit my journal paper on time.

I would like to thank to Sibaura Zouki. They provided porcine brain for our experiments.

I am gratitude to the Chinese Scholar Council. They provided me with financial support for my study in The University of Tokyo. I couldn't imagine that I can complete my study without their nice support. I would like to express my gratitude to Center for Medical System Innovation (CMSI) in the University of Tokyo for financial support. They not only support me in financial but also give me a chance to study in The University of Texas MD Anderson Cancer Center. Last but not the least; I acknowledge my family, my father Zhonggui Jiang, my mother Lingling

Zhao and my sister Yuan Jiang for providing me a loving environment and supporting me in spiritual in all my life. I would like to thank my wife, Wen Wen. We had a very hard time in Tokyo, she always gave me good suggestions and hear my feeling give me motivation.

Reference

1. Olesen, J. and M. Leonardi, *The burden of brain diseases in Europe.* European Journal of Neurology, 2003. **10**(5): p. 471-477.
2. Lag, R., et al., *Seer cancer statistics review.* Bethesda, National Cancer Institute, 1975: p. 1975-2003.
3. https://www.pinterest.com/pin/439945457319027803/. Available from: https://www.pinterest.com/pin/439945457319027803/.
4. Amorim, R.L.O.d., et al., *Cortical stimulation of language fields under local anesthesia: optimizing removal of brain lesions adjacent to speech areas.* Arquivos de neuro-psiquiatria, 2008. **66**(3A): p. 534-538.
5. Hastreiter, P., et al., *Strategies for brain shift evaluation.* Medical image analysis, 2004. **8**(4): p. 447-464.
6. Sun, H., et al., *Stereopsis-guided brain shift compensation.* Medical Imaging, IEEE Transactions on, 2005. **24**(8): p. 1039-1052.
7. Nauta, H.J., *Error assessment during "image guided" and "imaging interactive" stereotactic surgery.* Computerized Medical Imaging and Graphics, 1994. **18**(4): p. 279-287.
8. Hill, D.L., et al., *Measurement of intraoperative brain surface deformation under a craniotomy.* Neurosurgery, 1998. **43**(3): p. 514-526.
9. Bucholz, R.D., et al. *The correction of stereotactic inaccuracy caused by brain shift using an intraoperative ultrasound device.* in *CVRMed-MRCAS'97*. 1997. Springer.
10. Maurer Jr, C.R., et al., *Investigation of intraoperative brain deformation using a 1.5-T interventional MR system: preliminary results.* Medical Imaging, IEEE Transactions on, 1998. **17**(5): p. 817-825.
11. Hartkens, T., et al., *Measurement and analysis of brain deformation during neurosurgery.* Medical Imaging, IEEE Transactions on, 2003. **22**(1): p. 82-92.
12. Dorward, N.L., et al., *Postimaging brain distortion: magnitude, correlates, and impact on neuronavigation.* Journal of neurosurgery, 1998. **88**(4): p. 656-662.
13. Hassenbusch, S.J., J.S. Anderson, and P.K. Pillay, *Brain tumor resection aided with markers placed using stereotaxis guided by magnetic resonance imaging and computed tomography.* Neurosurgery, 1991. **28**(6): p. 801-806.
14. Yoshikawa, K., et al., *Improvement of functional outcome after radical surgery in glioblastoma patients: the efficacy of a navigation-guided fence-post procedure and neurophysiological monitoring.* Journal of neuro-oncology, 2006. **78**(1): p. 91-97.
15. Sakai, K., *Treatment strategy for malignant gliomas.* shinsyo magzine, 2010. **58**(5): p. 11.
16. Lewin, J.S., A. Metzger, and W.R. Selman, *Intraoperative magnetic resonance image guidance in neurosurgery.* Journal of Magnetic Resonance Imaging, 2000. **12**(4): p. 512-524.
17. Kaibara, T., et al., *Optimizing epilepsy surgery with intraoperative MR*

imaging. Epilepsia, 2002. **43**(4): p. 425-429.

18. Sutherland, G.R., et al., *Intraoperative assessment of aneurysm clipping using magnetic resonance angiography and diffusion-weighted imaging: technical case report.* Neurosurgery, 2002. **50**(4): p. 893-898.

19. Kaibara, T., J.K. Saunders, and G.R. Sutherland, *Advances in mobile intraoperative magnetic resonance imaging.* Neurosurgery, 2000. **47**(1): p. 131-138.

20. Sutherland, G.R., et al., *A mobile high-field magnetic resonance system for neurosurgery.* Journal of neurosurgery, 1999. **91**(5): p. 804-813.

21. Nabavi, A., et al., *Serial intraoperative magnetic resonance imaging of brain shift.* Neurosurgery, 2001. **48**(4): p. 787-798.

22. Nimsky, C., et al., *Intraoperative compensation for brain shift.* Surgical neurology, 2001. **56**(6): p. 357-364.

23. Nimsky, C., et al., *Intraoperative magnetic resonance imaging combined with neuronavigation: a new concept.* Neurosurgery, 2001. **48**(5): p. 1082-1091.

24. Buchfelder, M., et al., *Intraoperative magnetic resonance imaging in epilepsy surgery.* Journal of Magnetic Resonance Imaging, 2000. **12**(4): p. 547-555.

25. Fahlbusch, R., O. Ganslandt, and C. Nimsky, *Intraoperative imaging with open magnetic resonance imaging and neuronavigation.* Child's Nervous System, 2000. **16**(10-11): p. 829-831.

26. Nimsky, C., et al., *[Intraoperative magnetic resonance tomography. Experiences with its use in neurosurgery].* Der Nervenarzt, 2000. **71**(12): p. 987-994.

27. Nimsky, C., et al., *Integration of functional magnetic resonance imaging supported by magnetoencephalography in functional neuronavigation.* Neurosurgery, 1999. **44**(6): p. 1249-1255.

28. Steinmeier, R., et al., *Intraoperative magnetic resonance imaging with the magnetom open scanner: concepts, neurosurgical indications, and procedures: a preliminary report.* Neurosurgery, 1998. **43**(4): p. 739-747.

29. Hadani, M., et al., *Novel, compact, intraoperative magnetic resonance imaging-guided system for conventional neurosurgical operating rooms.* Neurosurgery, 2001. **48**(4): p. 799-809.

30. Jolesz, F.A., A. Nabavi, and R. Kikinis, *Integration of interventional MRI with computer‐assisted surgery.* Journal of magnetic resonance imaging, 2001. **13**(1): p. 69-77.

31. Pergolizzi, R.S., et al., *Intra‐operative MR guidance during trans‐sphenoidal pituitary resection: Preliminary results.* Journal of Magnetic Resonance Imaging, 2001. **13**(1): p. 136-141.

32. Nabavi, A., et al., *Image-guided therapy and intraoperative MRI in neurosurgery.* Minimally Invasive Therapy & Allied Technologies, 2000. **9**(3-4): p. 277-286.

33. Black, P.M., et al., *Craniotomy for tumor treatment in an intraoperative magnetic resonance imaging unit.* Neurosurgery, 1999. **45**(3): p. 423.

34. Knauth, M., et al., *Low-field interventional MRI in neurosurgery: finding the right dose of contrast medium.* Neuroradiology, 2001. **43**(3): p. 254-258.

35. Wirtz, C.R., et al., *Clinical evaluation and follow-up results for intraoperative magnetic resonance imaging in neurosurgery.* Neurosurgery, 2000. **46**(5): p. 1112-1122.

36. Tronnier, V., et al., *MRI-guided brain biopsies using a 0.2 Tesla open magnet.* Minimally invasive neurosurgery: MIN, 1999. **42**(3): p. 118-122.

37. Knauth, M., et al., *[Intraoperative magnetic resonance tomography for*

control of extent of neurosurgical operations]. Der Radiologe, 1998. **38**(3): p. 218-224.

38. Wirtz, C.R., et al., *Modified Headholder and operating table for intra-operative MRI in neurosurgery.* Neurological research, 1998. **20**(7): p. 658-661.

39. Wirtz, C.R., et al., *Image-guided neurosurgery with intraoperative MRI: update of frameless stereotaxy and radicality control.* Stereotactic and functional neurosurgery, 1997. **68**(1-4): p. 39-43.

40. Tronnier, V.M., et al., *Intraoperative diagnostic and interventional magnetic resonance imaging in neurosurgery.* Neurosurgery, 1997. **40**(5): p. 891-902.

41. Pamir, M., et al., *Intraoperative MR imaging: preliminary results with 3 tesla MR system*, in *Medical Technologies in Neurosurgery*. 2006, Springer. p. 97-100.

42. Engle, D.J., D.L. Lunsford, and T. Panichelli, *Rigid head fixation for intraoperative computed tomography.* Neurosurgery, 1986. **19**(2): p. 258-262.

43. Lunsford, L.D., A.J. Martinez, and R.E. Latchaw, *Stereotaxic surgery with a magnetic resonance-and computerized tomography-compatible system.* Journal of neurosurgery, 1986. **64**(6): p. 872-878.

44. Lunsford, D.L., R. Parrish, and L. Albright, *Intraoperative imaging with a therapeutic computed tomographic scanner.* Neurosurgery, 1984. **15**(4): p. 559-561.

45. Lunsford, L.D. and A.J. Martinez, *Stereotactic exploration of the brain in the era of computed tomography.* Surgical neurology, 1984. **22**(3): p. 222-230.

46. Lunsford, L., L. Leksell, and B. Jernberg, *Probe holder for stereotactic surgery in the CT scanner a technical note.* Acta neurochirurgica, 1983. **69**(3-4): p. 297-304.

47. Lunsford, L., *A dedicated CT system for the stereotactic operating room.* Stereotactic and Functional Neurosurgery, 1982. **45**(4-5): p. 374-378.

48. Lunsford, L., D. Kondziolka, and D. Bissonette, *Intraoperative imaging of the brain.* Stereotactic and functional neurosurgery, 1996. **66**(1-3): p. 58-64.

49. http://neurosurgery.mgh.harvard.edu/NeuroScience/mobileCT.htm.; Available from: http://neurosurgery.mgh.harvard.edu/NeuroScience/mobileCT.htm.

50. Roberts, D.W., et al., *A frameless stereotaxic integration of computerized tomographic imaging and the operating microscope.* Journal of neurosurgery, 1986. **65**(4): p. 545-549.

51. Rubin, J.M. and G. Dohrmann, *Intraoperative neurosurgical ultrasound in the localization and characterization of intracranial masses.* Radiology, 1983. **148**(2): p. 519-524.

52. Tsutsumi, Y., Y. Andoh, and N. Inoue, *Ultrasound-guided biopsy for deep-seated brain tumors.* Journal of neurosurgery, 1982. **57**(2): p. 164-167.

53. Sjölander, U., P.G. Lindgren, and R. Hugosson, *Ultrasound sector scanning for the localization and biopsy of intracerebral lesions.* Journal of neurosurgery, 1983. **58**(1): p. 7-10.

54. Rubin, J. and G. Dohrmann, *Efficacy of intraoperative US for evaluating intracranial masses.* Radiology, 1985. **157**(2): p. 509-511.

55. Quencer, R. and B. Montalvo, *Intraoperative cranial sonography.* Neuroradiology, 1986. **28**(5-6): p. 528-550.

56. Machi, J., et al., *Criteria for using imaging ultrasound during brain and spinal cord surgery.* Journal of Ultrasound in Medicine, 1984. **3**(4): p. 155-161.

57. Lange, S.C., et al., *Intraoperative ultrasound detection of metastatic tumors in the central cortex.* Neurosurgery, 1982. **11**(2): p. 219-222.

58. Koivukangas, J. and P. Kelly, *Application of ultrasound imaging to stereotactic brain tumor surgery.* Annals of clinical research, 1985. **18**: p. 25-32.

59. Knake, J., et al., *Intraoperative sonographic delineation of low-grade brain neoplasms defined poorly by computed tomography.* Radiology, 1984. **151**(3): p. 735-739.

60. Knake, J., et al., *Neurosurgical applications of intraoperative ultrasound.* Radiologic Clinics of North America, 1985. **23**(1): p. 73-90.

61. Gooding, G., et al., *Intraoperative real-time ultrasound in the localization of intracranial neoplasms.* Radiology, 1983. **146**(2): p. 459-462.

62. Gooding, G., J. Boggan, and P. Weinstein, *Characterization of intracranial neoplasms by CT and intraoperative sonography.* American journal of neuroradiology, 1984. **5**(5): p. 517-520.

63. Gooding, G., et al., *Neurosurgical sonography: intraoperative and postoperative imaging of the brain.* American journal of neuroradiology, 1984. **5**(5): p. 521-525.

64. Chandler, W.F., et al., *Intraoperative use of real-time ultrasonography in neurosurgery.* Journal of neurosurgery, 1982. **57**(2): p. 157-163.

65. Berger, M.S., *Ultrasound-guided stereotaxic biopsy using a new apparatus.* Journal of neurosurgery, 1986. **65**(4): p. 550-554.

66. LeRoux, P.D., et al., *Correlation of intraoperative ultrasound tumor volumes and margins with preoperative computerized tomography scans: An intraoperative method to enhance tumor resection.* Journal of neurosurgery, 1989. **71**(5): p. 691-698.

67. Comeau, R.M., et al., *Intraoperative ultrasound for guidance and tissue shift correction in image-guided neurosurgery.* Medical Physics, 2000. **27**(4): p. 787-800.

68. Gobbi, D.G., R.M. Comeau, and T.M. Peters. *Ultrasound/MRI overlay with image warping for neurosurgery*. in *Medical Image Computing and Computer-Assisted Intervention–MICCAI 2000*. 2000. Springer.

69. Comeau, R.M., A. Fenster, and T.M. Peters, *Intraoperative US in interactive image-guided neurosurgery.* Radiographics, 1998. **18**(4): p. 1019-1027.

70. Edwards, P.J., et al., *A three-component deformation model for image-guided surgery.* Medical image analysis, 1998. **2**(4): p. 355-367.

71. Ferrant, M., et al., *Registration of 3-D intraoperative MR images of the brain using a finite-element biomechanical model.* Medical Imaging, IEEE Transactions on, 2001. **20**(12): p. 1384-1397.

72. Škrinjar, O., A. Nabavi, and J. Duncan, *Model-driven brain shift compensation.* Medical image analysis, 2002. **6**(4): p. 361-373.

73. Škrinjar, O., A. Nabavi, and J. Duncan. *A stereo-guided biomechanical model for volumetric deformation analysis*. in *Mathematical Methods in Biomedical Image Analysis, 2001. MMBIA 2001. IEEE Workshop on*. 2001. IEEE.

74. Škrinjar, O., et al. *Steps toward a stereo-camera-guided biomechanical model for brain shift compensation*. in *Information Processing in Medical Imaging*. 2001. Springer.

75. Škrinjar, O., D. Spencer, and J. Duncan, *Brain shift modeling for use in neurosurgery*, in *Medical Image Computing and Computer-Assisted Interventation—MICCAI'98*. 1998, Springer. p. 641-649.

76. Platenik, L.A., et al., *In vivo quantification of retraction deformation modeling for updated image-guidance during neurosurgery.* Biomedical Engineering,

IEEE Transactions on, 2002. **49**(8): p. 823-835.

77. Miga, M.I., et al., *Modeling of retraction and resection for intraoperative updating of images.* Neurosurgery, 2001. **49**(1): p. 75-85.

78. Miga, M.I., et al., *In vivo quantification of a homogeneous brain deformation model for updating preoperative images during surgery.* Biomedical Engineering, IEEE Transactions on, 2000. **47**(2): p. 266-273.

79. Miga, M.I., et al., *In vivo modeling of interstitial pressure in the brain under surgical load using finite elements.* Journal of biomechanical engineering, 2000. **122**(4): p. 354-363.

80. MIGA, M.I., et al., *In vivo analysis of heterogeneous brain deformation computations for model-updated image guidance.* Computer Methods in Biomechanics and Biomedical Engineering, 2000. **3**(2): p. 129-146.

81. Miga, M.I., et al. *Model-updated image-guided neurosurgery using the finite element method: Incorporation of the falx cerebri*. in *Medical Image Computing and Computer-Assisted Intervention–MICCAI'99*. 1999. Springer.

82. Miga, M.I., et al. *Model-updated image guidance: initial clinical experiences with gravity-induced brain deformation*. in *Biomedical Imaging, 2002. 5th IEEE EMBS International Summer School on*. 2002. IEEE.

83. Miga, M.I., et al., *Updated neuroimaging using intraoperative brain modeling and sparse data.* Stereotactic and functional neurosurgery, 1999. **72**(2-4): p. 103-106.

84. Paulsen, K.D., et al., *A computational model for tracking subsurface tissue deformation during stereotactic neurosurgery.* Biomedical Engineering, IEEE Transactions on, 1999. **46**(2): p. 213-225.

85. Miga, M., et al., *Initial in-vivo analysis of 3d heterogeneous brain computations for model-updated image-guided neurosurgery*, in *Medical Image Computing and Computer-Assisted Interventation—MICCAI'98*. 1998, Springer. p. 743-752.

86. Miller, K., *Constitutive model of brain tissue suitable for finite element analysis of surgical procedures.* Journal of biomechanics, 1999. **32**(5): p. 531-537.

87. Miller, K. and K. Chinzei, *Constitutive modelling of brain tissue: experiment and theory.* Journal of biomechanics, 1997. **30**(11): p. 1115-1121.

88. Fontenla, E., et al., *Using serial imaging data to model variabilities in organ position and shape during radiotherapy.* Physics in medicine and biology, 2001. **46**(9): p. 2317.

89. Hata, N., et al., *Three-dimensional optical flow method for measurement of volumetric brain deformation from intraoperative MR images.* Journal of Computer Assisted Tomography, 2000. **24**(4): p. 531-538.

90. Ji, S., et al. *An integrated model-based neurosurgical guidance system*. in *SPIE Medical Imaging*. 2010. International Society for Optics and Photonics.

91. Sun, H., et al., *Modeling of brain tissue retraction using intraoperative data*, in *Medical Image Computing and Computer-Assisted Intervention–MICCAI 2004*. 2004, Springer. p. 225-233.

92. Ji, S., et al., *Cortical surface strain estimation using stereovision*, in *Medical Image Computing and Computer-Assisted Intervention–MICCAI 2011*. 2011, Springer. p. 412-419.

93. Ji, S., et al., *Cortical surface shift estimation using stereovision and optical flow motion tracking via projection image registration.* Medical image analysis, 2014. **18**(7): p. 1169-1183.

94. Sun, H., et al., *Cortical surface tracking using a stereoscopic operating microscope.* Neurosurgery, 2005. **56**(1): p. 86-97.
95. Miga, M.I., T.K. Sinha, and D.M. Cash, *Techniques to correct for soft tissue deformations during image-guided brain surgery.* Biomechanics Applied to Computer Assisted Surgery, 2005: p. 153-177.
96. Cao, A., et al., *Laser range scanning for image-guided neurosurgery: Investigation of image-to-physical space registrations.* Medical physics, 2008. **35**(4): p. 1593-1605.
97. Cash, D.M., et al., *Incorporation of a laser range scanner into image-guided liver surgery: Surface acquisition, registration, and tracking.* Medical Physics, 2003. **30**(7): p. 1671-1682.
98. Chen, I., et al., *Intraoperative brain shift compensation: accounting for dural septa.* Biomedical Engineering, IEEE Transactions on, 2011. **58**(3): p. 499-508.
99. Zhang, C., M. Wang, and Z. Song, *A brain-deformation framework based on a linear elastic model and evaluation using clinical data.* Biomedical Engineering, IEEE Transactions on, 2011. **58**(1): p. 191-199.
100. Ding, S., et al., *Tracking of vessels in intra-operative microscope video sequences for cortical displacement estimation.* Biomedical Engineering, IEEE Transactions on, 2011. **58**(7): p. 1985-1993.
101. Ding, S., et al., *Semiautomatic registration of pre-and postbrain tumor resection laser range data: method and validation.* Biomedical Engineering, IEEE Transactions on, 2009. **56**(3): p. 770-780.
102. Ding, S., et al. *Estimation of intra-operative brain shift using a tracked laser range scanner*. in *Engineering in Medicine and Biology Society, 2007. EMBS 2007. 29th Annual International Conference of the IEEE*. 2007. IEEE.
103. Garg, I., et al. *Enhancement of subsurface brain shift model accuracy: a preliminary study*. in *SPIE Medical Imaging*. 2010. International Society for Optics and Photonics.
104. Cao, A., P. Dumpuri, and M.I. Miga. *Tracking cortical surface deformations based on vessel structure using a laser range scanner*. in *Biomedical Imaging: Nano to Macro, 2006. 3rd IEEE International Symposium on*. 2006. IEEE.
105. Sinha, T.K., et al., *Intraoperative cortical surface characterization using laser range scanning: Preliminary results.* Neurosurgery, 2006. **59**(4 0 2).
106. Dumpuri, P., et al., *An atlas-based method to compensate for brain shift: Preliminary results.* Medical Image Analysis, 2007. **11**(2): p. 128-145.
107. Sinha, T.K., et al., *A method to track cortical surface deformations using a laser range scanner.* Medical Imaging, IEEE Transactions on, 2005. **24**(6): p. 767-781.
108. Miga, M.I., et al., *Cortical surface registration for image-guided neurosurgery using laser-range scanning.* Medical Imaging, IEEE Transactions on, 2003. **22**(8): p. 973-985.
109. Sinha, T.K., et al., *Cortical shift tracking using a laser range scanner and deformable registration methods*, in *Medical Image Computing and Computer-Assisted Intervention-MICCAI 2003*. 2003, Springer. p. 166-174.
110. Sinha, T.K., et al., *Cortical surface registration using texture mapped point clouds and mutual information*, in *Medical Image Computing and Computer-Assisted Intervention—MICCAI 2002*. 2002, Springer. p. 533-540.
111. Frangi, A.F., et al., *Multiscale vessel enhancement filtering*, in *Medical Image Computing and Computer-Assisted Interventation—MICCAI'98*. 1998,

Springer. p. 130-137.
112. https://en.wikipedia.org/wiki/Levenberg%E2%80%93Marquardt_algorithm. Available from: https://en.wikipedia.org/wiki/Levenberg%E2%80%93Marquardt_algorithm.
113. Faria, C., et al., *Validation of a stereo camera system to quantify brain deformation due to breathing and pulsatility.* Medical physics, 2014. **41**(11): p. 113502.
114. Reinertsen, I., et al., *Clinical validation of vessel-based registration for correction of brain-shift.* Medical Image Analysis, 2007. **11**(6): p. 673-684.
115. Reinertsen, I., et al., *Validation of vessel-based registration for correction of brain shift.* Medical image analysis, 2007. **11**(4): p. 374-388.
116. Marreiros, F.M., et al., *Non-rigid deformation pipeline for compensation of superficial brain shift*, in *Medical Image Computing and Computer-Assisted Intervention–MICCAI 2013*. 2013, Springer. p. 141-148.
117. Paul, P., X. Morandi, and P. Jannin, *A surface registration method for quantification of intraoperative brain deformations in image-guided neurosurgery.* Information Technology in Biomedicine, IEEE Transactions on, 2009. **13**(6): p. 976-983.
118. Olesen, O.V., et al., *Motion tracking for medical imaging: a nonvisible structured light tracking approach.* Medical Imaging, IEEE Transactions on, 2012. **31**(1): p. 79-87.
119. Wen, R., et al., *Projection-based visual guidance for robot-aided RF needle insertion.* International journal of computer assisted radiology and surgery, 2013. **8**(6): p. 1015-1025.
120. Yachide, Y., et al. *Real-time 3-D measurement system based on light-section method using smart image sensor*. in *Image Processing, 2005. ICIP 2005. IEEE International Conference on*. 2005. IEEE.
121. Karpinsky, N. and S. Zhang, *High-resolution, real-time 3D imaging with fringe analysis.* Journal of Real-Time Image Processing, 2012. **7**(1): p. 55-66.
122. Asundi, A. and Z. Wensen, *Fast phase-unwrapping algorithm based on a gray-scale mask and flood fill.* Applied optics, 1998. **37**(23): p. 5416-5420.
123. Fang, S., et al., *Quality-guided phase unwrapping algorithm based on reliability evaluation.* Applied optics, 2011. **50**(28): p. 5446-5452.
124. Ghiglia, D.C. and M.D. Pritt, *Two-dimensional phase unwrapping: theory, algorithms, and software*. Vol. 4. 1998: Wiley New York.
125. Herráez, M.A., et al., *Fast two-dimensional phase-unwrapping algorithm based on sorting by reliability following a noncontinuous path.* Applied Optics, 2002. **41**(35): p. 7437-7444.
126. Zhang, S. and P.S. Huang, *Novel method for structured light system calibration.* Optical Engineering, 2006. **45**(8): p. 083601-083601-8.
127. http://elonen.iki.fi/code/tpsdemo/. Available from: http://elonen.iki.fi/code/tpsdemo/.
128. : p. http://www.konicaminolta.com/instruments/download/instruction_manual/3d/pdf/range7-5_instruction_eng.pdf.